https://doi.org/10.1016/j.jallcom.2020.154597

Hydrogen Storage in Light-Metal Based Systems: A Review

Liuzhang Ouyang[a, b, *], Kang Chen[a], Jun Jiang[a], Xu-Sheng Yang[c, d, *], Min Zhu[a, b]

[a]School of Materials Science and Engineering, Guangdong Provincial Key Laboratory of Advanced Energy Storage Materials, South China University of Technology, Guangzhou, 510641, People's Republic of China. E-mail: meouyang@scut.edu.cn

[b]China-Australia Joint Laboratory for Energy & Environmental Materials, Key Laboratory of Fuel Cell Technology of Guangdong Province, Guangzhou, 510641, People's Republic of China

[c]Advanced Manufacturing Technology Research Centre, Department of Industrial and Systems Engineering, The Hong Kong Polytechnic University, Hung Hom, Kowloon, Hong Kong, China. Email: xsyang@polyu.edu.hk

[d]Hong Kong Polytechnic University Shenzhen Research Institute, Shenzhen 518057, China

ABSTRACT

Promoting widespread utilization of sustainable and renewable energy sources along with efficient energy storage and conversion technologies is vital to address gargantuan energy and environmental challenges. Hydrogen, working as an eco-friendly and highest mass-energy density clean energy carrier for abundant but fluctuating renewable power, has been recognized as an ideal alternative for fossil fuels in both mobile and stationary applications. To date, the production, storage, and delivery of hydrogen remain a linchpin enabling technologies for the advent of the hydrogen economy community. Herein, an overview is present of recent research progress on hydrogen release and uptake in potential reversible systems with a focus on light-metal hydrogen storage

materials, including magnesium (Mg)-based hydrides, metal alanates, borohydrides, and amides. Both Mg-based hydrides and complex hydrides are, however, plagued by unfavorable thermodynamics and/or sluggish kinetics in the dehydrogenation and/or rehydrogenation. To overcome these challenges, recent advances have been driven by tremendous efforts, such as catalysis, nanoscaling, compositing or ionic substitutions, etc. Though great achievements have been attained in light-metal based materials, it is still far from satisfying the requirements of practical automotive applications. Sustainable research efforts are further needed to be made for solving the intrinsic thermodynamic and kinetic barriers.

Keywords: Light-weight hydrogen storage; Mg-based hydrides; Complex hydrides; Thermodynamics; Kinetics

1. Introduction

1.1. Hydrogen energy economy and hydrogen storage

The continuously rising concerns for the energy crisis (dwindling traditional energy resources, such as petroleum, coal, and natural gas, etc.) and the environmental issues of burning fossil fuels have prompted tremendous efforts on exploration of sustainable and renewable alternative energy carriers, including nuclear energy [1], solar energy [2, 3], and hydrogen energy [4, 5], etc. Among the above substitutes, hydrogen has been in the limelight for the past decades from the viewpoint of the so-called "hydrogen energy economy" [6-8], owing to its abundant content, environmentally benign products of oxidation (water), high energy density (142 MJ/kg) and so on. Initially proposed by genetics J. B. S Haldane in conceptually, the term "hydrogen economy" was lately coined by John Bockris during a talk that he gave in 1970 at General Motor Technical Center [9] [10]. The hydrogen economy is, in fact, the utilization of hydrogen as a fuel, particularly for heating and hydrogen vehicles [11] as well as using hydrogen for long-term energy storage and for long-distance transport of low-carbon energy.

However, a major barrier for the transition of the world from the current hydrocarbon economy to the future hydrogen economy lies in the lack of efficient hydrogen storage methods in harnessing the enormous amount of hydrogen for use in stationary, portable and automotive applications. As we all know, hydrogen storage strategies are usually assigned into ultrahigh-pressure hydrogen storage (H-storage, hereinafter), cryogenic-liquid and solid-state H-storage. H-density is very low no matter as compressed gas or as condensed liquid, i.e. 0.024 kg H_2/L at pressure as high as 700 bar and 0.071 kg H_2/L as a liquid at the temperature as low as -253 ℃ [12, 13]. Although the technologies for compressing gaseous hydrogen and condensing liquid hydrogen are relatively

mature and have been applied in various prototype vehicles [14, 15], the hydrogen storage densities still fall short of the targets for the US Department of Energy (DOE). For instance, the H-storage targets of DOE upon onboard hydrogen applications in terms of gravimetric and volumetric density are 1.6 and 2.1 times higher (**Table 1**), respectively, than the highest values achieved to date using state-of-the-art 700-bar tanks [16]. Besides, the use of ultra-high pressurized compressed tanks not only requires super-high compressive strength assembly materials, but also incurs safety risks and considerable ineluctable energy consumption during compression. For liquefaction hydrogen, in spite of a much higher volumetric density (0.071 kg H_2/L) in comparison with that of hydrogen gas, the inevitable hydrogen loss resulted from heat transfer and a large amount of energy for liquefying hydrogen severely impede its practical applications [17, 18]. Compared to ultrahigh-pressure or cryogenic-liquid H-storage, solid H-storage has received much attention owing to its higher energy density and safety. Therefore, mainstream researches have been focused on developing suitable solid hydrogen storage systems for off- or on-board hydrogen applications. **Fig. 1** presents the volumetric versus gravimetric H-density of the diverse hydrogen-contained materials [19].

Table 1. Current states vs targets for onboard H_2 storage for light-duty fuel cell vehicles [16].

Storage targets	Gravimetric kWh/kg (kg H_2/kg system)	Volumetric kWh/L (kg H_2/L system)	Cost[1] \$/kWh (\$/kg H_2)
2020	1.5 (0.045)	1.0 (0.030)	\$10 (\$333)
2025	1.8 (0.055)	1.3 (0.040)	\$9 (\$300)
Ultimate	2.2 (0.065)	1.7 (0.050)	\$8 (\$266)
Current status[2]			
700 bar compressed (5.6 kg H_2, type IV, single tank)	1.4 (0.042)	0.8 (0.024)	\$15 (\$500)

[1] Projected at 500,000 units/year

[2] FCTO Data Record #15013, 11/25/2015: https://www.hydrogen.energy.gov/pdfs/15013_onboard_storage performance cost.pdf

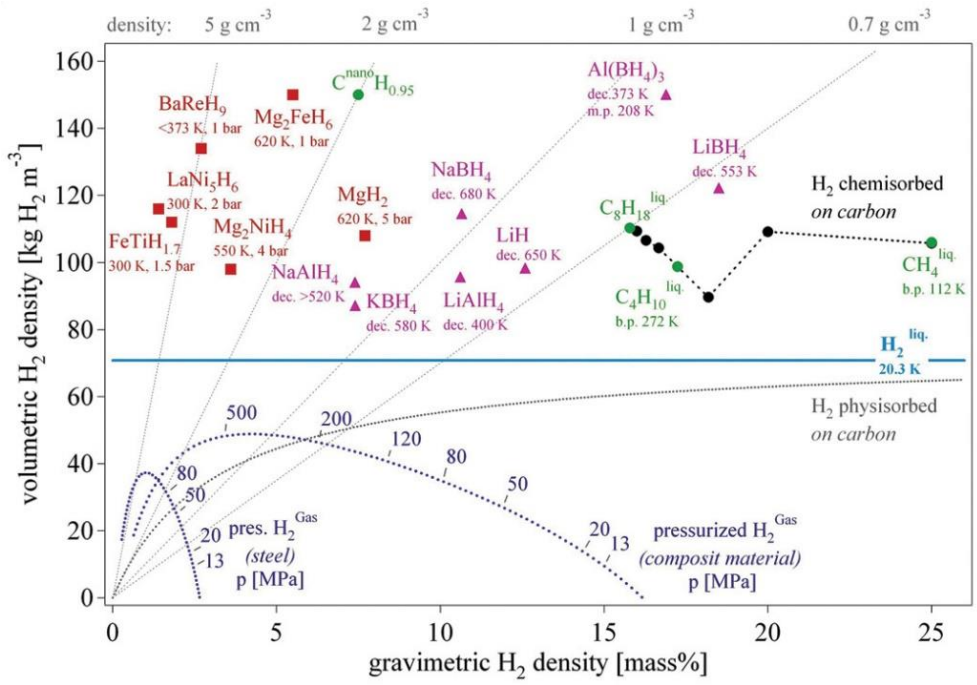

Fig. 1. Volumetric and gravimetric hydrogen density of some hydrides. Reprinted with permission from ref [19]. Copyright 2003 Elsevier.

1.2. Advantages and remaining challenges in light-metal based materials

Generally, solid hydrogen storage materials can be fell into nanostructured materials for hydrogen physisorption (van der Waals interactions) and chemisorption materials (chemical action). The above nanostructured materials are mainly carbon-based materials and recently emerging Metal-Organic Frameworks (MOFs) with low density, ultrahigh surface area and porosity [20-22]. MOFs are comprised of metallic ions or clusters combined by multidentate organic functional groups, delivering extremely large specific surface areas over 5000 m^2/g and tuneable properties [17, 23]. However, the hydrogen uptake upon the porous materials only occurs at cryogenic temperatures, because of the weak interaction between H_2 and sorbents. The hydrogen storage capacity of these materials is extremely low, usually < 2 mass % at ambient conditions [24, 25]. Further researches indicated that the hydrogen capacity is approximately proportional to the surface area and micropore volume [19, 26, 27].

As opposed to physisorption materials, chemisorption materials (metal hydrides, complex and chemical hydrides, etc.) combine with atomic or ionic H in the form of metallic bonding, covalent bonding or ionic bonding, thus achieving solid hydrogen storage. Conventional metal hydrides (e.g. $LaNi_5H_6$, $TiFeH_2$, $ZrMn_2$) were in the limelight for the past decades in the hydrogen storage community, because of their reversibility and rapid kinetics under suitable temperature and pressure [28]. Unfortunately, the applications of these hydrides have been hindered by the limited gravimetric density (< 2 wt% H_2), which is far from the hydrogen storage targets given by DOE, particularly for vehicular hydrogen energy areas. Thus, research turns into novel light-metal, such as Li, B, N, Na, Mg, and Al in hydride forms, for using as solid-state storage materials [29]. These light metal-based hydrides (e.g., magnesium (Mg)-based materials or complex hydrides) exhibits great potential in off-/on-board applications, for their charming volumetric and gravimetric hydrogen densities [30, 31]. The hydrogen capacity of representative Mg-based hydrides or complex hydrides surpasses the target for vehicle applications given by DOE, being 7.6 wt% for MgH_2 and 18.5 wt% for $LiBH_4$, respectively. However, most of the hydrides are plagued by their unfavorable kinetic barriers, stable thermodynamics or/and poor reversibility. **Table 2** lists a comparison between typical light-/heavy-weight solid hydrogen storage materials.

In this review, we summarize the recent advances upon the thermodynamics and kinetics of light-metal based materials, especially for Mg-based hydrides and complex hydrides with effective tuning strategies, such as catalysis, nanoscaling, and compositing, etc.

Table 2. A comparison between typical lightweight and heavyweight solid-state hydrogen storage materials [32].

Parameters	Lightweight				Heavyweight	
Category	Metal hydride	Complex hydride	Microporous adsorbents		AB_5	AB
Compound	MgH_2	$LiBH_4$	Activated Carbon	MOF	$LaNi_5$	TiFe
Gravimetric capacity (wt%)	7.6	18.5	2.1-2.6	6.1	1.4	1.89
Volumetric capacity (g/L)	110	121	20	20	125	114
Cost	Low	High	Low	Low	High	Low
Kinetics rate	Slow	Slow	Fast	Fast	Moderate	Moderate
Operating temperature (°C)	Very high (> 300)	Very high (380-600)	Low (-196~25)	Cryogenic (-196)	Ambient temperature	Ambient temperature
Abundant	High availability	Produce from $NaBH_4$	High availability	High availability	High availability	High availability

2. Mg-based hydrides

2.1. Overview

Mg-based materials have been researched extensively due to virtually limitless amount of Mg, being ~0.13 wt% in seawater and the 8th most abundant element in the earth crust (~2.3%) of this cheap and readily available light-weight metal with the density of ~1.74 g/cm^3 [33]. Generally, Mg-based alloys possess considerable hydrogen capacity as a result of the high theoretical H-capacity of the host material (MgH_2, has ideal hydrogen densities, up to 7.6 wt% H_2 and 110 g H_2/L, respectively.). With respect to economics, the industrial production technologies of Mg-based alloys are mature, rendering it possible for large-scale practical applications. Mg_2Ni, firstly investigated by Reilly and Wiswall in 1968, could reversibly react with H_2 to form a new hydride Mg_2NiH_4, delivering a H-capacity of 3.6 wt% [34]. On the other hand, the electrochemical capacity of Mg_2NiH_4 is up to 999 mAh/g, almost three times as high as commercial $LaNi_5$-type alloy [35]. Overall, Mg-based alloys show gargantuan potential as energy-storage materials.

However, these Mg-based materials suffer from troublesome thermodynamics and kinetics during hydrogen release and uptake. For example, the formation enthalpy (ΔH) and entropy (ΔS) of MgH_2 are -74 kJ/mol and -130 J/(K·mol) H_2, respectively. Corresponding to its thermodynamic nature, the equilibrium dehydrogenation temperature is > 289 °C under ambient pressure [36, 37]. Usually, ΔH and ΔS can be calculated according to Vant's Hoff equation in pressure-composition isotherm (PCI) curves for hydrogen ad-/desorption, while activation energy (Ea, a parameter that reflects kinetic barrier) can be given by Arrhenius or Kissinger's equation [38]. Numerous approaches have been developed to tailor the thermodynamics and kinetics for hydrogen release and uptake in Mg-based hydrides, such as alloying, catalyzing, nanostructuring, forming composites, and destabilizing, etc. **Table 3** lists the thermodynamic, kinetic and hydrogen storage properties of some Mg-based hydrides.

Table 3. Summary of thermodynamics, kinetics and hydrogen storage properties of some Mg-based materials.

Materials	Formation enthalpy, ΔH (kJ/mol H_2)	Activation energy, Ea (kJ/mol)	Gravimetric capacity (wt%)	Desorption temperature: (°C) [H_2 pressure]	Ref.
Mg (bulk)	74.5	-	7.6	300 [1 bar]	[39]
Mg-nanocrystals (d_{avg} < 6nm) in PMMA	-	25	4	200 [35 bar]	[40]
Mg_2Ni	64.5	-	3.6	254 [1 bar]	[34]
MgH_2/multi-valence Ti composites	75.1	30.8	6.7	279 [1 bar]	[41]
Ni-modified MgH_2/GR hybrids	62.1	22.7	5.4	150 [0.01 bar]	[42]
$CeH_{2.73}$-MgH_2-Ni	76	63	4.0	232 [0.1 bar]	[43]
Mg_2Si	36.4	-	5.0	-	[44]
$Mg_{0.95}(In)_{0.05}$	68.1	-	5.3	-	[45]
$Mg_2(In)_{0.1}Ni$	38.4	28.9	3.0	-	[46]

2.2. Kinetic tuning of Mg-based hydrides

2.2.1. Nanostructuring

Nanoscaling has exhibited an undoubtedly effect upon enhancing the hydrogen release and uptake kinetics of Mg-based alloys. The kinetics depends heavily on the particle size of Mg-based materials. Numerous studies [40, 47] have proposed that reducing the particle size into nanometer could greatly increase the ratio of surface area to volume, thereby simultaneously providing more nucleation sites, promoting rapid diffusion of hydrogen alongside the interface of Mg/MgH_2 or internal boundaries and defects of hydrides, and delivering shortened hydrogen diffusion path. Zaluska et al. [48] reported the de-/hydrogenation kinetic behaviors of nanocrystalline Mg, and they found that Mg is unable to absorb hydrogen at the crystallite size over 1 um at 300 °C, whereas both of hydrogen absorption rate and capacity are apparently enhanced as the crystallite size downshifted to 50 nm under the same conditions. Qu and co-workers [49] calculated the hydrogen diffusion coefficient for nanocrystalline Mg film, being 6.52×10^{-19} m^2/s at 25 °C, much higher than the value of 1.1×10^{-20} m^2/s for the coarse-grained Mg.

Mg-based nanomaterials can be acquired by several technologies, such as ball milling (BM) and a few techniques adopting severe plastic deformation (e.g., hydrogen plasma-metal reaction, equal channel angular pressing, and high-pressure torsion, etc.). Unfortunately, the nanometer-size Mg particles tend to aggregate together and coarsen during hydrogen release/uptake cycling. For instance, the particle size of nanocrystalline Mg might increase from 30~50 nm before hydrogen absorption to 100~500 nm after hydrogen uptake [50]. Hence, stabilizing metastable nanostructure is of critical importance in the development of a series of nanoscaling technologies for Mg-based alloys. Gross et al. [51] fabricated MgH_2 nanoparticles in carbon aerogel with pore sizes from 2 to

~30 nm and found that the desorption rate of catalyst-free nanoconfined MgH_2 reaches 2.2 wt%/h at 250 °C, much higher than that (0.12 wt%/h) of MgH_2 milled with synthetic graphite under the same conditions. In the same year, Nielsen et al. [52] successfully synthesized MgH_2 nanoparticles dispersed uniformly in nanoporous carbon gel scaffold materials via wet chemical impregnation, namely loading precursor $MgBu_2$ heptane solution into carbon aerogel with average pore diameters between 7-22 nm and then $MgBu_2$ converted directly into MgH_2 under 137 °C and 5 MPa of hydrogen pressure. The results indicated that the nanometer-sized MgH_2 presents 4 times hydrogen desorption rate as fast as that of the ball-milled MgH_2, and the onset desorption temperature is as low as ~200 °C. Recently, Au et al. [53] reported that the growth of MgH_2 nanoparticles, supported on high surface area carbon aerogels with pore sizes of 6-20 nm, are effectively restrained by the carbon support. It was found that the MgH_2 nanoparticles enable hydrogen absorption of ~1.75 wt% H_2 within 1 h, whereas bulk MgH_2 only absorb 0.25 wt% H_2 after 60 min. However, there are many drawbacks in the aforementioned nanoconfined methods, including difficulty in large-scale production and low hydrogen storage capacity of loading systems compared to pure MgH_2 with limited embedding amount of hydrides supported on scaffold materials.

2.2.2. Doping Catalysts

Another method, i.e., doping catalytic additives, has been demonstrated as a promising strategy to improve the reaction kinetics of Mg-H in Mg-based systems. This is mainly because addition of catalysts can effectively reduce the reaction energy barrier, thus accelerating the hydrogen absorption/desorption rate of Mg-H systems. These catalysts are often classified into three categories: metals, metal oxides and metal halides, and carbon-based nanostructure, which will be discussed more specifically in the following sections.

(1) Metals

Zaluska and co-workers [48] reported that the rehydrogenation/dehydrogenation kinetics of Mg-based materials were enhanced by catalyzing through 1.0 wt% of Pt nanoparticles located on Mg surface. Liang et al. [54] proposed that the 3d-transition metals (TM = Ti, V, Ni, Fe, Mn) present diverse catalytic effects upon hydrogen release/uptake kinetics of Mg-based systems, of which Mg-Ti exhibited optimal hydrogen absorption kinetics, followed by Mg-V, Mg-Fe, Mg-Mn, and Mg-Ni. On the other hand, the MgH_2-V system possessed most rapid H-desorption rate, followed in order by MgH_2-Ti, MgH_2-Fe, MgH_2-Ni, and MgH_2-Mn. Berlouis et al. [55] also confirmed that the active role played by Ni for rapid uptake of hydrogen because Ni improves dissociation of H_2 and enables faster formation of Mg hydride. Besides, Yin et al. [56] found that Mg_2Ni showed superior hydrogen absorption kinetics with the addition of rare-earth element Nd at the temperature above 100 ℃ as well as superb desorption over 200 ℃. To figure out the enhanced dynamics, Huot and Pelletier et al. [57-59] adopted in-situ time-resolved X-ray scattering measurements on hydrogen desorption in MgH_2-Nb nanocomposites using synchrotron radiation. They revealed that the real catalyst was a short-lived metastable $NbH_{0.6}$ phase with ordered vacancies, which provided the diffusion channels for hydrogen transfer. This was the first time that the dehydrogenation mechanism of MgH_2-TM systems was verified directly, of which hydrogen was prior to being released through the catalytic phase, namely “hydrogen pump”.

Recently, Liu et al. [60, 61] reported superior catalytic effects derived from Ti-based alloys on the dehydrogenation/hydrogenation kinetics of MgH_2. They firstly adopted 2D Ti_3C_2 as a novel catalyst precursor for the reversible hydrogen behaviors of MgH_2, which was synthesized by the exfoliation of the MAX phase of Ti_3AlC_2 with HF solution [60]. As a result, the onset

dehydrogenation temperature of the 5 wt% Ti_3C_2-containing MgH_2 was reduced from 278 °C to 185 °C (**Fig. 2a**), and the hydrogen desorption amounted to 6.2 wt% H_2 within only 1 min at 300 °C (**Fig. 2b**). More importantly, the dehydrogenated sample could absorb hydrogen at room temperature and the hydrogen uptake amounted to 6.1 wt% H_2 within 30 s at 150 °C under 50 bar H_2 pressure (**Fig. 2c-d**). Further cycling measurements showed a good stability with a reversible hydrogen capacity up to 6.4 wt% H_2 over the first 10 cycles for the MgH_2-5 wt% Ti_3C_2 composite. The superior catalytic activity of Ti_3C_2 may be ascribed to the unique layered structure and the in situ formed metallic Ti. Afterwards, they synthesized a series of Ti-based catalysts (Mg-Al-Ti-F composite, $(Ti_{0.5}V_{0.5})_3C_2$, NbTiC and so forth) [62-64] by introducing V, Al or Nb element into Ti-C system to form their compounds. All of these catalyst-doped systems possess very good stability and low starting temperature for hydrogen desorption. For example, the MgH_2 doped with 9 wt% NbTiC started to release hydrogen from 195 °C, and the hydrogen desorption was up to 5.8 wt% H_2 in 30 min at 250 °C. Afterwards, the fully dehydrogenated sample took up 4.0 wt% H_2 within 15 min even at 50 °C under 50 bar H_2 pressure. After 10 cycles, the hydrogen capacity of the MgH_2-9 wt% NbTiC sample was evaluated to be 6.5 wt% below 300 °C, corresponding to 96% capacity retention [64].

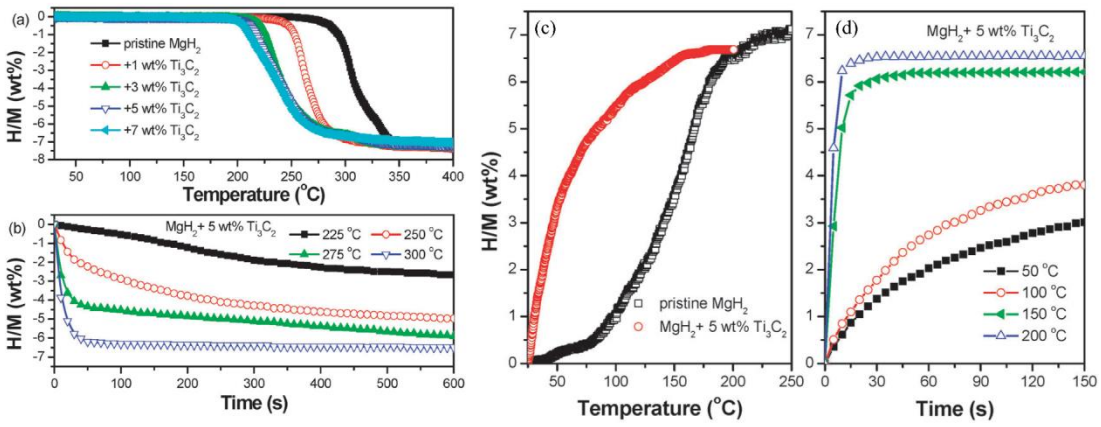

Fig. 2. Non-isothermal (a) and isothermal (b) dehydrogenation curves of the MgH_2-x wt% Ti_3C_2 samples. Non-

isothermal (c) and isothermal (d) hydrogenation curves of the dehydrogenated MgH_2-5 wt% Ti_3C_2 samples. Reprinted with permission from ref [60]. Copyright 2015 Royal Society of Chemistry.

(2) Metal oxides and metal halides

The transition-metal (TM) oxides, such as Nb_2O_5, TiO_2, V_2O_5, Cr_2O_3, Fe_3O_4, and other metal oxides, have been discovered for their catalytic effects upon hydrogen sorption and desorption of Mg-based hydrides, as reported by Hanada et al. [65, 66]. These metal nanoparticles can capture a large number of hydrogen molecules and provide pathways for hydrogen sorption on the surface of Mg-based materials. Some researchers [67, 68] focused on the hydrogen release/uptake behaviors of nanocrystalline MgH_2/Me_xO_y- and Mg_2NiH_4/Me_xO_y-systems (Me_xO_y = Sc_2O_3, TiO_2, V_2O_5, and Cr_2O_3, etc.) and found that these Mg-based materials catalyzed by the metal oxides showed fast sorption/desorption kinetics. In the absorption process, the catalytic effect of TiO_2, V_2O_5, Cr_2O_3, Mn_2O_3, Fe_3O_4, and CuO was comparable, whereas Fe_3O_4 showed the fastest desorption kinetics followed by V_2O_5, Mn_2O_3, Cr_2O_3, and TiO_2. In later studies, Nb_2O_5 showed the first-rank catalytic activity among numerous TM oxides in both absorption and desorption processes [69]. The catalytic effect from Nb_2O_5 upon Mg showed that hydrogen absorption occurred within 1min for 7 wt% H_2 and it took 2.2 min for hydrogen desorption at 300 °C [70]. In addition, Sabitu et al. [71] also demonstrated the consistent result, and they compared the effect of TM oxides (Nb_2O_5 > Fe_3O_4 > CeO_2 > ZrO_2) on the hydrogen evolution of MgH_2. Recently, Liu's group systematically studied the catalytic properties of transition metal-based oxides upon the hydrogen storage performance of MgH_2, especially focusing on Ti-/V-based materials [72-74]. They found that the porous carbon-supported TiO_2 nanocomposite (TiO_2@C) exhibited superior catalytic activity, wherein the carbon

structures could facilitate the further enhancement of the catalytic activity of TiO_2 by accelerating the diffusion of hydrogen within bulk MgH_2 resulting from an increase in transfer channel. The MgH_2-10 wt% TiO_2@C composite rapidly released hydrogen from 205 °C with the hydrogen absorption over 6.5 wt% H_2 within 7 min at 300 °C (**Fig. 3a**). The dehydrogenated sample took up hydrogen even at room temperature under 50 bar H_2 pressure (**Fig. 3b**), and approximately 6.6 wt% hydrogen was absorbed within 10 min at 140 °C, as shown in **Fig. 3c**. Moreover, the MgH_2-10 wt% TiO_2 sample exhibited good cycle stability with the de-/hydrogenation behaviors remaining at ca. 6.2 wt% H_2 over 10 cycles in **Fig. 3d**, corresponding to a capacity retention of 96.8% [72]. Similarly, the nano-V_2O_3@C composite also possessed superior catalytic effects on the hydrogen storage reaction of MgH_2, where the MgH_2 doped with 9 wt% nano-V_2O_3@C could absorb ca. 6.4 wt% of hydrogen in 20 min at 275 °C and the rehydrogenation was completed within 700 s at 150 °C under same hydrogen pressure [74]. Afterwards, they found that the onset dehydrogenation temperature of MgH_2 in the presence of the nitrogen-stimulated Nb_2O_5 (MgH_2-10 wt% N-Nb_2O_5 composite) could be downshifted to 170 °C [75]. Significantly, the full hydrogenation from the dehydrogenated sample could be achieved at temperature as low as 70 °C under 50 atm of hydrogen pressure with an available hydrogen capacity of 6.3 wt% H_2.

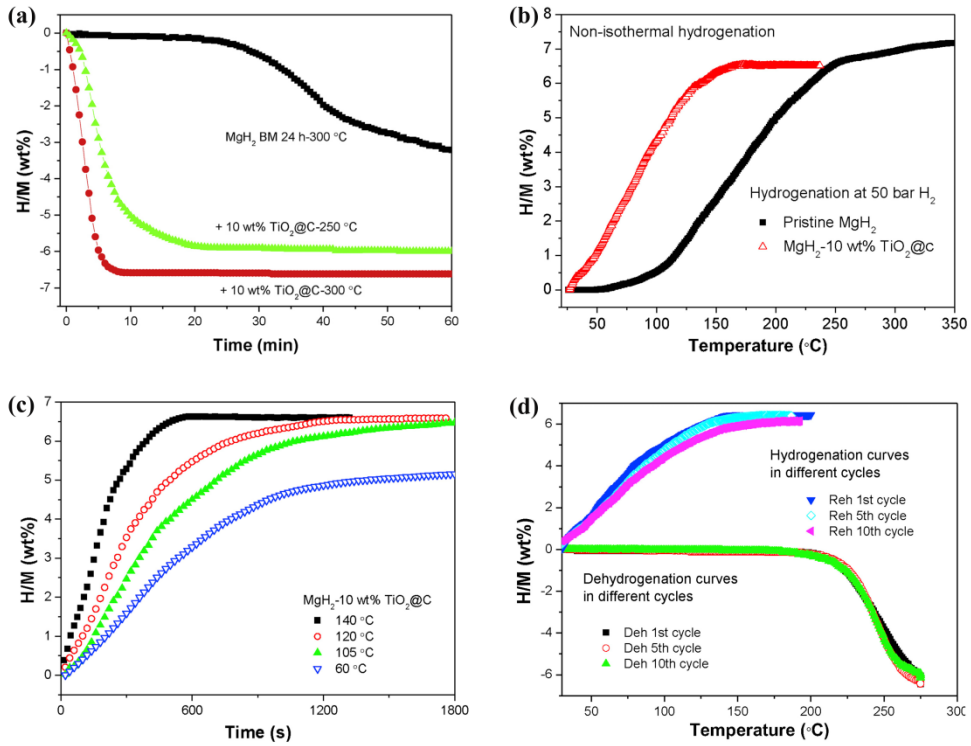

Fig. 3. (a) Isothermal dehydrogenation curves, (b) non-isothermal hydrogenation curves and (c) re-dehydrogenation curves of milled MgH_2 doped with and without 10 wt% TiO_2@C. (d) Non-isothermal dehydrogenation/hydrogenation cycling curves of the MgH_2-10 wt% TiO_2@C sample. Reprinted with permission from ref [72]. Copyright 2018 Elsevier.

With respect to metal halide dopants (such as ZrF_4, TaF_5, NbF_5, TiF_3, and $TiCl_3$, etc.), most of them play positive roles on the kinetics of re-/dehydrogenation of MgH_2 [76, 77]. Malka et al. [76] discovered that both ZrF_4 and NbF_5 could reduce the total sorption time of MgH_2 to 1.5 min with 6.3% of hydrogen uptake at 325 °C. Meanwhile, the hydrogen desorption rate is most rapid in MgH_2/ZrF_4, followed in order by NbF_5, $TiCl_3$, and TaF_5. The hydrogen release/uptake of MgH_2 catalyzed by different metal hydrides at 325 °C are summarized in **Table 4**.

Recently, Cui et al. [41, 78] synthesized a multi-phase and multi-valence Ti-based catalyst (Ti,

TiH_2, $TiCl_3$, and TiO_2) coated on the surface of milled Mg powders (~1 μm in diameter), which could significantly accelerate the hydrogen desorption from MgH_2. The MgH_2-coated Ti-based system started to release H_2 at about 175 °C and desorbed 5 wt% of H_2 within 15 min at 250 °C, with the apparent Ea reduced to 30.8 kJ/mol H_2. They believed that the multiple-valence Ti sites facilitated electron transfer among them, and thus acted as the intermediate during electron transfer between Mg^{2+} and H^-. **Fig. 4** presents the transmission electron microscopy (TEM) bright-field micrograph and selected area electron diffraction (SAED) of multi-valence Ti-based catalyst, whereas **Fig. 5** demonstrates the schematic diagram of the catalytic mechanism in the de-/hydrogenation process. The electron transfers in dehydrogenation process is proposed in the following steps: (1) H^- at the interface of MgH_2/Ti-compounds donates e^- to high valence Ti ($Ti^{3+/4+}$) which captures e^- and transforms into low valence Ti (Ti^{2+}) simultaneously; (2) as the weakened Mg-H bond is broken, the dissociative H is produced and dehydrogenation reaction occurs; (3) H atoms are recombined into H_2; (4) Mg nucleates and grows coupled with H_2 recombination. Conversely, the hydrogenation process can be described as the following steps: (1) H_2 dissociates into H; (2) low valence Ti (Ti^{2+}) donates e^- to H and transforms into high valence Ti ($Ti^{3+/4+}$); (3) Mg-H bonding is formed and the hydrogenation reaction is induced; and (4) MgH_2 nucleates and grows. Thus, the de-/hydrogenation process of MgH_2 is promoted due to the lowered barrier in the above inferred catalytic process. Then, Lin et al. [79] developed a facile and efficient method to fabricate novel symbiotic $CeH_{2.73}/CeO_2$ catalyst in-situ formed in Mg-based hydrides via controllable hydrogenation and oxidation treatments of amorphous Mg-Ce-Ni alloy. **Fig. 6** shows TEM pictures of the typical symbiotic morphology for the $CeH_{2.73}/CeO_2$ nanoparticles. **Fig. 7** presents the microstructural evolution of the symbiotic $CeH_{2.73}/CeO_2$ particles during

dehydrogenation and theoretical calculations. It was revealed that the superior catalytic activity was ascribed to the spontaneous hydrogen release effect at the $CeH_{2.73}/CeO_2$ interface with different valence of Ce.

Table 4. De-/sorption kinetics for MgH_2 milled without additives and with halide dopants at 325 °C [76].mission f

Sample	Time to reach 90% total absorption (min)	Time to reach 90% total desorption (min)
MgH_2-milled	3	Over 8
$MgH_2 + TaF_5$	2	8
$MgH_2 + TiCl_3$	2	4.5
$MgH_2 + ZrF_4$	1.5	3
$MgH_2 + NbF_5$	1.5	2.2

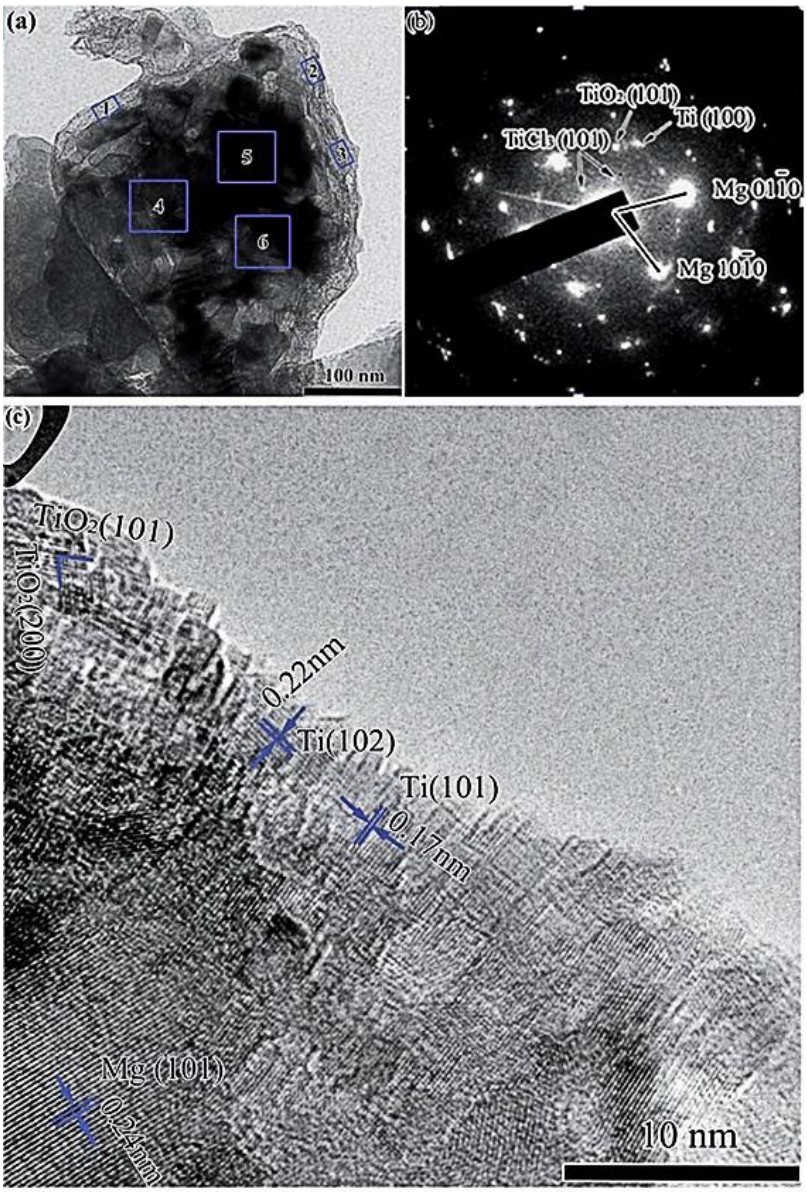

Fig. 4. TEM micrographs of the multi-valence Ti-based catalyst as-prepared. (a) Bright field pattern. (b) Electron diffraction pattern. (c) HR-TEM images. Reprinted with permission from ref [41]. Copyright 2013 Royal Society of Chemistry.

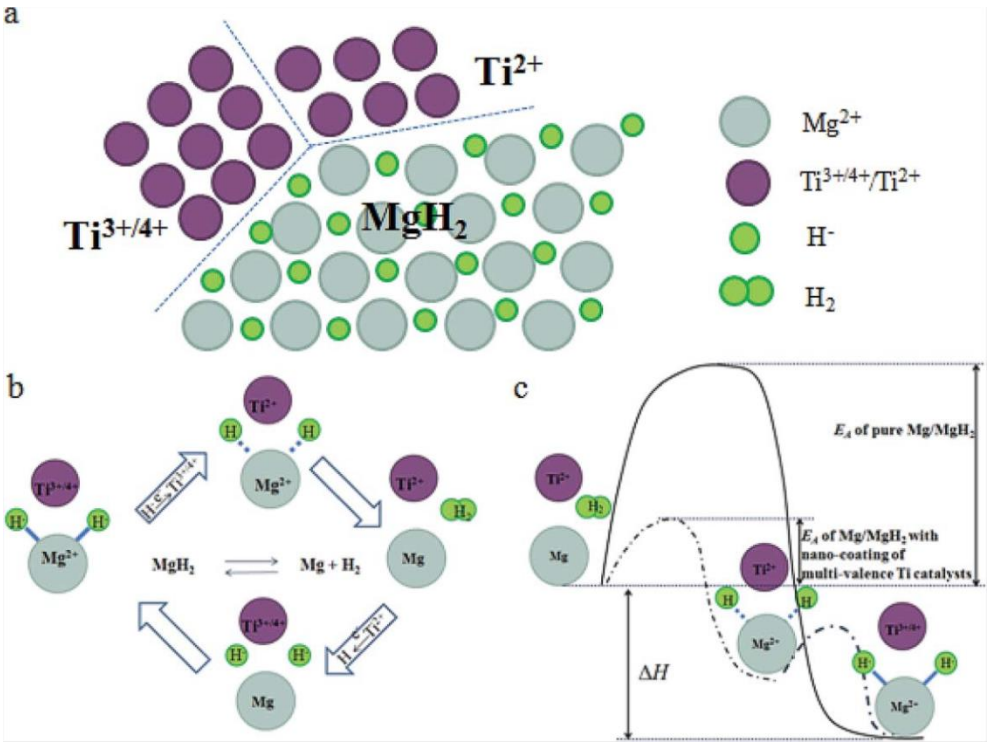

Fig. 5. The schematic diagram of the catalytic mechanism in de-/hydrogenation of Mg-multiple valence Ti composites. Reprinted with permission from ref [41]. Copyright 2013 Royal Society of Chemistry.

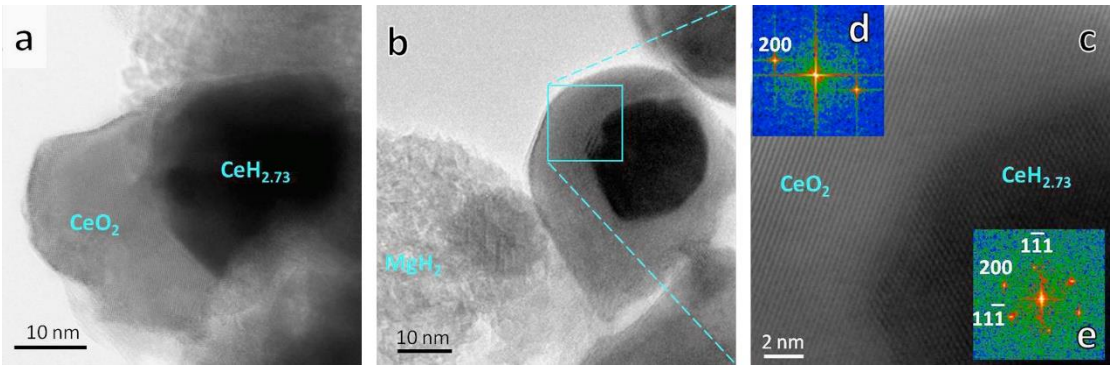

Fig. 6. Microstructure characterizations. (a) HRTEM image of typical symbiotic $CeH_{2.73}/CeO_2$ nanoparticles. (b) TEM image of symbiotic $CeH_{2.73}/CeO_2$ nanoparticles with core–shell structure. (c) HRTEM image showing the magnified area in b. The insets are the corresponding FFT patterns of (d) the outer and (e) inner layers of the core-

shell structure. Zone axis [011]. Reprinted with permission from ref [79]. Copyright 2014 Elsevier.

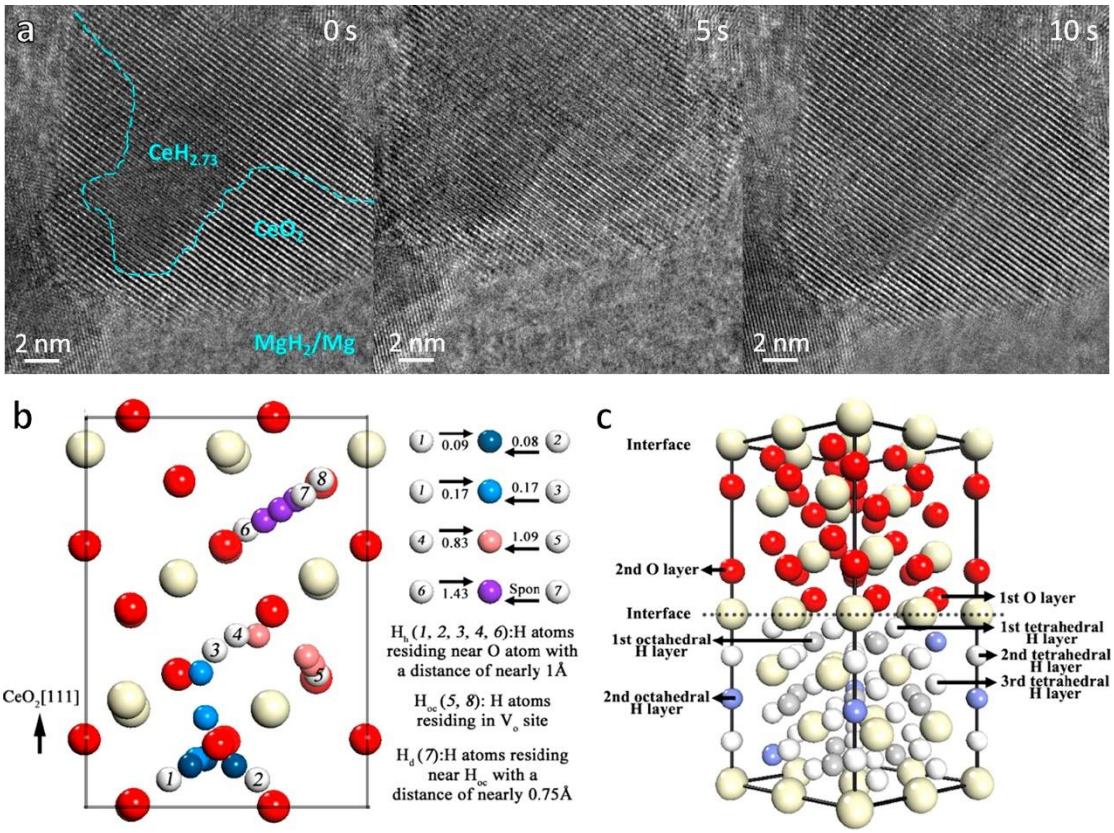

Fig. 7. In situ dehydrogenation and theoretical calculations. (a) The lattice fringe evolution of the symbiotic $CeH_{2.73}/CeO_2$ particles during dehydrogenation. (b) Theoretical model and hydrogen migration barriers of CeO_2 bulk inside view. (c) The arrangement positions of atoms at the $CeH_{2.73}/CeO_2$ interface. Reprinted with permission from ref [79]. Copyright 2014 Elsevier.

(3) Carbon-based nanostructures

Carbon-based materials (carbon nanotubes, activated carbons, and graphene) have present great potentials as H-storage materials from the viewpoint of numerous advantages, such as low cost, light-weight, high surface areas, pore structures, and high chemical stability, etc. Relative early reports upon carbon nanotubes demonstrated that they may be suitable candidates due to their considerable H-storage capacities, and thus triggering substantial researches all over the world [80].

Recently, carbon-based materials have been extensively applied to enhance H-storage performance of Mg-based hydrides [20, 81]. Wu and co-authors [82] investigated the hydrogen behaviors of MgH_2/Mg with various carbon materials. The hydrogen capacity of all Mg/C composites was over 6.0 wt% in 5 min at 300 °C. Particularly, the H-amount for the composites with ~5 wt% of SWNTs (single-walled carbon nanotubes) or C_{60} (fullerene) could reach ~6.7 wt% H_2 within 2 min, higher than 5.5 wt% H_2 for pristine Mg in 10 min. The main obstacle lies in relative low loading ratio (< 20 wt% Mg), because of the unfavorable wetting of molten Mg upon carbon. Further efforts demonstrated that the troublesome issue could be greatly enhanced with the addition of Ni, of which the H-desorption temperature was closed to that of Mg_2NiH_4 for ~50 wt% of MgH_2 loading capacity with trace of Ni ($Mg_{0.95}Ni_{0.05}$) [83].

Recently, Yu and co-authors [42] reported bottom-up self-assembly of MgH_2 anchored on graphene induced by the hydrophobic interaction between graphene and alkyl metallic compounds, resulting in massive monodisperse MgH_2 nanoparticles (< 5 nm) distributed uniformly upon the graphene. Notably, no visible aggregation occurred, even for a loading amount of MgH_2 up to 75 wt% (**Fig. 8**), delivering a practical H-capacity of the loading system as high as 5.7 wt%. After the modification with Ni addition, the peak temperature of graphene-75 wt% MgH_2 composites was downshifted to ca. 201 °C with a virtual H-capacity being 5.4 wt% in overall composite mass. Specifically, the above Ni-doped system could realize full hydrogen release at the temperature over 250 °C, delivering a H-capacity up to ~5.4 wt% in merely 30 min. For hydrogen uptake, the system could be fully hydrogenated in 60 min at 50 °C and gave ~2.3 wt% of H-absorption even at room temperature under same duration. The improved de-/hydriding kinetics could be ascribed to the lower activation energy (Ea), wherein the Ea for hydrogen absorption and desorption was

determined to be 22.7 and 64.7 kJ/mol, respectively, much lower than those for the bulk counterpart (99.0 and 158.5 kJ/mol for re-/dehydrogenation). Cycling tests indicated that a high reversible capacity of 5.35 wt% H_2, corresponding to a capacity retention of up to 99.2%, was still obtained after 100 consecutive cycles of H_2 sorption, with no loss in kinetic performance (**Fig. 9**). Apparently, the concept for assembling MgH_2 with high loading upon graphene may deliver an applicable strategy for designing other nanostructured composites with widespread applications in hydrogen energy or other energy-related fields.

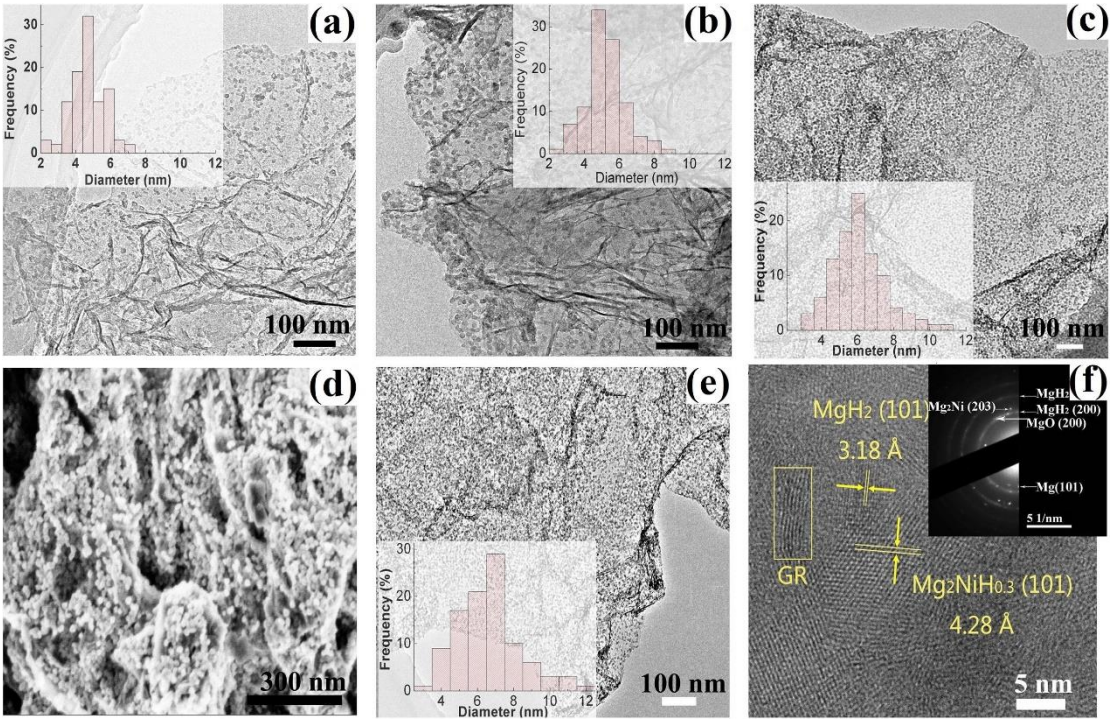

Fig. 8. TEM images of the MgH_2 nanoparticles supported upon the graphene with a weight ratio of (a) 20 wt% MgH_2, (b) 40 wt% MgH_2, (c) 75 wt% MgH_2, and (e) 75 wt% MgH_2 with Ni addition; (d) cross-sectional SEM image of 75 wt% MgH_2; (f) HRTEM image of Ni added 75 wt.% MgH_2 sample. Reprinted with permission from ref [42]. Copyright 2015 Wiley Online Library.

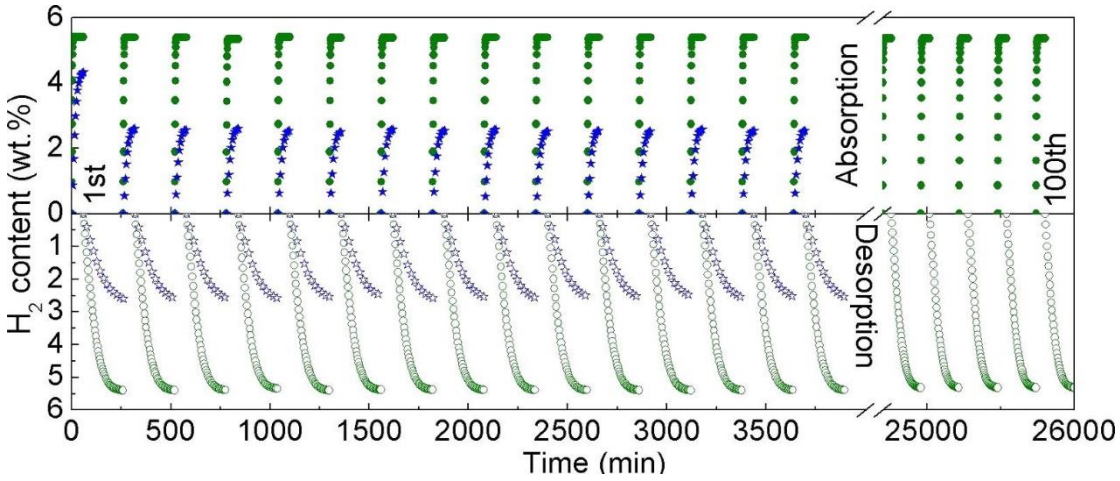

Fig. 9. Reversible hydrogen absorption (under 30 bar H_2 pressure) and desorption (under 0.01 bar H_2 pressure) of Ni added 75 wt% MgH_2 sample (circles) and 75 wt.% MgH_2 sample (stars) at 200 °C, respectively. Reprinted with permission from ref [42]. Copyright 2015 Wiley Online Library.

2.3. Thermodynamic tuning of Mg-based alloys

2.3.1. Alloying

Alloying, initially proposed by Reilly and Wiswall [34], was utilized to tailor sorption and desorption properties by weakening the bonding strength between hydrogen and metal. They found that Mg_2Ni could react readily with H_2 to form Mg_2NiH_4 with the ΔH being -64 kJ/mol H_2 under 2.0 MPa H_2 pressure and at 325 °C, whereas it suffered from drastically reduction in hydrogen capacity of 3.6 wt%. Morinaga et al. [84] revealed that H-Ni interaction in Mg_2NiH_4 was much weaker than H-Mg bonding in MgH_2, accounting for a lower formation enthalpy of Mg_2NiH_4. Another attractive compound is Mg_2FeH_6 [85], of which the gravimetric and volumetric hydrogen densities are up to 5.5 wt% and 150 kg H_2/m^3, respectively. Unfortunately, the formation enthalpy (ΔH) is -82 kJ/mol H_2, even higher than that for MgH_2. Moreover, there is no stable compound in Mg-Fe system, thus Mg_2FeH_6 is often obtained by reacting MgH_2 with Fe under H_2 pressure [86,

87]. Similarly, Mg_2CoH_5 (H-capacity of 4.5 wt%) can be prepared by above-mentioned methods [87, 88]. The formation enthalpy (ΔH) of Mg_2CoH_5 is -82 kJ/mol H_2, which is identical to that of Mg_2FeH_6, thereby delivering poor reversibility for both Mg_2CoH_5 and Mg_2FeH_6.

Recently, a series of Mg-RE-H (La, Ce, Nd, etc.) hydrides [89, 90] have received much attention, owing to superior hydrogen absorption features of Mg and RE. Ouyang et al. [91] found that Mg_3La exhibited rapid hydrogenation and dehydrogenation kinetics. PCI profiles of Mg_3La alloys obtained at various temperatures are shown in **Fig. 10**, the maximum hydrogen uptake capacity of Mg_3La is ~2.89 wt% at room temperature. It takes < 4 min for Mg_3La to absorb 90% of its full hydrogen content at room temperature under 35 bar H_2 pressure, whereas hydrogen release occurs at relatively elevated temperature (~274 ℃). Further results demonstrated that the structure of Mg_3La maintained unchanged after re-/dehydrogenation cycles [92, 93], indicating that the disproportionation reaction occurred in La_2Mg_{17} [94] did not appear here in Mg_3La alloy. The dehydriding enthalpy (ΔH) of the Mg_3La-H hydride was determined to be 81.0 kJ/mol H_2 according to Vant's Hoff equation from PCI curves. Resembling hydrogen release and uptake behaviors could be observed in Mg_3Nb-H [92] or Mg_3Pr-H system [95].

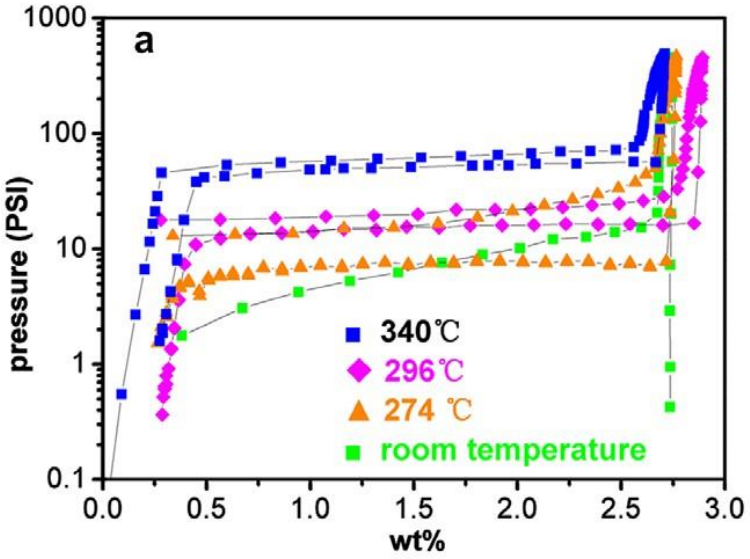

Fig. 10. PCI curves of Mg_3La-H system during hydriding/dehydriding process. Reprinted with permission from ref [91]. Copyright 2006 Elsevier.

2.3.1. Nanostructuring

Nanostructuring can not only overcome the kinetic barriers of Mg-based hydrides but also has a great effect on improving their thermodynamics, due to the special effects of nanosizing and boundary/surface [96, 97]. Some theoretical calculations and experimental results demonstrated that the introduction of extra boundary/surface can reduce the reaction enthalpy of Mg-H systems. Therefore, nanostructuring may be one of the most effective strategies to tune the thermodynamics of Mg-based hydrogen storage materials. Wagemans et al. [98] investigated the influence of crystallite size upon the thermodynamic stability of Mg/MgH_2 via using ab-initio calculations. The results showed that ΔH for hydrogen desorption was evaluated to be ~63 kJ/mol H_2 with the temperature at ~200 °C, as the MgH_2 cluster size reduced to 0.9 nm. Subsequent experimental results [99] also proved the remarkable thermodynamic destabilization as the particle size of the hydride downshifted to nanoscale (**Fig. 11**). Chen and co-workers [100] successfully prepared Mg nanowires with various diameters (**Fig. 12**) by the vapor-transport method. And they revealed that the desorption enthalpy of MgH_2 could be decreased by reducing the diameter of nanowires, where ΔH for dehydrogenation of MgH_2 nanowires with the diameters of 30-50, 80-100, and 150-170 nm were determined to be 65.3, 65.9, and 67.2 kJ/mol, respectively. Nevertheless, the nanoparticles grow up readily during de-/hydrogenation cycling process. To stabilize the nanostructures of Mg/MgH_2, nanoconfinement is developed to constrain the nanoparticles in a matrix or scaffold. For example, Konarova et al. [101] fabricated well-distributed MgH_2 nanocrystallites anchored in the

mesopores of host materials (CMK3/SBA15) by wet impregnation. MgH_2/CMK3 composites with 20 wt% loading amount present a desorption peak temperature of 253 °C (**Fig. 13**), corresponding to a decomposition enthalpy of 52 kJ/mol. These results indicated that the growth of Mg nanoparticles could be effectively restrained by nanoconfinement.

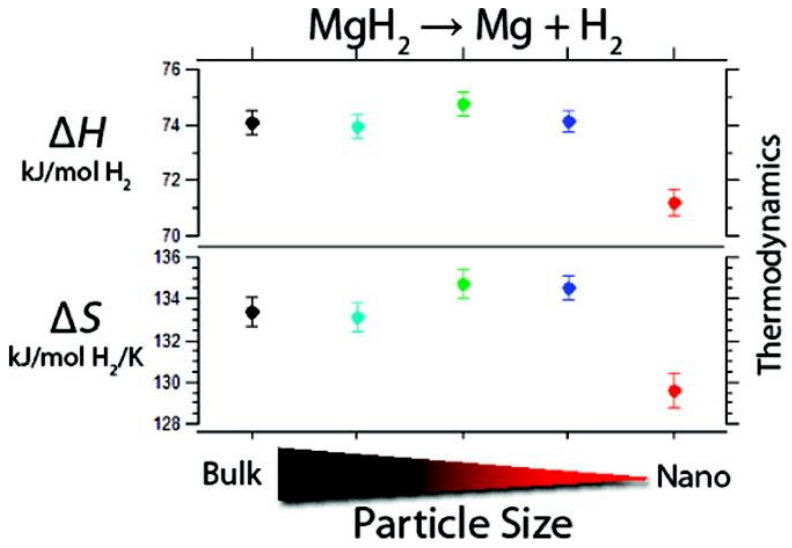

Fig. 11. The dehydrogenation thermodynamic properties versus Mg hydride nanoparticle size. Reprinted with permission from ref [99]. Copyright 2010 ACS Publications.

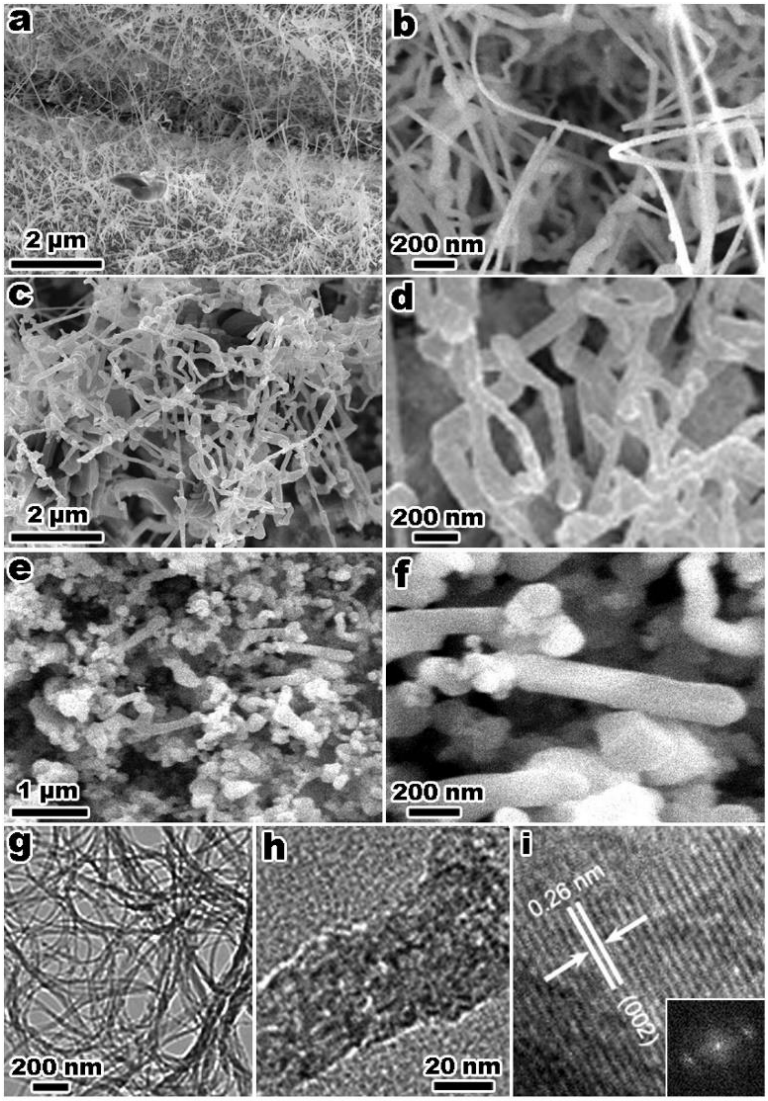

Fig. 12. SEM and TEM images of Mg nanowires with various diameters. Reprinted with permission from ref [100]. Copyright 2007 ACS Publications.

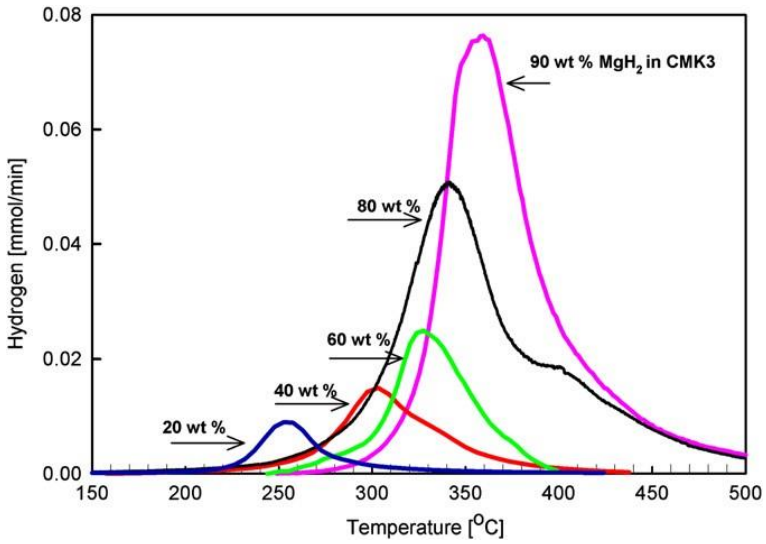

Fig. 13. TPD curves of MgH_2/CMK3 with various MgH_2 loadings measured at room temperature to 500 °C at a heating rate of 5 °C /min in helium flow. Reprinted with permission from ref [101]. Copyright 2013 Elsevier.

2.2.3. Altering reaction pathway

Altering reaction routes is one of the most effective approaches to tailor the poor thermodynamics of Mg-based hydrides. A well-known example is alloying with Si to destabilize the strongly bound of MgH_2 [44], of which more stable Mg_2Si (i.e. $2MgH_2 + Si \rightarrow Mg_2Si + 2H_2$) forms after dehydrogenation, resulting in the equilibrium pressure ranging from 1.8 to > 7.5 bar at 300 °C. The standard enthalpy of dehydrogenation for the MgH_2-Si system is reduced from 75.3 kJ/mol for MgH_2 to 36.4 kJ/mol H_2 with a H-capacity of ~5.0 wt% H_2. Unfortunately, the MgH_2/Si composite suffered from the poor reversibility and slow kinetics. Catalysts, such NbF_5, TiO_2, and other additives were used to enhance the kinetics [102], whereas the reaction was still incomplete even after 5 h at 250 °C. Homogeneously, Walker's group [103] milled MgH_2 with Ge and thus gave rise to a thermodynamic destabilization of 61 kJ/mol H_2, corresponding to a greatly reduced dehydrogenation temperature of 130 °C. The destabilization also occurred in the MgH_2-Al system, in which the desorption temperature was reduced to 255 °C under 1 bar H_2 pressure [50].

Recently, a fully reversible reaction in Mg-In-H system with destabilizing thermodynamics was realized by Zhong et al. [45]. The hydriding/dehydriding reactions of Mg (In) solid solution could be described as: Mg (In) + H_2 ↔ MgH_2 + β. In situ high-temperature X-ray diffraction (XRD) analysis on the dehydrogenation revealed that Mg_2In and ordered MgIn compounds transformed into the disordered MgIn compound (β phase), then reacting with MgH_2 to form the Mg (In) solid solution, and vice versa (As shown in **Fig. 14**). The reaction enthalpy change of $Mg_{0.95}In_{0.05}$ solid solution was decreased from 77.9 for pure Mg to 68.1 kJ/mol H_2 with a H-capacity over 5.0 wt% H_2. Subsequently, Zhu et al. [104] successfully synthesized the Mg (In, Al) ternary solid solution and investigated the reversible de-/hydriding behaviors of the alloy. The aim was to partially substitute expensive and heavy In with cheap and light-weight Al due to the relatively high solubility of Al in Mg. The PCI desorption curves of $Mg_{0.9}In_{0.05}Al_{0.05}$ alloy at different temperatures are shown in **Fig. 15**, of which the H-capacity is ~5.0 wt% H_2 with a desorption enthalpy of 66.3 kJ/mol H_2. The value is slightly lower than that of $Mg_{0.95}In_{0.05}$ with the same In content. Unfortunately, both Mg (In) and Mg (In, Al) alloys are plagued by harsh kinetics. To enhance the poor kinetics of Mg (In) solid solution, Fang's group [105] applied some Ti-based intermetallic alloys to catalyze the solid solution. The hydrogen desorption rate was highly accelerated by introducing $TiMn_2$ as a catalyst, wherein the Mg-0.1In alloy hydride was fully dehydrogenated at 150 ℃ within 3 h with an onset dehydrogenation temperature at approximately 100 ℃. Meanwhile, the temperature of the alloy was downshifted to 262.9 ℃ under 0.1 MPa H_2 pressure, which is 16 ℃ lower than that for pristine MgH_2. In addition, Vajo et al. [44, 106] and Bösenberg et al. [107, 108] proposed a new destabilized system consisting of $LiBH_4$ and MgH_2. The de-/hydrogenation reaction of $LiBH_4$-MgH_2 composite could be expressed as: MgH_2 + $LiBH_4$ ↔ 2LiH + MgB_2 + $4H_2$, where the

dehydrogenation enthalpy was reduced to 40.5 kJ/mol H_2. We will discuss the reactive hydride composites in the next section in detail.

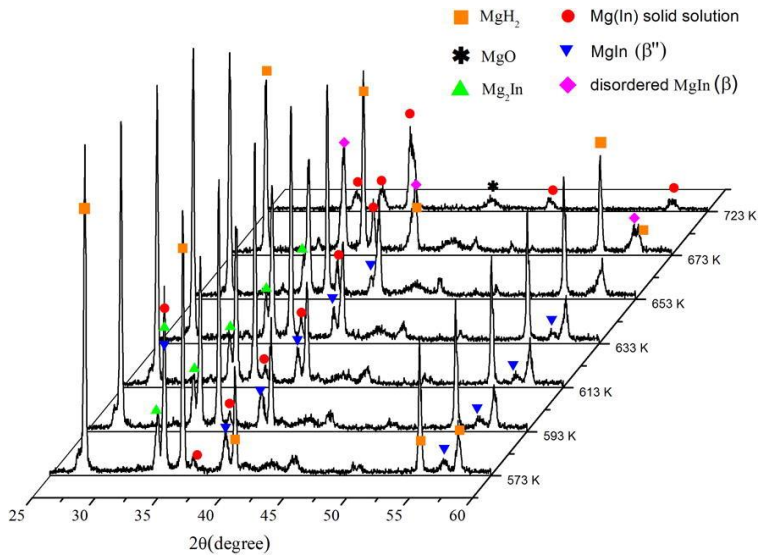

Fig. 14. In situ XRD patterns for the dehydrogenation of a hydrogenated Mg(In) sample at different temperatures. Reprinted with permission from ref [45]. Copyright 2011 Elsevier.

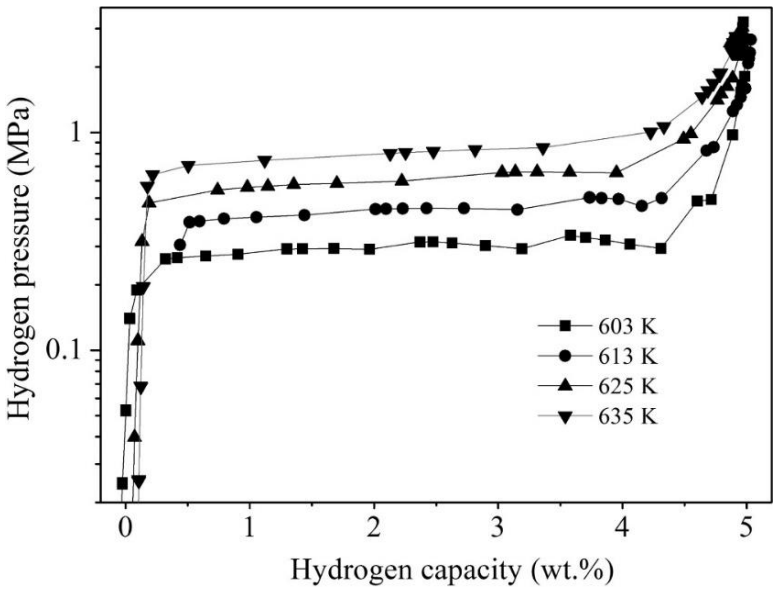

Fig. 15. PCI curves of $Mg_{0.9}In_{0.05}Al_{0.05}$ alloy. Reprinted with permission from ref [104]. Copyright 2014 ACS Publications.

2.4. Thermodynamic and kinetic dual tuning of Mg-based alloys via multiphase compositing

2.4.1. Establishing multiphase composite systems

Single-phase hydrogen storage materials are often unsuitable for practical applications. On the other hand, dual tuning of both thermodynamics and kinetics may be possible by taking advantage of the properties of individual phases. In this regard, the incorporation of catalysts and nanoscaling, or destabilization leading to Mg-based nanocomposite/multiphase systems appears promising. For instance, Wang et al. [109] synthesized the Mg-$ZrFe_{1.4}Cr_{0.6}$ composites via mechanically milling, in which Mg-40 wt% $ZrFe_{1.4}Cr_{0.6}$ exhibited superior hydrogenation properties, i.e., the highest hydrogen storage capacity (4.25 wt%) coupled with excellent kinetics. The composite remained relatively high H-capacity (2.4 wt%) and rapid absorption rate (< 5.5 min to reach 80% of the final capacity) even at 160 °C. Liang et al. [110] prepared Mg + LaH_3 + Mg_2Ni multiphase composites via mechanical milling Mg-50 wt% $LaNi_5$ powders, delivering superior hydriding/dehydriding kinetics at moderate temperatures (250-300 °C). Particularly, this composite enables a hydrogen absorption of 2.5 wt% H_2 in 500s under 15 bar H-pressure at ~29 °C, similar to the hydrogen behaviors occurred in Mg-FeTi(Mn) and Mg-CFMmNi_5 composites [111, 112].

Recently, Zhang et al. [113] and Liu et al. [114] synthesized Mg-Ni-Y nanocomposites consisting of a large quantity of long-period stacking ordered (LPSO) phases. Mg_{12}YNi alloy with an 18R-type LPSO phase at a crystalline size of 200-300 nm, as shown in **Fig. 16**, was hydrogenated into YH_2 and YH_3 with the average particle size of 10 nm at 300 °C. Afterwards, the in-situ formed fine YH_2 and YH_3 particles in de-/hydrogenation process could accelerate the dehydrogenation rate of the hydrogenated Mg_{12}YNi sample, delivering a H-desorption of 4.6 wt% at 300 °C in 6 min as well

as 4.2 wt% of H_2 even at 250 °C within 25 min [113]. Another ternary alloy $Mg_{91.9}Ni_{4.3}Y_{3.8}$ (**Fig. 17**) with a large number of 18R-type LPSO phase and a small quantity of 14H-type LPSO phase was prepared using rapid solidification [114]. Notably, the LPSO phases were transformed into MgH_2, Mg_2NiH_4, and YH_3 after the first hydrogenation, and the transformations could not be reversibly occurred during the subsequent hydrogenation reaction. The catalytic roles of YH_x and Mg_2NiH_4 substantially improved the hydrogen storage properties of the composite, rendering its reversible hydrogen sorption being ca. 5.8 wt%. Besides, this composite could achieve a full hydrogen release at 250 ℃. Ouyang et al. [43] reported that the dehydrogenation/rehydrogenation performance of Mg-based alloy was dramatically enhanced by combining the catalytic effect of in-situ formed Ni nanoparticles and "hydrogen pump" effect of $CeH_{2.73}$ in $CeH_{2.73}$-MgH_2-Ni nanocomposites obtained from the hydrogenation of as-melt $Mg_{80}Ce_{18}Ni_2$ alloy. The results showed that there were two steps in the hydrogenation of $Mg_{80}Ce_{12}Ni_2$ alloy: $Mg_3CeNi_{0.1} + H_2 \rightarrow Mg + Ni + CeH_{2.73} + H_2 \rightarrow MgH_2 + Ni + CeH_{2.73}$, where the $CeH_{2.73}$ hydride was preferentially formed with a crystalline size of ~5 nm as well as in-situ formed Mg and Ni at a crystallite size of ca. 25 nm (As shown in **Fig. 18** and **Fig. 19**). Due to the synergistic catalysis of Ni and $CeH_{2.73}$, this composite showed a reversible H-capacity of > 4.0 wt% H_2 with rapid kinetics and long cycling life, at a relative low desorption temperature. The full de-/hydrogenation cycle temperature of the system was reduced to 232 °C, ~100 °C lower than that for bulk Mg. The dehydrogenation activation energy was 63 kJ/mol H_2, much lower than that of Mg_3Ce alloy or pure Mg (104 and 158 kJ/mol H_2, respectively). More importantly, in-situ formed Ni nanoparticles located on the crystallite boundaries of $CeH_{2.73}$/Mg particles could restrain the migration of the crystallite boundaries, thus hindering the growth of grains. In the meanwhile, the existence of in-situ formed Ni enables the

transformation of $CeH_{2.73}$ into CeH_2, accounting for the higher practical hydrogen capacity. The hydrogen capacity remained up to 80% after 500 hydrogen absorption/desorption cycles (**Fig. 20**), wherein the capacity loss is mainly caused by the partial oxidation. Overall, the synergistic effect of in-situ formed Ni and $CeH_{2.73}$ in $CeH_{2.73}$-MgH_2-Ni nanocomposite enables thermodynamic and kinetic dual tuning for the composite, which may provide a novel strategy for tailoring the thermodynamics and kinetics of Mg-based alloys.

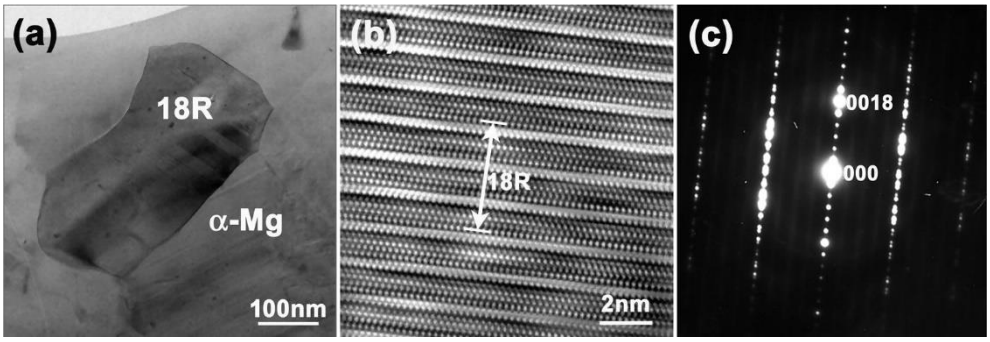

Fig. 16. (a) Bright-field TEM image, (b) high-resolution TEM image and (c) SAED pattern of the 18R phase in the crystallized $Mg_{12}YNi$ alloy. Reprinted with permission from ref [113]. Copyright 2011 Elsevier.

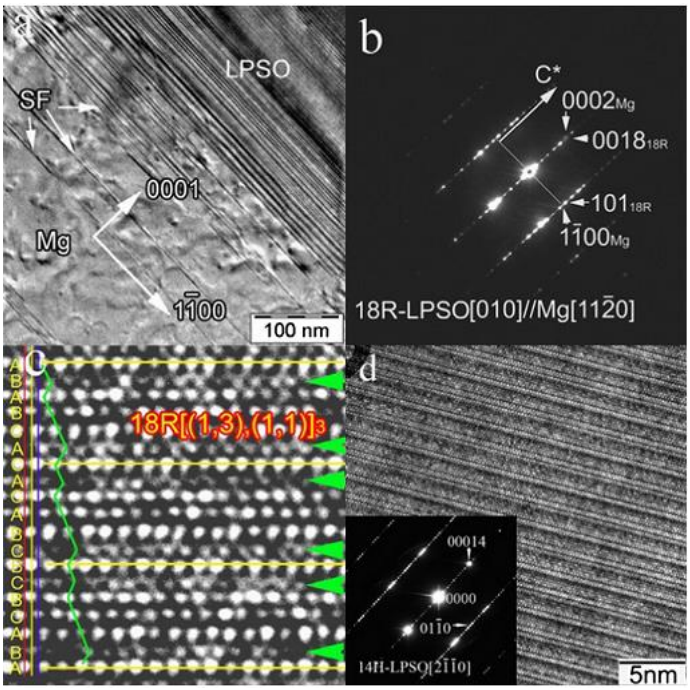

Fig. 17. The fine structure of $Mg_{91.9}Ni_{4.3}Y_{3.8}$ alloy with 18R- and 14H-LPSO phases. Reprinted with permission from ref [114]. Copyright 2013 Elsevier

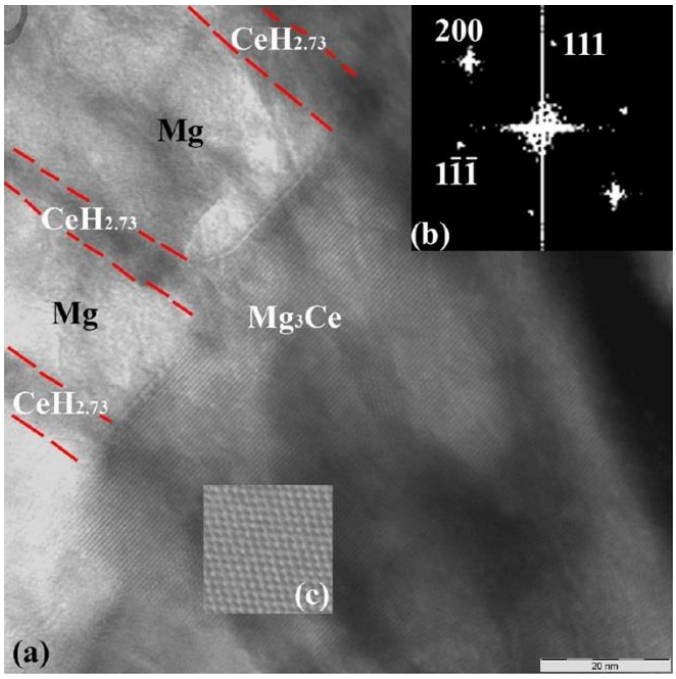

Fig. 18. TEM images of partially hydrogenated $Mg_{80}Ce_{18}Ni_2$ alloy. (a) Bright field image, (b) corresponding FFT patterns of Mg_3Ce (zone axis [01$\bar{1}$]), and (c) magnified HRTEM image of Mg_3Ce. Reprinted with permission from ref [43]. Copyright 2014 ACS Publications.

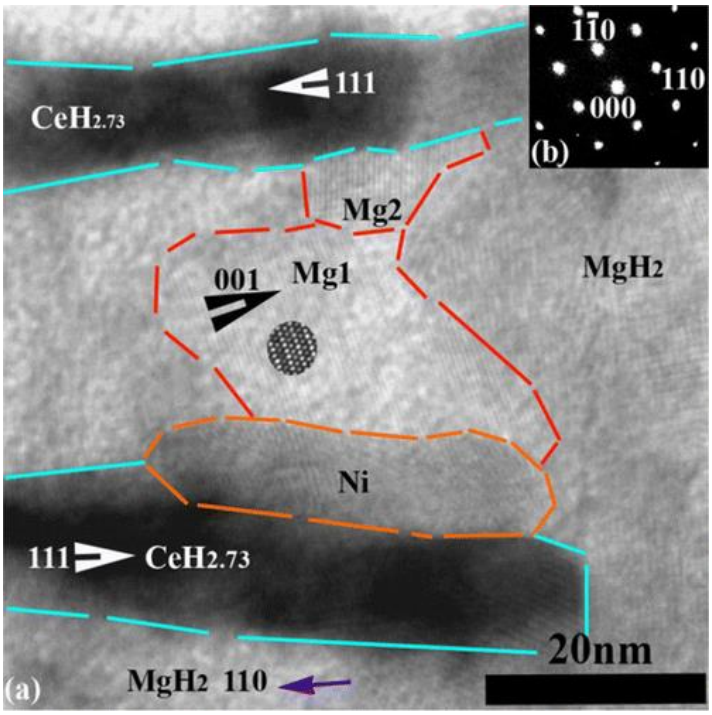

Fig. 19. TEM images of the microstructure of the partially dehydrogenated $CeH_{2.73}$-MgH_2-Ni sample demonstrate the catalyst effect of $CeH_{2.73}$ and Ni on MgH_2 dehydrogenation process. (a) Bright field TEM image of the in situ

formed $CeH_{2.73}$-MgH_2-Ni composite and (b) selected area diffraction patterns of MgH_2 (zone axis [011]). Mg nuclei preferentially nucleate along the surface of $CeH_{2.73}$/CeH_2 and Ni phase at the starting transition stage of MgH_2 to Mg during the dehydrogenation process. Reprinted with permission from ref [43]. Copyright 2014 ACS Publications.

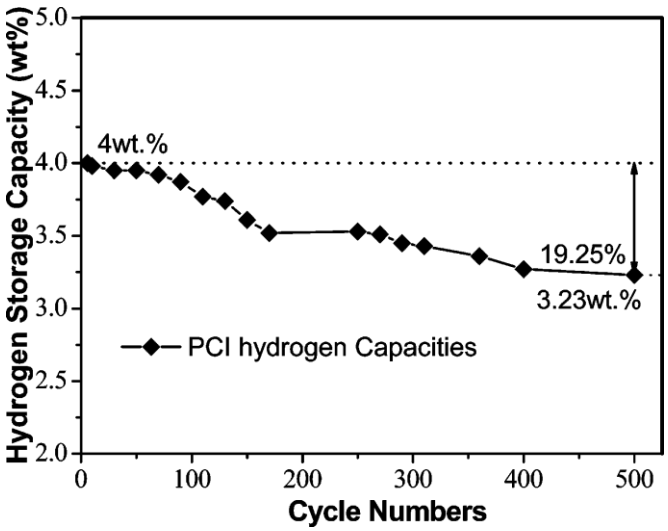

Fig. 20. Evolution of the maximum hydrogen sorption capacities versus cycle times of $CeH_{2.73}$-MgH_2-Ni composite. Reprinted with permission from ref [43]. 2014 ACS Publications.

2.4.2. Establishing novel Mg-based solid solution alloys

Both of the aforementioned Mg(In) binary [45] and Mg(In, Al) ternary solid solution [104] have achieved the thermodynamic regulation, but still suffer from poor kinetics. Ouyang et al. [115] synthesized Mg(In) solid solution with in-situ formed MgF_2 acting as a catalyst via plasma-assisted ball milling (P-milling), realizing the dual tuning of the thermodynamics and kinetics of MgH_2 with a H-capacity of ~5.16 wt% of H_2. As shown in **Fig. 21**, the dehydrogenation ΔH of the hydrogenated Mg(In)-MgF_2 composite is reduced to 69.2 kJ/mol from 79 kJ/mol H_2 for bulk MgH_2. Moreover, the dehydrogenation Ea is calculated to 127.7 kJ/mol H_2, much lower than those for pure MgH_2 (~160 kJ/mol) as well as Mg(In) binary (161 kJ/mol). Subsequently, they [46] successfully

synthesized $Mg(In)_2Ni$ solid solution by introducing In into Mg_2Ni. This system exhibited a completely reversible hydrogen capacity in hydrogen release/uptake cycles. Significantly, the Mg-In-Ni system achieved the dual tuning of the thermodynamics and kinetics of Mg_2Ni without catalysts, rendering the dehydrogenation Ea and ΔH being decreased from 80 kJ/mol and 64.5 kJ/mol H_2 to 28.9 kJ/mol and 38.4 kJ/mol H_2, respectively [34]. Similarly, the dual tuning of thermodynamic and kinetic properties of MgH_2 was realized in the $Mg_{85}In_5Al_5Ti_5$-MgF_2 system synthesized by P-milling (**Fig. 22** shows a synthesizing schematic illustration) [116]. The dehydrogenation ΔH and Ea for the hydrogenated $Mg_{85}In_5Al_5Ti_5$-MgF_2 composite were lowered to 65.2 kJ/mol H_2 and 125.2 kJ/mol H_2, respectively.

The dual tuning of kinetics and thermodynamics of Mg-based hydrides was also achieved in Mg-In-Y [117] and Mg-In-Ni ternary systems [118]. With regard to $Mg_{90}In_5Y_5$ solid solution [117], the reaction enthalpy of 62.9 kJ/mol H_2, was lower than that of $Mg_{95}In_5$ binary alloy (67.8 kJ/mol H_2) or pure Mg (74.1 kJ/mol H_2). The Ea for the dehydrogenation was reduced to 147 kJ/mol, slightly less than the value for pure MgH_2. In $Mg_{18}In_1Ni_3$ ternary system [118], the overall reversible H-capacity was ca. 3.8 wt%, and the lowest dehydrogenation temperature was downshifted to 230 °C (**Fig. 23**), much lower than both of Mg (315 °C) and $Mg_{95}In_5$ solid solution (313 °C). Also, two new Mg-In-Ni ternary alloy phases were reversibly formed in the two-step hydriding and dehydriding processes, where partial Ni participated in dehydrogenation reaction. Notably, the equilibrium pressure of the $Mg_{18}In_1Ni_3$ alloy was 3.62 bar at 300 °C, much higher than those of pure MgH_2 (0.96 bar) and $Mg_{95}In_5$ solid solution (2.23 bar) under the same conditions. On the other hand, the Ea for hydrogen desorption reaction was lowered to 107 kJ/mol H_2, which can be attributed to the addition of Ni.

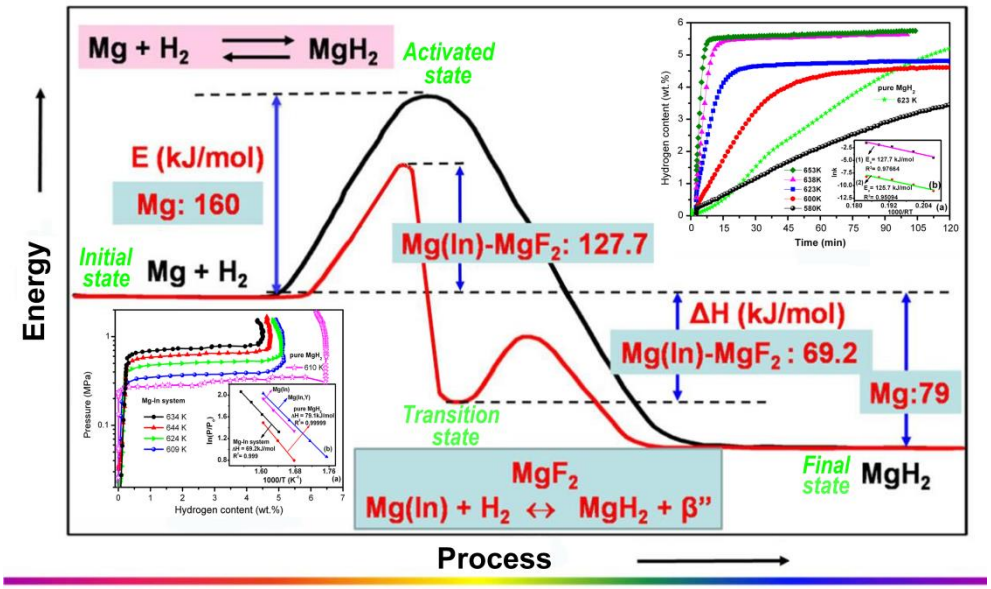

Fig. 21. The dual regulation of the thermodynamics and kinetics of Mg(In)-MgF_2 composite. Reprinted with permission from ref [115]. Copyright 2014 Elsevier.

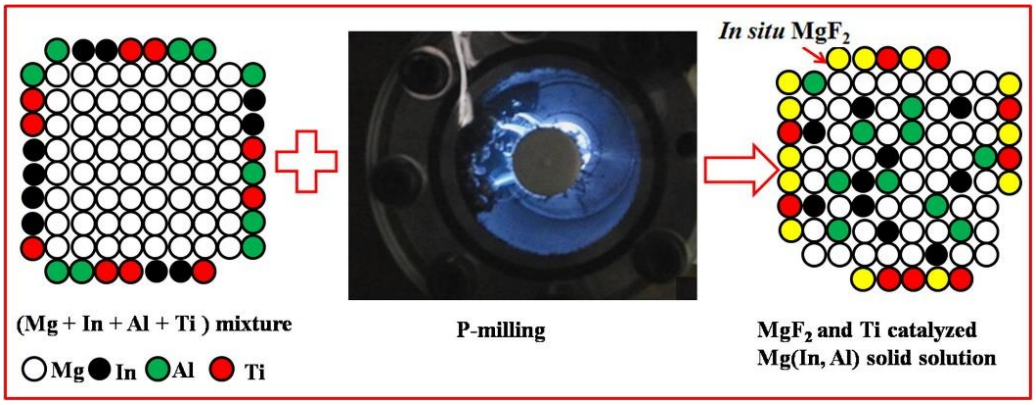

Fig. 22. Schematic illustration of the preparation process of the $Mg_{85}In_5Al_5Ti_5$ alloy by P-milling. Reprinted with permission from ref [116]. Copyright 2015 Elsevier.

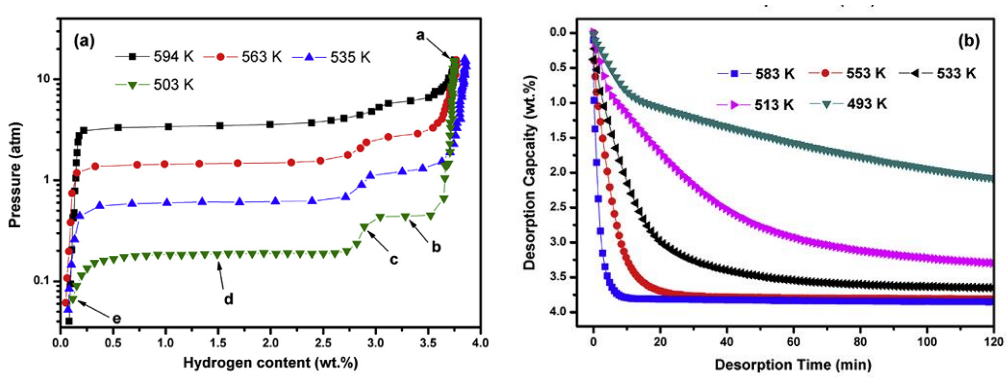

Fig. 23. PCI patterns and isothermal dehydrogenation kinetic curves of $Mg_{18}In_1Ni_3$ alloy. Reprinted with permission from ref [118]. Copyright 2014 Elsevier.

3. Complex hydrides

3.1. Overview

Complex hydrides, namely group I and II salts of $[AlH_4]^-$ (alanates), $[NH_2]^-$ (amides), and $[BH_4]^-$ (borohydrides), consist of an alkali or alkali earth metal cation and a coordination complex anion where hydrogen is covalently bonded to the central atom (Al, B, and N, etc.) [31]. In comparison with Mg-based materials and other traditional metal hydrides, complex hydrides have been in the limelight over the last few decades as solid-state hydrogen materials. Their unparalleled theoretical hydrogen densities make them promising candidates for a wide range of applications in on-/off-board hydrogen storage areas [4, 119]. The hydrogen supply of complex hydrides could be achieved via hydrolysis or thermolysis [120]. Compared to thermal composition, hydrogen supply from hydrolysis shows precisely controllable hydrogen release, high-purity H_2, and mild operating temperature, etc [119, 121, 122]. Nevertheless, the hydrolysis reactions are highly irreversible and cannot be applied for rechargeable hydrogen storage systems. Homogeneously, the difficulty in reversibly hydrogen uptake of pyrolysis products under moderate conditions, makes it impractical for vehicular commercial application [123, 124]. Not until the mid-nineties did a significant paradigm shift occur, when Bogdanovic observed reversible hydrogen sorption/desorption for titanium-catalyzed $NaAlH_4$ at mild conditions [125]. Followed by reversible nitrogen-based complex hydrides, e.g. $LiNH_2$-Li_2NH-LiH, discovered by P. Chen [126] in 2002 while A. Zuttel and K. Yvon and co-authors were among the first to investigate metal tetrahydroborates, e.g. $LiBH_4$

in 2003 [127, 128]. As the strength of the covalent bonds increases, so does the decomposition temperature of complex hydrides. Note that the strength of the covalent bond of complex hydrides is positively correlated with the Pauling electronegativity χP of element A in MAH_4 complex hydrides, such as $[BH_4]^-$ (borohydrides) and $[AlH_4]^-$ (alanates), where $[BH_4]^-$ (borohydrides) possess the higher Pauling electronegativity. With the same alkali or alkali earth metal element M, therefore, the complex hydride MBH_4 should be more stable than $MAlH_4$. **Table 5** presents the theoretical hydrogen capacity and decomposition temperature of some representative light-metal complex hydrogen storage materials. This review summarizes recent advances upon complex hydrides and effective strategies applied to improve the hydrogen release and uptake properties, such as catalyzing, nanostructuring, cation/anion substitution, and so on.

Table 5. Representative complex hydrides and theoretical hydrogen storage capacity [31].

Complex hydrides	Density (g/cm^3)	Gravimetric density (wt%)	Decomposition temperature (°C)
$LiAlH_4$	0.92	10.5	187
$NaAlH_4$	1.28	7.5	220
$Mg(AlH_4)_2$	-	9.3	135
$LiBH_4$	0.67	18.4	268
$NaBH_4$	1.07	10.7	505
KBH_4	1.17	7.5	585
$Mg(BH_4)_2$	0.99	14.8	260
$Al(BH_4)_3$	0.79	16.9	-64
$LiNH_2$	1.18	8.8	372
$NaNH_2$	1.39	5.2	210
$Mg(NH_2)_2$	1.39	7.2	360

3.2. Hydrogen supply via thermal decomposition in potential reversible systems

3.2.1. $LiAlH_4$/ $NaAlH_4$/$Mg(AlH_4)_2$ hydrogen storage systems

Alanates, one of most typical members of complex hydrides family, consist of a metal cation and a $[AlH_4]^-$ tetrahedron (where four hydrogen atoms are covalently bonded to a central aluminum

atom) connected through the ionic bond, such as $LiAlH_4$, $NaAlH_4$, and $Mg(AlH_4)_2$, etc. The crystal structures of the above alanates are shown in **Fig. 24**, where Li cations are surrounded by five isolated $[AlD_4]^-$ tetrahedral and Na atoms are surrounded by eight $[AlH_4]^-$ tetrahedral, whereas $Mg(AlH_4)_2$ shows six-coordinated Mg and four-coordinated Al in a distorted MgH_6 octahedral geometry. One engaging feature of alanates is that both lithium and sodium salts are readily available commercially. Also, $Mg(AlH_4)_2$ can be easily synthesized via a metathesis reaction between $NaAlH_4$ and MgH_2 [129]. Nonetheless, alkali metal alanates undergo hydrogen release at a relatively high temperature due to their intrinsic nature combining both ionic bonds and covalent bonds. For instance, not until the temperature of over 220 ºC does $NaAlH_4$ begin to release hydrogen slowly [31]. Moreover, the hydrogen desorption of $MAlH_4$ (where M = Na, Li, K) is a complicated and multi-step process (see in eq 1-3) which starts with melting of the hydride as well as trialkali metal, hexahydroaluminate (M_3AlH_6) as the intermediate, where the temperature and pressure of single-step reaction vary greatly [130, 131].

$$MAlH_4 \rightarrow 1/3M_3AlH_6 + 2/3Al + H_2 \quad (1)$$

$$1/3M_3AlH_6 \rightarrow MH + 1/3Al + 1/2H_2 \quad (2)$$

$$MH \rightarrow M + 1/2H_2 \quad (3)$$

Based on the extremely high decomposition temperature of MH, it may be unsuitable as the hydrogen storage material for practical vehicular applications [132]. To date, tremendous efforts have been made to solve the issues of hydrogen sorption/desorption thermodynamics and kinetics, including catalysis, nanostructuring and composite systems.

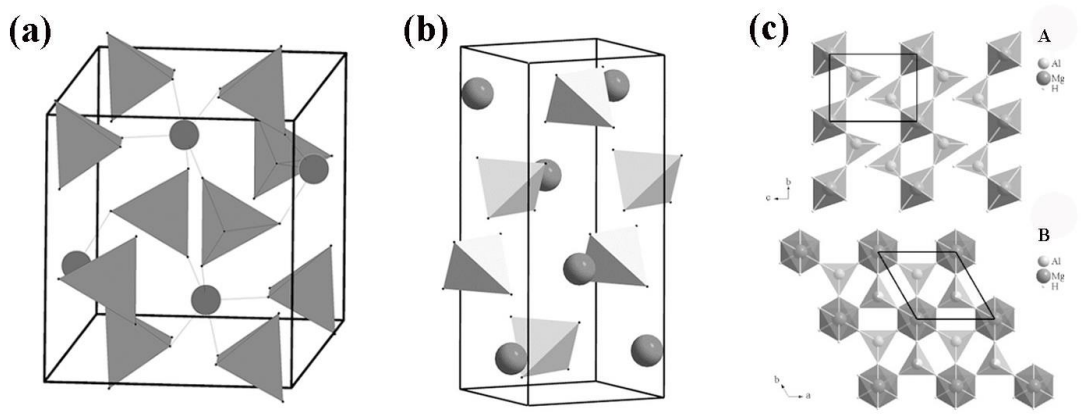

Fig. 24. The crystal structures of (a) $LiAlD_4$, where Li cations are surrounded by five isolated $[AlD_4]^-$ tetrahedra. Reprinted with permission from ref [133]. Copyright 2002 Elsevier; (b) $NaAlD_4$, in which Na atoms are surrounded by eight $[AlH_4]^-$ tetrahedra in a distorted square antiprismatic geometry. Reprinted with permission from ref [134]. Copyright 2003 Elsevier; (c) $Mg(AlH_4)_2$, showing six-coordinated Mg and four-coordinated Al in a distorted MgH_6 octahedral geometry. Views along (A) the a-axis and (B) the c-axis. Reprinted with permission from ref [135]. Copyright 2005 Elsevier.

(1) Catalysis

Since the successful discovery of the Ti-doped $NaAlH_4$ system with a reversible hydrogen capacity 3.1-4.2 wt% H_2 [125], great efforts on state-of-the-art dopant precursor and doping technologies have been made to explore the hydrogen release/uptake behaviors of alanates systems. Generally, the most favorable dopants for the $NaAlH_4$ system are still recognized to be Ti-based compounds. Initially, Majzoub et al. [136] and Anton's group [137], reported that the catalytic activity of TiF_3 is in accordance with that of $TiCl_3$. Subsequently, Wang et al. [138] synthesized Ti-doped $NaAlH_4$ composite by a multi-step mechanically ball milling method, where TiF_3 exhibited more superior hydrogen storage performance over analog $TiCl_3$, including the considerably reduced operating temperature and pressure conditions. Besides, Li et al. [139] found that TiN could also

significantly enhance the hydrogen desorption kinetics and lower the temperature of $NaAlH_4$. Interestingly, the onset dehydrogenation temperature of 2% TiC-doped system was reduced to ~130 ºC, and the dehydriding rate reached a maximum value at 183.5 ºC, with a hydrogen desorption of ~5.44 wt% at 190.0 ºC. The Ea for the first and second dehydrogenation steps in the TiN-$NaAlH_4$ system was determined to be 91.70 and 99.93 kJ/mol^{-1} H_2, respectively. They [140] also found that the Co-B catalyst could facilitate hydrogen desorption of $NaAlH_4$, of which the onset temperature was downshifted to 90 ºC with the Ea being only 67.95 kJ/mol^{-1}. Considering the reversible gravimetric hydrogen storage density of Ti-doped $NaAlH_4$ system, pure Ti was adopted to replace Ti-based halides to reduce the "dead-weight" of the system, whereas it suffers from extremely limited enhanced absorption/desorption performance [141]. It may be ascribed to good plasticity of Ti, thus it's hard to be well-dispersed in the vicinity of $NaAlH_4$ via ball milling process. To solve this issue, Fichtner et al. [142] doped small Ti clusters into $NaAlH_4$, in which the launching desorption temperature was 120 ºC with a hydrogen capacity up to ~5.0 wt%. The Ti-doped system could be fully hydrogenated within 35 min, and the hydrogen content maintained ~4.2 wt% even undergoing 20 cycles for de-/hydrogenation. However, the difficulty lies in the synthesis of nanoscale Ti. Recently, Liu et al. [143] successfully fabricated ultrafine metallic Ti nanoparticles (3-5 nm) supported on amorphous carbon (nano-Ti@C) through a facile, scalable calcination process. The as-received nano-Ti@C exhibited remarkable catalytic activity for hydrogen behaviors in $NaAlH_4$, wherein the $NaAlH_4$ doped with 7 wt% Ti@C released hydrogen from 75 ºC with an available hydrogen capacity of 5.04 wt% H_2 within 20 min at 140 ºC, as shown in **Fig. 25a**. Moreover, the dehydrogenated sample could absorb hydrogen at room temperature and full re-hydrogenation was achieved within < 3 min at 100 ºC under 120 bar H_2 (**Fig. 25b**.). As shown in

Fig. 25c. the reversible hydrogen capacity still maintained at 4.97 wt% after 100 cycles, corresponding to 98.6 wt% of capacity retention.

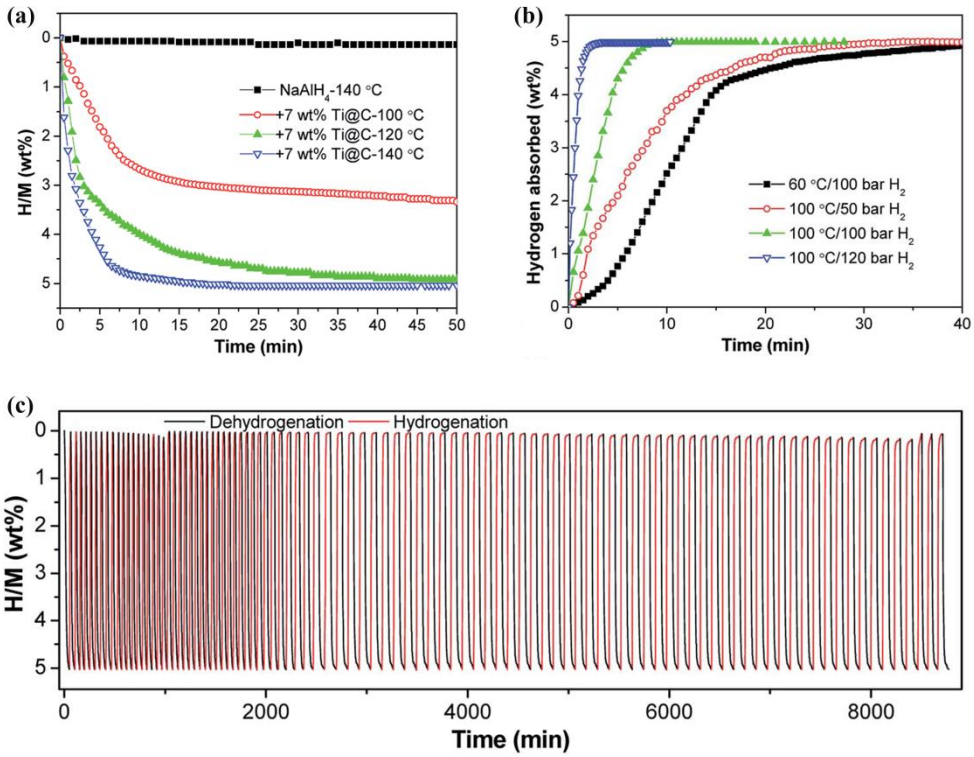

Fig. 25. (a) Isothermal dehydrogenation curves of nano-Ti@C-containing $NaAlH_4$, (b) isothermal hydrogenation curves of the dehydrogenated samples, (c) cycling curves of $NaAlH_4$-7 wt% nano-Ti@C. Reprinted with permission from ref [143]. Copyright 2019 Royal Society of Chemistry.

Rongeat and co-workers [144, 145] put forward a one-step mechano-chemical synthesis of $NaAlH_4$ with diverse additives ($TiCl_3$, $CeCl_3$, $ScCl_3$, etc.) and compared the reversible hydrogen release/uptake performance of various doped systems. The catalytic effect of the above dopants was followed by: $TiCl_3$ > $CeCl_3$ > $ScCl_3$ > Ti. In this regard, $TiCl_3$ exhibited optimal hydrogen desorption properties, whereas $CeCl_3$ was the best dopant for absorption. Bogdanovic´ et al. [146] applied trichlorids of Sc-, Ce- and Pr-doped as alternative dopants for $TiCl_3$, where $ScCl_3$ was found to be highly efficient, for either a nearly theoretical hydrogen capacity (> 4.5 wt% at ~125 ºC, expected

5.0 wt%) or fast kinetics with ~3 times desorption rate as high as the Ti-doped $NaAlH_4$ in **Fig. 26**. The Ce-doped system exhibited similar kinetics as Sc-doped one, absorbing 4.4 wt% of H_2 (calculated maximum: ~4.8 wt%) within 35 min under 10 MPa H-pressure and at 129 ºC. Especially, the $CeCl_3$-doped system showed excellent cycle stability, and no visible hydrogen capacity loss occurred even after 29-cycle tests. Recently, Hu et al. [147] compared the catalytic effect of Ce, CeH_2, $CeCl_3$ and $CeAl_4$ dopants upon the absorption/desorption performance of $NaAlH_4$. The results indicated that $NaAlH_4$ doped with the Ce-based precursors delivered excellent sorption kinetics and stable cycling capacity. The rehydrogenation of $CeCl_3$-doped system was able to be fulfilled in approximately 10 min. They considered $CeAl_4$ to be catalytic active center with the intermediate $CeAl_4$ being observed during sorption and desorption cycles. Furthermore, the $NaAlH_4$ system doped with $CeAl_4$ instead of $CeCl_3$ possessed higher hydrogen capacity, as a result of bypassing the formation of the ineffective NaCl. The highest capacity of 4.9 wt% H_2, close to the theoretical value, was obtained from $NaAlH_4$ doped directly with metallic cerium. Recently, Liu et al. systematically studied the catalytic properties of transition metal-based oxides or nitrides supported on porous carbon (TiO_2@C, ZrO_2@C, TiN@N-C, etc.) upon the hydrogen storage performance of $NaAlH_4$ [148-152]. For instance, the $NaAlH_4$-9 wt% TiO_2@C composite started releasing hydrogen from ~63 ºC and re-hydrogenated starting from 31 ºC (**Fig. 27b**). As shown in **Fig. 27a,** the doped system could rapidly release approximately 4.2 wt% H_2 (93% of the available hydrogen capacity) within 10 min at 140 ºC and desorb 4.1 wt% H_2 in 30 min at 140 ºC, and the full re-hydrogenation was achieved at temperatures as low as 50 ºC under 100 bar H_2 (**Fig. 27c**). More importantly, the nanocrystalline TiO_2@C-doping sample exhibited a quite good cyclability with the hydrogen capacity retention remaining 98.9% even after 10 cycles in **Fig. 27d-e** [148].

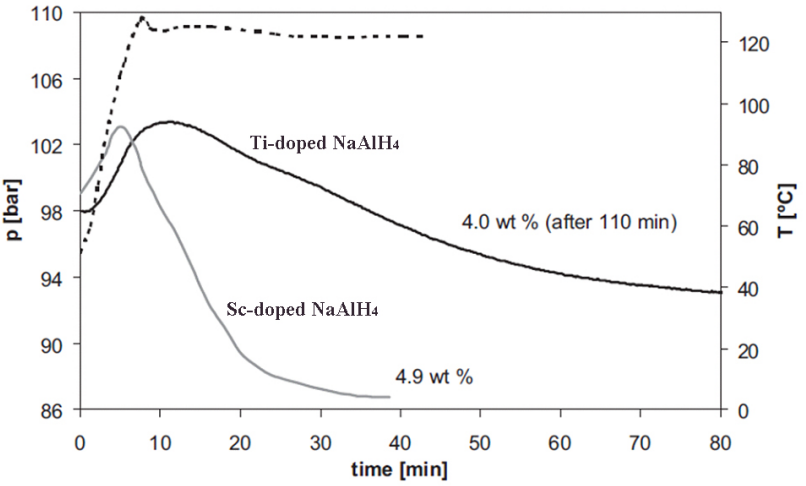

Fig. 26. Hydrogenation curves of Sc- and Ti-doped $NaAlH_4$ (2 mol%). The dashed line indicates the temperature within the hydride bed (heating rate 10 K min^{-1}). Reprinted with permission from ref [146]. Copyright 2006 Wiley Online Library.

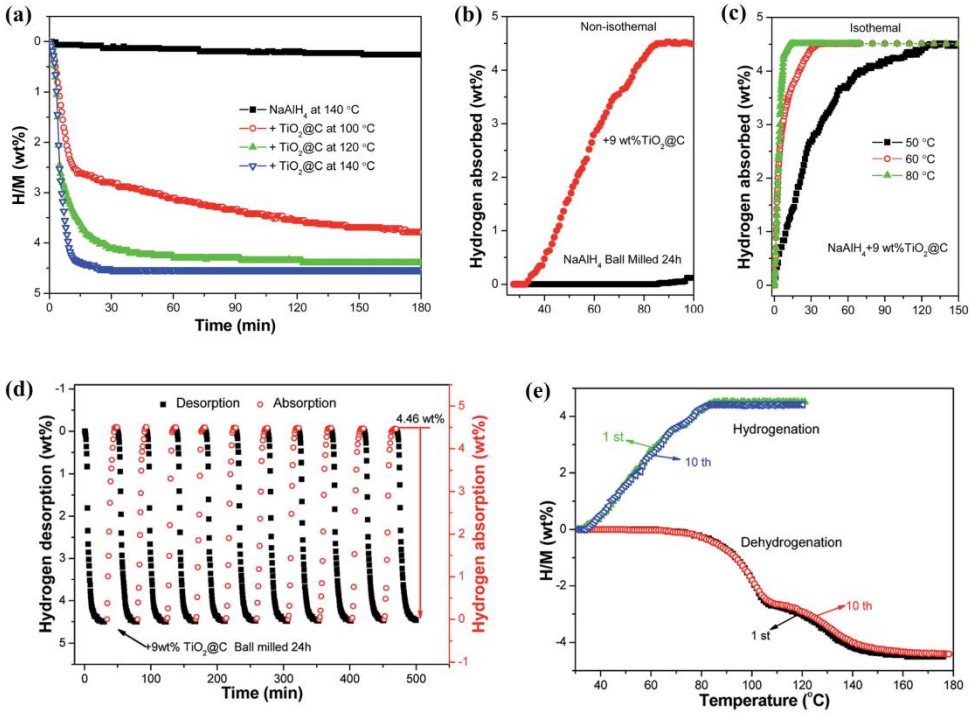

Fig. 27. De-/hydrogenation curves of the $NaAlH_4$ doped with and without TiO_2@C: (a) isothermal dehydrogenation, (b) non-isothermal hydrogenation and (c) isothermal hydrogenation. (d) Reversible H_2 absorption (at 100 ºC under 100 bar H_2) and desorption (140 ºC) of the 9 wt% TiO_2@C-containing sample. (e) Non-isothermal

dehydrogenation/hydrogenation curves (2 ºC min^{-1}) of the 9 wt% TiO_2@C-containing sample at the 1st and 10th cycles. Reprinted with permission from ref [148]. Copyright 2015 Royal Society of Chemistry.

Similarly, doping and catalyzing process could greatly enhance the hydrogen release performance of $LiAlH_4$ [153, 154]. Balema et al. [155] found that $LiAlH_4$ could be converted into Li_3AlH_6 and Al at ambient temperature after mechanical milling with 3 mol% $TiCl_4$ for 5 min. Chen and co-workers [156] found that the decomposition Ea of $LiAlH_4$ and Li_3AlH_6 was estimated to be 43 and 55 kJ/mol H_2, respectively. The initial dehydrogenation temperature was downshifted to 100 ºC after doping with 2 mol% $TiCl_3$. Compared to undoped $LiAlH_4$, the onset dehydrogenation temperature for the alanate doped with 2 mol% TiC was as low as 85 ºC and the dehydriding rate of the doped system was accelerated by 7-8 times at 115 ºC with the hydrogen release amount up to 6.9 wt% at 188 ºC [153]. The Ea for the dehydrogenation of $LiAlH_4$ and Li_3AlH_6 was estimated to be 59 and 70 kJ/mol H_2, respectively. Varin et al. [154] synthesized $LiAlH_4$ + 5 wt% nano-Ni composites via a ball milling process, which could release ~4.8 wt% of H_2 within 35 min at 120 ºC and ~7 wt% H_2 at 140 ºC within 120~170 min. Recently, Ouyang et al. [157] investigated the catalytic activity of $ScCl_3$ upon the dehydrogenation performance of $LiAlH_4$ and revealed the catalytic mechanism of $ScCl_3$-doped $LiAlH_4$. The results showed that the onset hydrogen evolution temperature of the composite doped with 5 mol% $ScCl_3$ was decreased to 90 ºC, much lower than undoped $LiAlH_4$, as shown in **Fig. 28**. Moreover, the doped system could desorb ~3.6 wt% of H_2 in 180 min at 150 °C, which was twice as much as the desorbed H_2 from as-milled $LiAlH_4$ under same conditions (**Fig. 29**). The catalytic effect of the $ScCl_3$-doped system lies in the intermediate ScH_2 formed during the ball milling process, which promotes the hydrogen release of $LiAlH_4$. However, the hydrogen uptake capacity of the dehydrogenated sample was merely 0.22 wt% of H_2 in 6 h under the given

conditions, and thus further works on exploring the poor reversibility of the $ScCl_3$-doped system are still in demand.

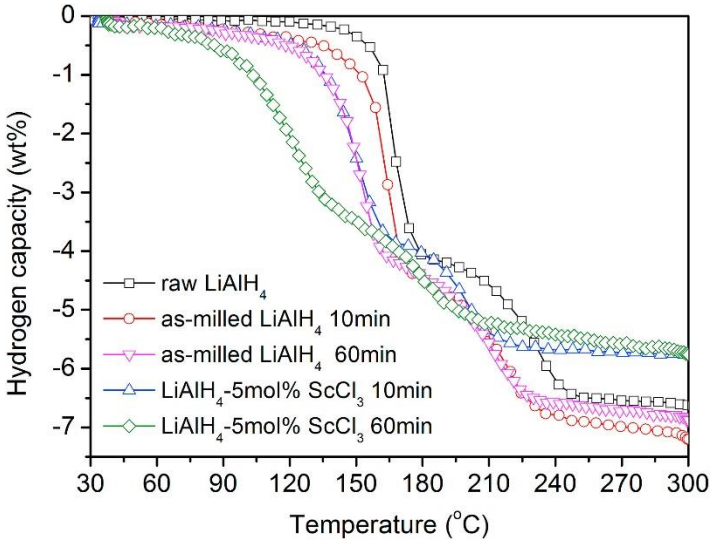

Fig. 28. Temperature Programmed Desorption (TPD) curves of raw $LiAlH_4$, as-milled $LiAlH_4$ 10 min, as-milled $LiAlH_4$ 60 min, $LiAlH_4$-5 mol% $ScCl_3$ 10 min, $LiAlH_4$-5 mol% $ScCl_3$ 60 min. Reprinted with permission from ref [157]. Copyright 2018 Elsevier.

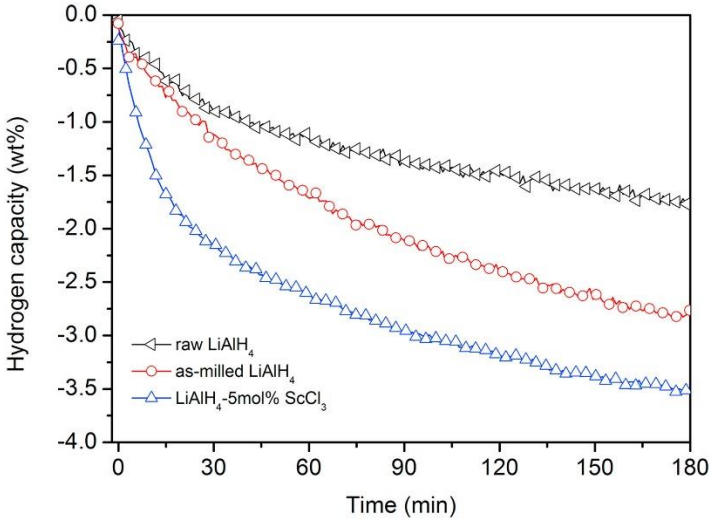

Fig. 29. Hydrogen desorption curves at 150 °C: (a) raw $LiAlH_4$, (b) as-milled $LiAlH_4$ and (c) $LiAlH_4$-5 mol% $ScCl_3$. Reprinted with permission from ref [157]. Copyright 2018 Elsevier.

In contrast to the alkali metals alanates, former studies [158, 159] of $Mg(AlH_4)_2$ showed that, the dehydrogenation of the hydride proceeded without the involvement of $[AlH_6]_3^-$ as an intermediate phase, as the Eq. 4-5 listed below:

$$Mg(AlH_4)_2 \rightarrow MgH_2 + 2Al + 3H_2 \quad (4)$$

$$3MgH_2 + 4Al \rightarrow Mg_2Al_3 + Mg\text{-}Al + 3H_2 \quad (5)$$

DSC analysis [160] demonstrated that there is a minor endothermic peak located at 147 °C (**Fig. 30**), corresponding to the first-step decomposition of $Mg(AlH_4)_2$ into MgH_2 and Al metal. And the enthalpy calculated from the peak area is ~2 kJ/mol, indicating that $Mg(AlH_4)_2$ may be unsuitable as reversible hydrogen material for potential vehicular applications. Fichtner et al. [129] investigated the kinetic behaviors of $Mg(AlH_4)_2$ by doping with 2 mol% $TiCl_3$ and they found that the peak decomposition temperature for the $TiCl_3$-doped system could be reduced by up to 45 °C. However, full dehydrogenation to MgH_2 still requires heating to ~200 °C.

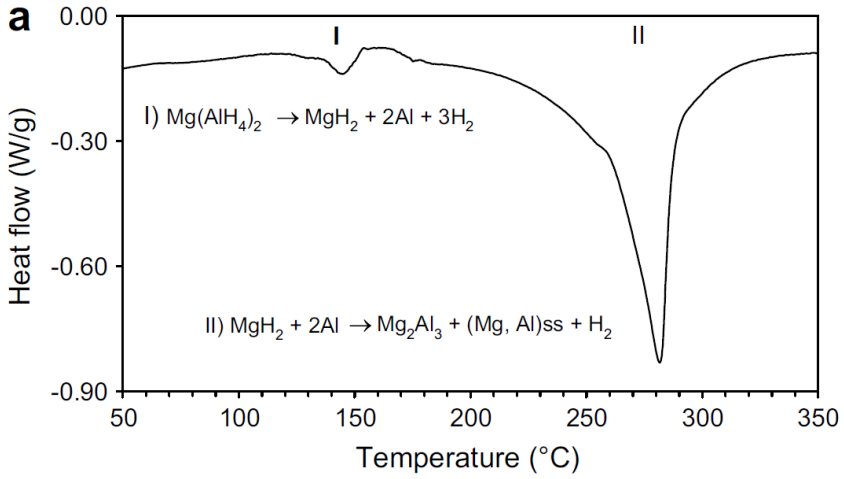

Fig. 30. DSC curve of $Mg(AlH_4)_2$ at a heating rate of 2 °C/min. Reprinted with permission from ref [160]. Copyright 2003 Elsevier.

(2) Nanostructuring

Nanoscaling is also an effective approach to tailor the hydrogen storage performance of alanates. Several nanoscaling techniques developed to date include ball milling, vapour deposition, and nanoconfinement. Andreasen et al. [161] studied the influence of the ball milling process on crystallite size and desorption kinetics of $LiAlH_4$. As seen in **Fig. 31**, the first-step dehydrogenation rate is negatively correlated with the rising the crystallite size. Latter studies also confirmed that ball milling could enhance the hydrogen desorption kinetics of $LiAlH_4$. Analogously, Xiao et al. [162] successfully synthesized nanocrystalline $NaAlH_4$ by ball milling the NaH/Al and 4 mol% TiF_3 hybrids at H-pressure of 1.5~2.5 MPa within 50 h. The as-received $NaAlH_4$ displayed a highly reversible H-capacity over 4.7 wt % H_2 with rapid reaction kinetics, and it could absorb ~3.5 wt% of H_2 even at ambient temperature. The de-/rehydriding curves of the as-received $NaAlH_4$ at various temperatures are shown in **Fig. 32**, of which the hydrogen uptake capacity ranges from 2.0 wt% at 40 °C to 4.8 wt% H_2 at 120 °C within 60 min. With regard to the dehydriding process, the hydrogen release capacity increases from 2.5 wt% to 4.7 wt% H_2 as the temperature varies from 100 to 125 °C in 120 min.

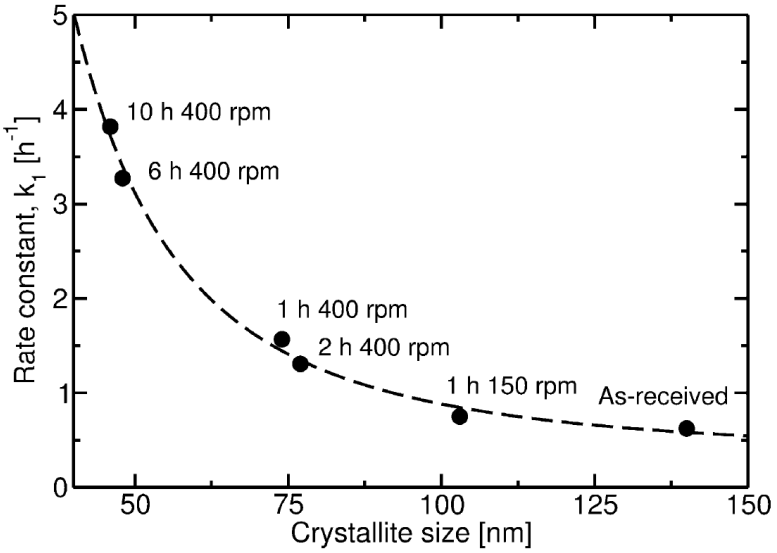

Fig. 31. Rate constants for first-step dehydrogenation reaction as a function of crystallite size. Reprinted with

permission from ref [161]. Copyright 2005 Elsevier.

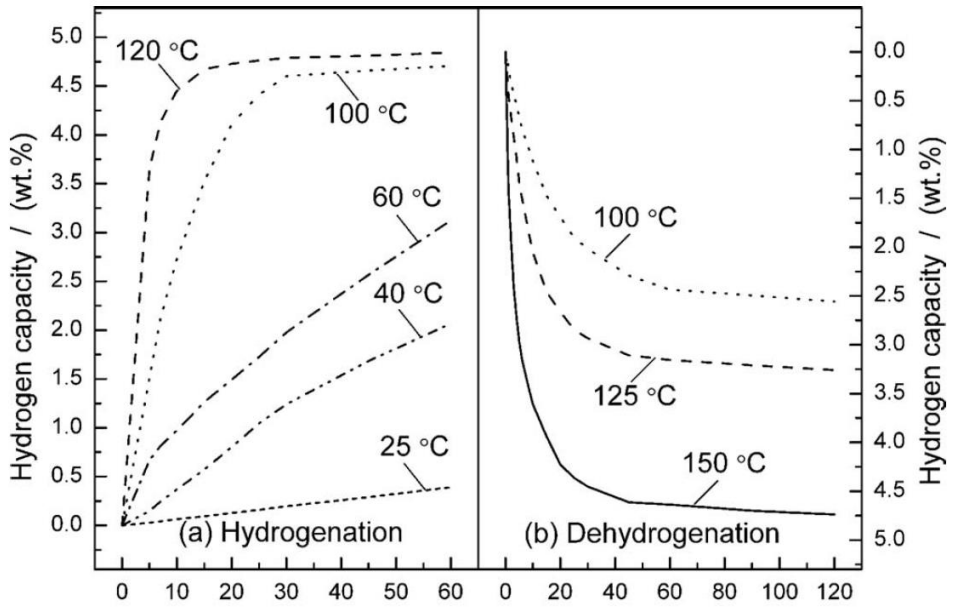

Fig. 32. Hydriding/dehydriding curves of NaH/Al+4 mol% TiF_3 ball milled for 50 h and 2.5 MPa H-pressure at different temperature. Reprinted with permission from ref [162]. Copyright 2009 Elsevier.

To solve the troublesome issue upon the maintenance of nanoscale size of alanates obtained from the ball milling method, researchers and scientists proposed space-confinement accordingly. The nanoscaffold materials, including carbon-based materials [163], ordered mesoporous silica [164] and metal-organic materials [165], have been developed to support alanates up to now. A typical space-confined procedure [164] is illustrated in **Fig. 33**, where $NaAlH_4$ is loaded into ordered mesoporous silica (OMS) with a pore size of 10 nm through THF solvent-mediated infiltration. The space-confined system showed a lower dehydrogenation temperature and faster kinetics than that of $NaAlH_4$. Moreover, the rehydriding of the dehydrogenated $NaAlH_4$ composite could be achieved at 125~150 °C under 3.5~5.5 MPa of hydrogen pressure. Stephens et al. [166] successfully incorporated $NaAlH_4$ into carbon aerogel with pore size up to 13 nm by melt infusion under ~18 MPa H_2 overpressure at 189 °C. The dehydrogenation temperature was reduced to ~140 °C from above 230 °C in the bulk catalyst-free alanate

and a facile rehydrogenation process with ~85% of the initial capacity was achieved at ~160 °C under 10 MPa H_2. De Jong's group [163] prepared nanosized $NaAlH_4$ particles supported on a surface-oxidized carbon nanofiber support (CNFox), of which the initial desorption temperature of the $NaAlH_4$/CNFox was downshifted to 40 °C, much lower than that of the physical mixture (150 °C) under the same conditions. Afterwards, Jensen et al. [167] proposed that $TiCl_3$-doped $NaAlH_4$ constrained in nanoporous carbon aerogel could facilitate far more rapid dehydrogenation, compared to both confined $TiCl_3$-free $NaAlH_4$ and bulk milled samples of $NaAlH_4$/$TiCl_3$. Its onset dehydrogenation temperature was as low as 33 °C and the hydrogen release rate reached a maximum at 125 °C, indicating favorable synergetic effect between space-confinement and catalyst addition. Moreover, $NaAlH_4$ in the $TiCl_3$-modified scaffold desorbed 2.9 wt% of H_2 in the first dehydrogenation and 1.6 wt% H_2 for the fourth cycle. Recently, Sun and co-workers [168] put forward a nanoconfinement system, of which $NaAlH_4$ was exclusively embedded in ordered mesoporous carbon (MC) with a pore size of 4 nm. The confined $NaAlH_4$ exhibited faster dehydrogenation kinetics than that of pure $NaAlH_4$ with a reduction by ~70 kJ/mol H_2 for Ea. Specifically, the nanoconfinement system could release 5.0 wt.% of H_2 at 180 °C in > 40 min, whereas the hydrogen release content of the pristine material was 0.5 wt.% H_2 even over 90 min under the same conditions. The cycling properties for the space-confined $NaAlH_4$ were also improved remarkably relative to the pristine material. During cycling, the confined system released 5 wt% H_2 for the first cycle, which was marginally downshifted to 4.6 wt% in the later five cycles, and remained at ~4.2 wt% H_2 through subsequent cycles (**Fig. 34**). This slight reduction for capacity may be the loss of active byproducts, because of the oxidation or migration at the openings of pores. By comparison, the hydrogen desorption capacity of the pristine $NaAlH_4$ was merely 0.5 wt% in the first cycle and decreased to < 0.2 wt% of H_2 after five cycles for the equivalent conditions.

Nanoconfinement can also enhance the hydrogen storage properties of $LiAlH_4$ and $Mg(AlH_4)_2$. Recently, Wang et al. [169] demonstrated a reversible space-confined $LiAlH_4$ hydrogen storage system, of which $LiAlH_4$ with particle size varying from 3 to 15 nm was incorporated into the porosity of graphite with a high surface area. The onset hydrogen desorption temperature of the space-confined $LiAlH_4$ was near 100 °C and the composite could be rehydrogenated at 300 °C and 7 MPa H_2 pressure. The result indicated that the nanoconfined $LiAlH_4$ demonstrated direct hydrogen reversibility through the Li_3AlH_6 route. Pan's group [170] first proposed a mechanical-force-driven physical vapor deposition procedure for preparing the support-free $Mg(AlH_4)_2$ nanorods with diameters of 20-40 nm (**Fig. 35**). As shown in **Fig. 36**, the hydrogen storage performance of the support-free $Mg(AlH_4)_2$ was more superior to those of the bulk counterparts, of which the total hydrogen capacity maintained 9.0 wt% and the dehydrogenation temperatures were lowered markedly with the reduction of the onset and end temperatures by ~30 °C and ~80 °C, respectively. The dehydrogenated $Mg(AlH_4)_2$ nanorods absorbed hydrogen from 120 °C, much lower than that (~150 °C) of the microrods. Notably, the morphology of the $Mg(AlH_4)_2$ nanorod persisted throughout the dehydrogenation and hydrogenation processes, suggesting a great potential for reversible storage.

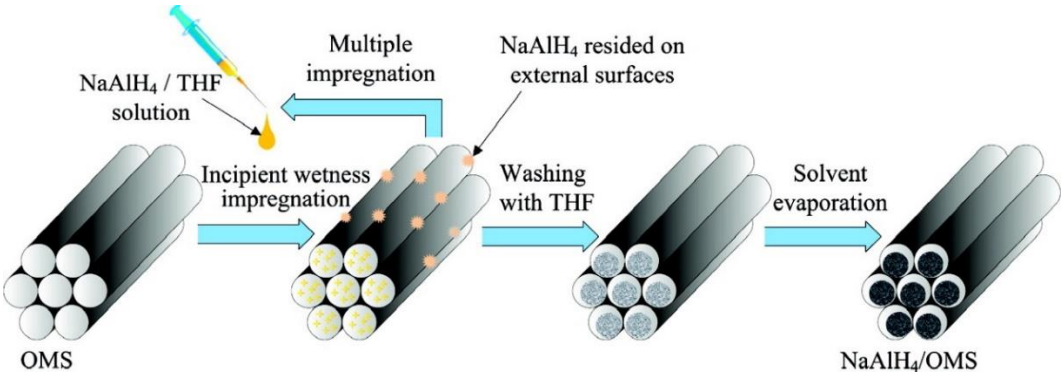

Fig. 33. Preparation process for $NaAlH_4$ nanoparticles space-confined in OMS. Reprinted with permission from ref [164]. Copyright 2008 ACS Publications.

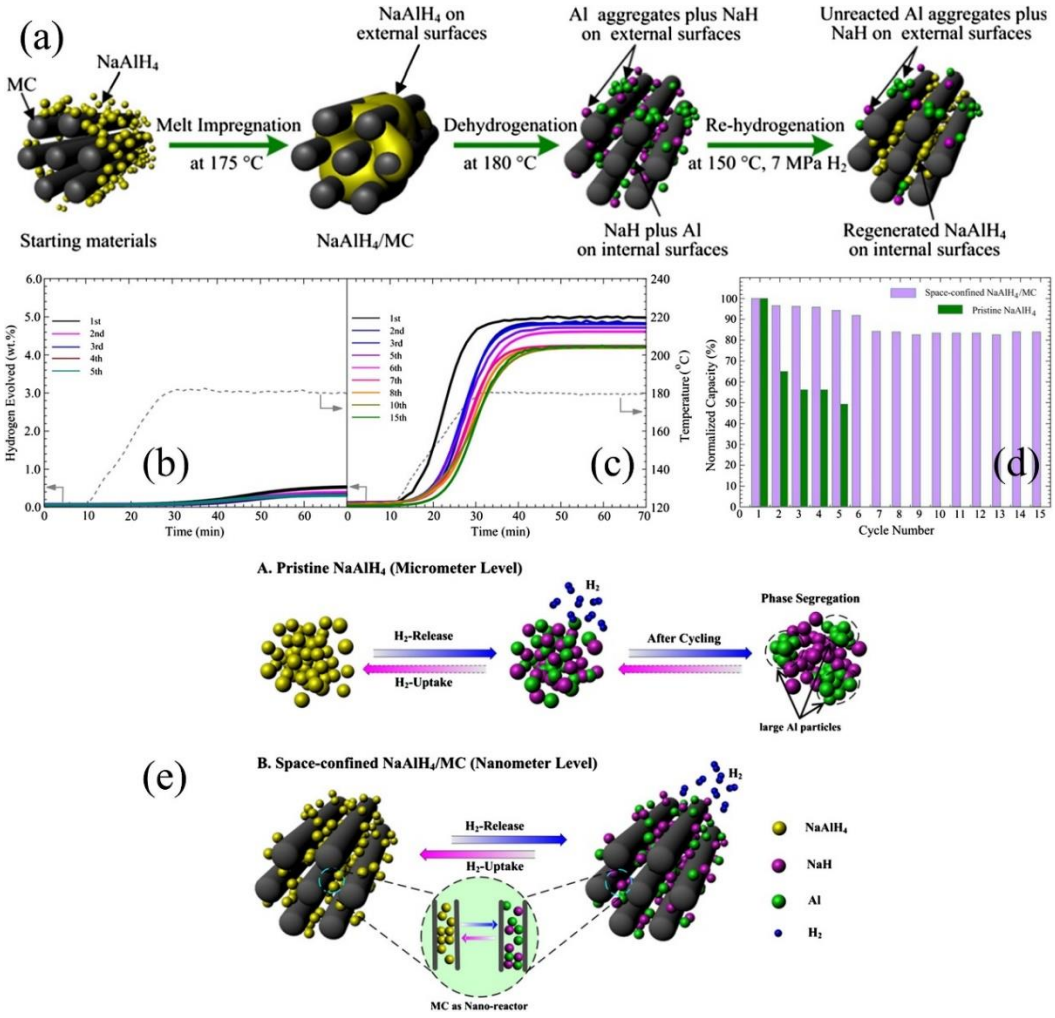

Fig. 34. (a) Schematic illustration of the preparation process for the $NaAlH_4$ exclusively confined in MC. Evolution of the dehydrogenation curves for (b) pristine $NaAlH_4$ after five cycles and (c) the confined $NaAlH_4$/MC after 15 cycles. The hydrogen capacity as a function of cycle number is shown in (d), where the hydrogen capacities are normalized to unity for the first value. (e) Schematic illustration of the phase distribution in pristine $NaAlH_4$ and the confined $NaAlH_4$/MC upon multiple cycling. Reprinted with permission from ref [168]. Copyright 2011 Elsevier.

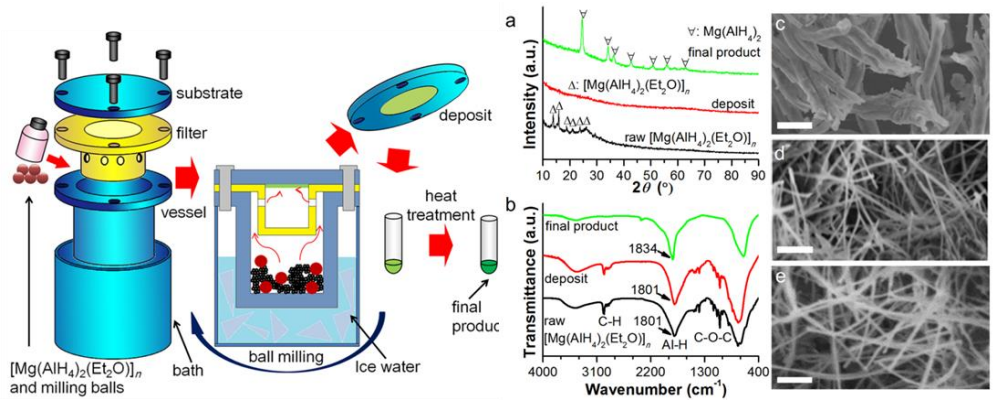

Fig. 35. A schematic diagram of the $Mg(AlH_4)_2$ nanorod preparation process (left) and the characterizations of the $Mg(AlH_4)_2$ samples at different stages (right). Reprinted with permission from ref [170]. Copyright 2014 Nature Publishing Group.

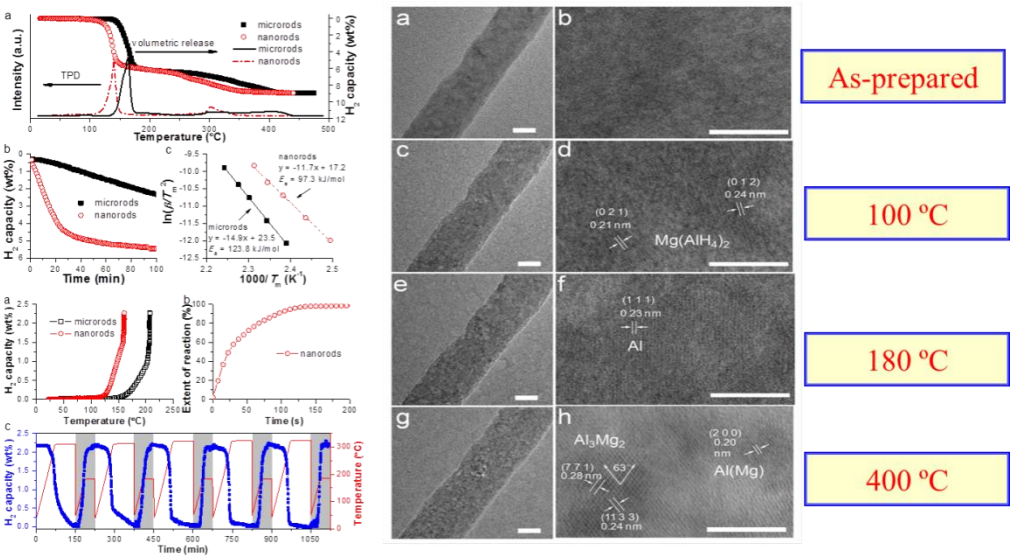

Fig. 36. Hydrogen desorption/absorption and cycling performances of $Mg(AlH_4)_2$ microrods and nanorods (left) and in-situ TEM images of $[Mg(AlH_4)_2 \cdot (Et_2O)]_n$ nanorod at different stages (right). Reprinted with permission from ref [170]. Copyright 2014 Nature Publishing Group.

(3) Composite systems

Multi-phase and multi-scale integrations have been developed for optimizing the comprehensive properties of alanates. For example, Vittetoe's group [171] studied the hydrogen evolution behaviors for the composite of $LiAlH_4$ and nano-MgH_2 obtained via mechano-chemical milling at

ambient temperature. They found that the nanosized MgH_2 had superior hydrogen performance on the parts of onset desorption temperature, hydrogen release amount and kinetics over the commercial one. For the 2 h-milled mixture, the initial hydrogen release temperature was decreased to 90 °C with a H-capacity of ~5.2 wt% (200 °C). The life-cycle tests revealed that the destabilized composite possessed ~5 wt% reversible capacity at a temperature below 350 °C, though the ΔH for dehydrogenation was estimated to be 85 kJ/mol H_2. Ismail et al. [172] reported the enhanced hydrogen storage behaviors of $LiAlH_4$-MgH_2 composites doped with Fe_2O_3 nano-powder. The results indicated that the addition of 5 wt% Fe_2O_3 into the composite could decrease the initial desorption temperature to 95 °C, ~40 °C lower than the undoped one. Moreover, the Ea for the dehydrogenation was lowered from 125.6 to 117.1 kJ/mol H_2 for the Fe_2O_3-doped system. They believed that the intermediate $Li_2Fe_3O_4$ worked as an actual catalyst in the MgH_2-$LiAlH_4$-Fe_2O_3 composite, which was favorable for the interaction of MgH_2 and $LiAlH_4$.

A similar effect occurs in the $NaAlH_4$-MgH_2 system. Yu's group [173] prepared 4MgH_2-$NaAlH_4$ composite by mechanically ball milling, of which the onset desorption temperature was downshifted by ~50 °C (as shown in **Fig. 37**) with the Ea for the MgH_2-relevant decomposition being decreased to 148 kJ/mol (20 kJ/mol less than that for as-milled MgH_2). Nevertheless, both of the absorption kinetics and hydrogen capacity of MgH_2-$NaAlH_4$ were inferior to MgH_2 (**Fig. 38**). Subsequently, they [174] introduced TiF_3 to further improve the dehydrogenation properties of the MgH_2-$NaAlH_4$ composite system. The results indicated that the system doped with 10 wt% TiF_3 exhibited lower dehydrogenation temperature and remarkably reduced Ea for each step dehydrogenation process compared to the undoped one. It was believed that the in-situ formed Ti-Al phase during the ball milling process acted as a true catalyst in the TiF_3-doped composite. Recently, Cheng et al. [175]

introduced TiH_2 to the above composite by ball milling method, resulting in the onset hydrogen release temperature of ~100 °C (which is lower by 50 °C than that of $4MgH_2$-$NaAlH_4$ composite) with much lower Ea (68 kJ/mol H_2) than the undoped system (159 kJ/mol H_2). Significantly, the Ea for rehydrogenation in the TiH_2-doped system was markedly reduced from 161.6 kJ/mol H_2 of $4MgH_2$-$NaAlH_4$ to 125.8 kJ/mol H_2. The enhanced kinetics may be the formation of intermediate phase Al_3Ti, facilitating the recombination of MgH_2 during the hydrogen absorption process. Wang at el. [176] systematically investigated the synergetic effect of $NaAlH_4$ and TiF_3 upon dehydriding performance of $Mg(AlH_4)_2$. The initial temperature for hydrogen release for the co-doped composite was reduced to 74 °C, ~59 °C lower than that of pristine $Mg(AlH_4)_2$. On the other hand, the desorption kinetics of the co-doped system was also enhanced, releasing ~94% of the total amount hydrogen in 48 min with the Ea being 85.6 kJ/mol H_2.

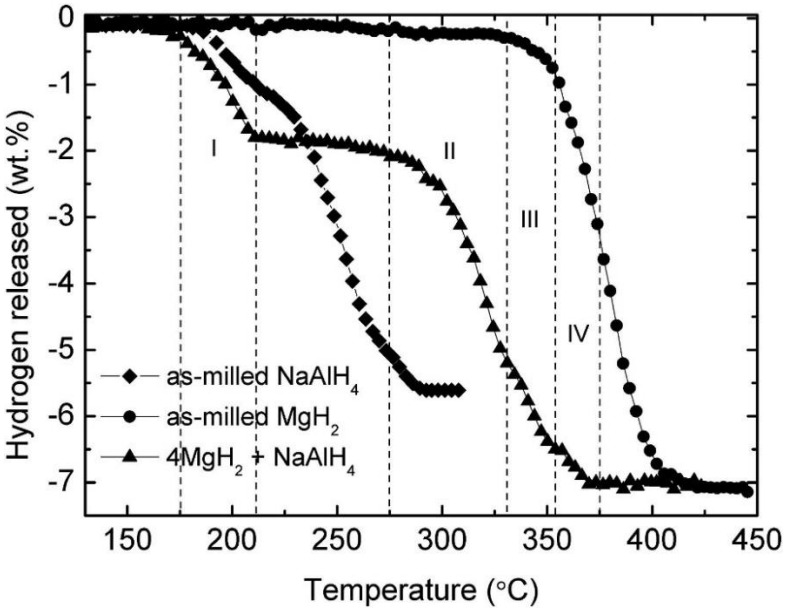

Fig. 37. TPD curves of the as-milled MgH_2, the as-milled $NaAlH_4$, and the MgH_2-$NaAlH_4$ composite. Reprinted with permission from ref [173]. Copyright 2011 Elsevier.

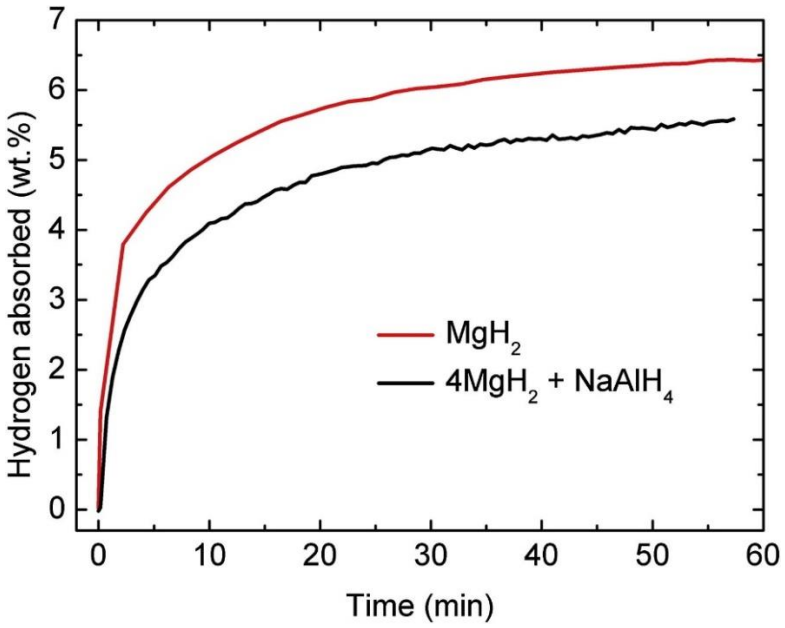

Fig. 38. Isothermal rehydrogenation kinetics of the MgH_2–$NaAlH_4$ composite and the MgH_2 samples at 300 °C and under 3 MPa H_2. Reprinted with permission from ref [173]. Copyright 2011 Elsevier.

3.2.2. $LiBH_4$/$NaBH_4$/$Mg(BH_4)_2$ hydrogen storage systems

In comparison with alanates, light-metal borohydrides possess higher theoretical hydrogen content (> 10 wt% H_2, see in **Table 5**), such as $LiBH_4$, $Mg(BH_4)_2$, and $NaBH_4$, etc. The light-weight metal borohydrides are recognized as one of the most promising solid hydrogen materials for their unparalleled hydrogen densities [177, 178], much higher than the ultimate target of 6.5 wt% by DOE. The crystal structures of the exemplary borohydrides are shown in **Fig. 39**, where the low- and high-temperature phases of $LiBH_4$ are determined to be orthorhombic and hexagonal structures and the structure of $NaBH_4$ is cubic as well as a crystal structure of hexagonal $Mg(BH_4)_2$. The overall decomposition reaction of alkali metal borohydrides is ascribed as [31]:

$$MBH_4 \rightarrow MH + B + 3/2H_2 \quad (6)$$

$$\text{or} \quad MBH_4 \rightarrow M + B + 2H_2 \quad (7)$$

The thermal decompositions of alkaline earth borohydrides proceed as the follows [179-181]:

$$M(BH_4)_2 \rightarrow MH_2 + 2B + 3H_2 \quad (8)$$

$$\text{or} \quad M(BH_4)_2 \rightarrow MB_2 + 4H_2 \quad (9)$$

$$\text{or} \quad M(BH_4)_2 \rightarrow 2/3MH_2 + 1/3MB_6 + 10/3H_2 \quad (10)$$

Some theoretical calculations and thermal desorption experiments demonstrated that the decomposition temperature of the single metal borohydrides was empirically well-related to the Pauling electronegativity of the metal cations. The charge transfer between M^{n+} and $[BH_4]^-$ is a critical factor for the stability of $M(BH_4)n$, where the decomposition temperature of $M(BH_4)n$ is negatively correlated with the Pauling electronegativity χP of M. Note that the Pauling electronegativity of Na and K is lower than that of Li, rendering $NaBH_4$ and KBH_4 unsuitable as reversible hydrogen storage materials for potential on-board applications. For example, $NaBH_4$ and KBH_4 deliver dehydrogenation temperatures over 500 °C [31]. On contrary, the hydrolysis of $NaBH_4$ possesses numerous appealing features, such as high gravimetric hydrogen storage capacity (up to 10.8 wt%), precisely controllable hydrogen release, high hydrogen purity, and environmentally benign by-products. More importantly, the regeneration of $NaBH_4$ can be readily achieved from its hydrolysis product ($NaBO_2 \cdot xH_2O$) in the presence of reductants, enabling a wide utilization of $NaBH_4$ for hydrogen storage. With regard to $Mg(BH_4)_2$, the decomposition products could hardly be rehydrogenated back to $Mg(BH_4)_2$, apart from some extreme conditions (400 °C and 95 MPa H_2 pressure) [182]. Few studies are focused on $Al(BH_4)_3$ because of its spontaneous hydrogen release below room temperature [183, 184]. Of late, researchers and scientists are primarily devoted to investigating the hydrogen absorption and desorption behaviors of $LiBH_4$. $LiBH_4$ undergoes three-stage for hydrogen release with ~13.8 wt% of H_2 desorption at a low heating

ramping rate of 0.5 °C/min with LiH and B as dehydrogenation products [185], as shown in **Fig. 40**. Orimo et al. [186] confirmed the existence of the intermediate phase $Li_2B_{12}H_{12}$ during the hydrogen release process and they also observed other impurity gases (such as B_2H_6) released in dehydrogenation. **Fig. 41** shows the schematic enthalpy diagram of the hydrogen evolution reaction for $LiBH_4$, including the intermediates and thermal decomposition products. The most stable state is $LiBH_4$ with the low-temperature phase Pnma and it would convert into the high-temperature modification ($P6_3mc$) at the temperature of ~118 °C, followed by melting around 280 °C. Subsequently, hydrogen desorption starts and undergoes the above-discussed intermediate phase(s), resulting in LiH and solid boron as final products. Due to the high stability of LiH (ΔH_f = -181.4 kJ/mol) of H_2)), its dehydrogenation proceeds at temperatures above 727 °C, thereby making it usually not practical in technical applications. Generally, the main dehydrogenation temperature of pristine $LiBH_4$ is ~400 °C under ambient pressure and the rehydrogenation conditions of LiH and B mixtures are extraordinarily harsh (at 600 °C and under 35MPa H_2 pressure), caused by chemical inertness of boron [124]. In this review, we mainly summarized the recent progress upon $LiBH_4$, particularly emphasizing on the thermodynamic and kinetic tailoring strategies via nanostructuring, catalysis, cation/anion substitution, and reaction destabilized systems.

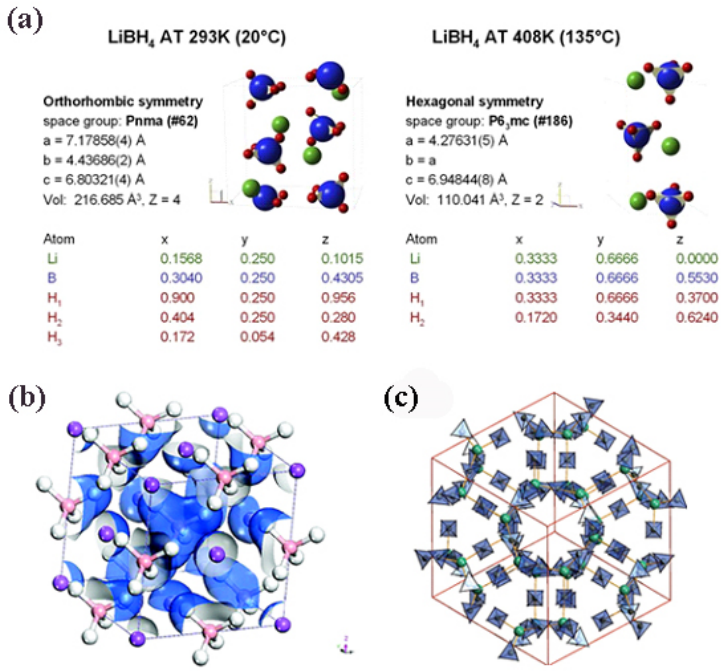

Fig. 39. (a) Low- and high-temperature structures of $LiBH_4$ determined from XRD. Blue, green, and red spheres represent boron, lithium, and hydrogen, respectively. Reprinted with permission from ref [185]. Copyright 2007 Elsevier. Crystal structure of cubic (b) α-$NaBH_4$. Reprinted with permission from ref [187]. Copyright 2010 ACS Publications, (c) γ-$Mg(BH_4)_2$. Reprinted with permission from ref [188]. Copyright 2011 Wiley Online Library.

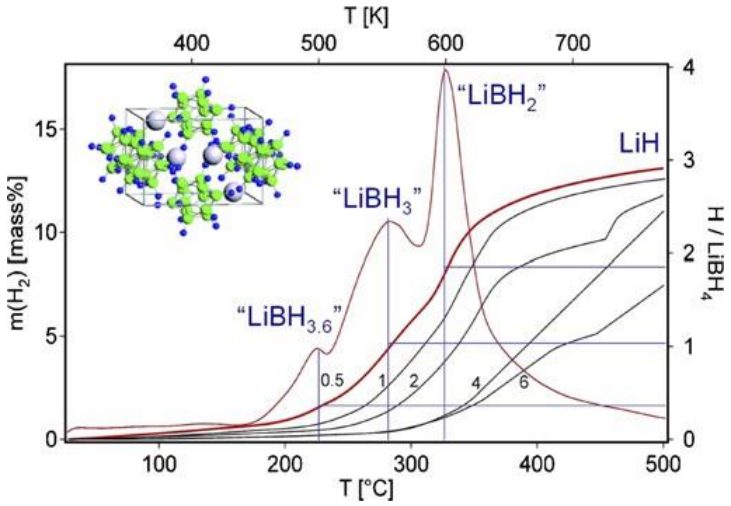

Fig. 40. Integrated thermal desorption from $LiBH_4$ measured at various heating rates. The structure for an intermediate phase of $Li_2B_{12}H_{12}$ is shown as the inset. Reprinted with permission from ref [185]. Copyright 2007 Elsevier. Inset reprinted with permission from ref [186]. Copyright 2006 American Institute of Physics.

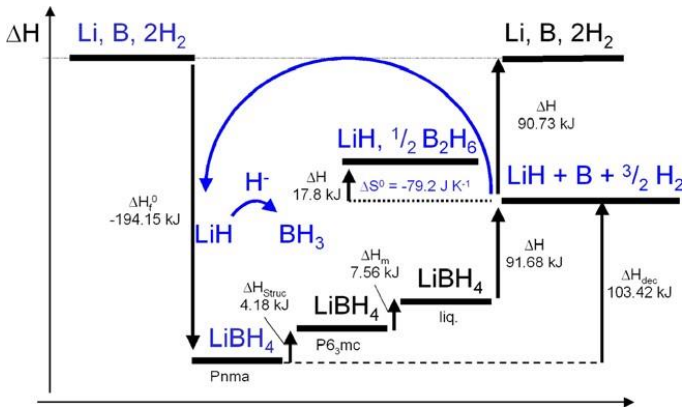

Fig. 41. Schematic enthalpy diagram of intermediate and final decomposed products of $LiBH_4$. Reprinted with permission from ref [185]. Copyright 2007 Elsevier.

(1) Cation/anion substitution

Orimo et al. [189, 190] systematically investigated the thermodynamics of borohydrides with a single cation through first-principles calculations and thermal desorption experiments. They found that the decomposition temperature of the single metal borohydrides is empirically related fairly well with the Pauling electronegativity of the metal cations. Accordingly, the first-principles calculations indicated that charge transfer between Mn^+ and $[BH_4]^-$ is a linchpin factor for the stability of $M(BH_4)_n$, where the decomposition temperature of $M(BH_4)_n$ is negatively correlated with the Pauling electronegativity χ_P of M [191], as shown in **Fig. 42**. Therefore, it may be possible to tailor the thermodynamic stability of $LiBH_4$ via introducing more electronegative elements to reduce the charge transfer from Li^+ to $[BH_4]^-$, thereby weakening the ionic bond between Li^+ and $[BH_4]^-$. Orimo's group [192] proposed the partial substitution of Li with Cu, because of almost the same ionic radii of Cu^+ and Li^+ as well as the larger electronegativity of Cu. Assuming the same crystal structure as orthorhombic $LiBH_4$, the calculations on $(Li_{1-x}Cu_x)BH_4$ were performed for x = 0.25, 0.5, 0.75, and 1. It was confirmed that the heat of formation is increased by ramping content

x of Cu. The optimum x was predicted to be $x \approx 0.3$ for practical applications. Subsequently, several typical multi-cation borohydrides have been synthesized, such as $LiZr(BH_4)_5$, $Li_2Zr(BH_4)_6$, $LiZn_2(BH_4)_5$, $LiK(BH_4)_2$, $Li_4Al_3(BH_4)_{13}$, $LiMn(BH_4)_3$, $LiSc(BH_4)_4$, etc [193-199]. The novel borohydrides mostly exhibits moderate thermodynamics between $LiBH_4$ and $M(BH_4)_n$. Normally, two main strategies are applied to synthesize $MLi(BH_4)_m$. One is mechanically ball milling the mixture of $LiBH_4$ and $M(BH_4)_n$, and another is the mechanochemical synthesis scenario based on the following reaction [200]:

$$MCl_n + mLiBH_4 \rightarrow MLi_{m-n}(BH_4)_m + nLiCl \quad (11)$$

Recently, Lindemann et al. [201] synthesized $Al_3Li_4(BH_4)_{13}$ (**Fig. 43** shows a cubic unit cell structure) via high-energy ball milling $AlCl_3$ and $LiBH_4$ mixtures. The onset dehydrogenation temperature of the Al-Li-borohydride was as low as ~70 °C, accompanied by the formation of $LiBH_4$ in the meantime. Unfortunately, the release of diborane (B_2H_6) and the Al evaporation restricted the reversibility of $Al_3Li_4(BH_4)_{13}$. This bottleneck might be broken by the formation of a boride.

Apart from cation substitution, partial substitution for $[BH_4]^-$ ligand or H^- in the complex anion can also lower the thermodynamic stability of $LiBH_4$. For instance, a density functional theory study indicated that $LiBH_{4-x}F_x$ with an orthorhombic structure may be obtained by partially replacing H^- in $LiBH_4$ with F^-. As the substitution mass of F^- reaches 7% (i.e., $LiBH_{3.75}F_{0.25}$), the computational decomposition enthalpy is reduced from 60.9 to 36.6 kJ/mol H_2. This gives an expected dehydrogenation equilibrium pressure of 1 bar H_2 at ~100 °C with a theoretical H-capacity over 11.3 wt% H_2 [202]. Fang et al. [203] put forward a reversible dehydrogenation system of $LiBH_4$ doped with titanium halides ($TiCl_3$ or TiF_3) combining the synergetic effect of catalysis and anion

substitution. In particular, TiF_3 exhibited a more superior promoting effect than $TiCl_3$, on the reversible dehydrogenation of $LiBH_4$. The results revealed that the catalytic effect may be attributed to in-situ formed Ti hydride in the milling or heating process. On the other hand, the F anion could readily substitute H^- located in both $LiBH_4$ and LiH lattices (**Fig. 44**), delivering a favorable thermodynamic modification, where ΔH for the dehydrogenation of $LiBH_4$-0.04TiF_3 composite was decreased to 45 kJ/mol from 54 kJ/mol H_2 for neat $LiBH_4$. This result may provide a new conceptual basis for designing novel hydrogen storage materials with the united effect of functional cation and anion.

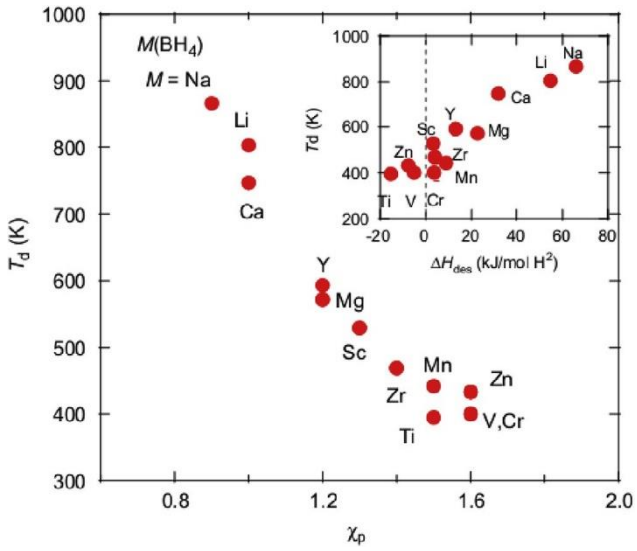

Fig. 42. Dehydrogenation temperature (T_d) as a function of the Pauling electronegativity χ_p. The inset shows the correlation between T_d and estimated ΔH_{des} for the desorption reaction. Reprinted with permission from ref [191] Copyright 2008 Elsevier.

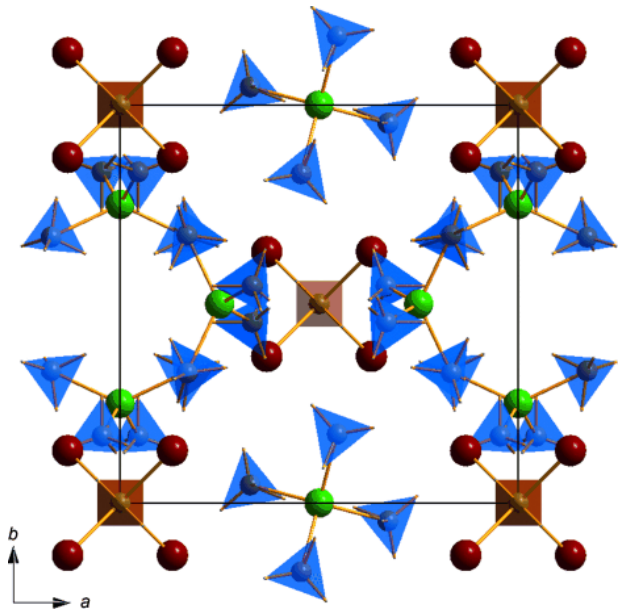

Fig. 43. Unit cell of $Al_3Li_4(BH_4)_{13}$. Four $[BH_4]^-$ tetrahedra (blue) and one Al^{3+} cation (green) form the complex anion $[Al(BH_4)_4]^-$. Four Li^+ cations (red) bonded to one $[BH_4]^-$ tetrahedron (brown) in the centre form the complex cation $[Li_4(BH_4)]^{3+}$. Reprinted with permission from ref [201]. Copyright 2010 Wiley Online Library.

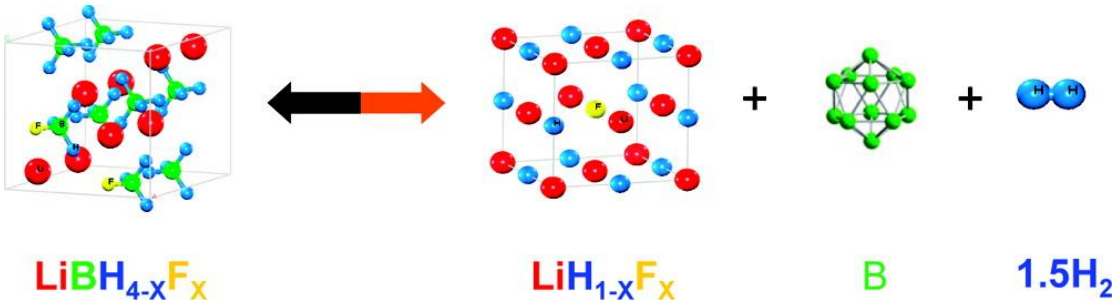

Fig. 44. Reversible dehydrogenation in the F-substituted $LiBH_4$ system. Reprinted with permission from ref [203].

Copyright 2011 ACS Publications.

(2) Catalyst modification

The catalyst doping is an effective strategy to lower the Ea for multiple-step reactions, enabling fast de-/rehydrogenation kinetics of $LiBH_4$. The catalysts can be summarized into three groups: metals and compounds, metal oxides and metal halides, and carbon-based materials (carbon nanotubes, activated carbons or graphene).

For metal and compound dopants, taking Al catalyzed $LiBH_4$ for instance, over 7.2 wt% of H_2 is liberated in ~3 h at 450 °C, but the rehydrogenation H-capacity is reduced to 3 wt% after 4 cycles at 400 °C under 100 bar H_2 [204]. Yu et al. [205] found that the hydrogen desorption kinetics of Ni-doped $LiBH_4$ was enhanced remarkably. The desorption plateau pressure of the composite was 0.023 MPa, 0.057 MPa and 0.103 MPa, respectively, at 320 °C, 350 °C, and 400 °C, whereas no plateau is observed for pristine $LiBH_4$ even at ~404 °C. In addition, the dehydrogenated products could be converted partly into $LiBH_4$ at 600 °C under 10 MPa H-pressure. Puszkiel et al. [206] synthesized $Mg_{50}Ni$-$LiBH_4$ composite by ball milling under an argon atmosphere, which delivered a considerable hydrogen capacity of 7 wt% H_2 at 300 °C in only 5 min. Further analysis of the composite confirmed that a new irreversible Mg-B interaction, i.e., $MgNi_3B_2$ phase, was formed during hydrogen cycling, which might influence the kinetics of the respective composite. Recently, Zhu's group [207] synthesized CoB with different nanostructures via a chemical process and then doped with $LiBH_4$. It was found that CoB could facilitate the de/rehydrogenation of $LiBH_4$, and the catalytic activity of CoB depends heavily on its morphology, being approximately in the order of mulberry-like > waxberry-like > chain-like > flake-like > rod-like. The onset hydrogen release of $LiBH_4$ took place at 170 °C and the majority of H_2 release was ~ 350 °C with a maximum H-capacity of 10.4 wt% H_2. Significantly, almost full reversibility was achieved at 400 °C under 10 MPa H_2, remaining 9.6 wt% of H_2 even after four cycles. The de-/rehydrogenation curves of $LiBH_4$ catalyzed by mulberry-like CoB and the associated catalyzing mechanism are shown in **Fig. 45**. The excellent catalytic effect may be attributed to the uncompensated electronic structure of CoB resulted from the electron transfer from B to Co, making boron electron-deficient and cobalt electron enriched.

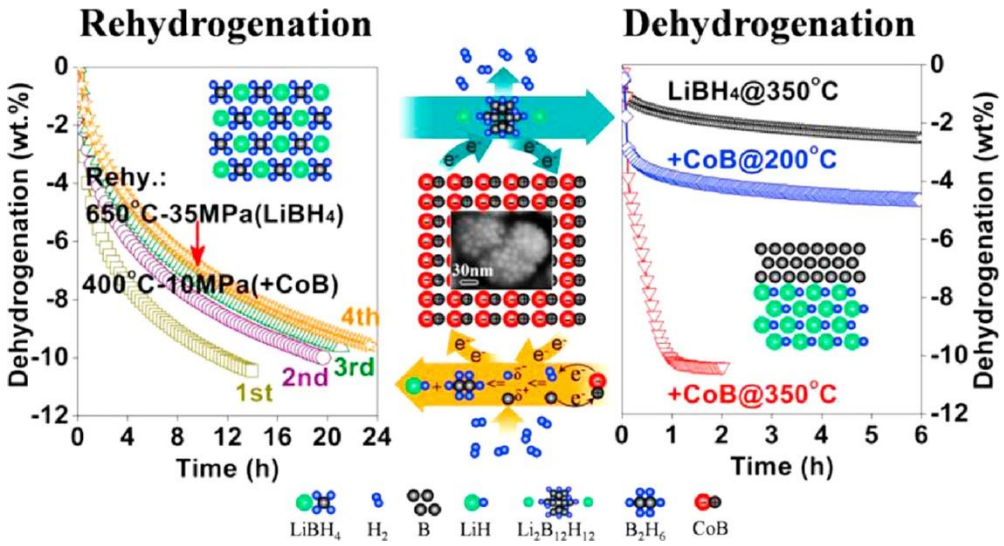

Fig. 45. The reversible dehydrogenation of $LiBH_4$ doped with the mulberry-like nanostructured CoB and schematic illustration of de-/rehydrogenation mechanism. Reprinted with permission from ref [207]. Copyright 2014 Elsevier.

Metal oxides (SiO_2, V_2O_5, ZrO_2, TiO_2, SnO_2, and Fe_2O_3, etc.) and halides ($TiCl_3$, TiF_3, and $ZnCl_2$, etc.), have been discovered to facilitate the dehydrogenation of $LiBH_4$. Zuttel et al. [178] found that the hydrogen evolution of $LiBH_4$ was successfully catalyzed with SiO_2 and the major hydrogen desorption started at approximately 200 °C as well as the hydrogen capacity of 9 wt% H_2 below 400 °C (**Fig. 46**). Yu et al. [208] investigated the hydrogen desorption of $LiBH_4$ doped with various oxides (V_2O_5, SiO_2, TiO_2 and so on) and they found that the $LiBH_4$/oxide mixtures possessed much lower dehydrogenated temperature. For example, the initial dehydrogenation temperature was reduced as low as 100 °C for $LiBH_4/Fe_2O_3$ mixtures (mass ratios of 1:2), and the majority of the hydrogen (~6 wt %) could be released after heating to 200 °C (**Fig. 47**). The order of destabilization effect of $LiBH_4$ for the oxides was $Fe_2O_3 > V_2O_5 > Nb_2O_5 > TiO_2 > SiO_2$, as shown in **Fig. 48**. Further results revealed that the enhanced desorption behaviors in $LiBH_4$/oxides were resulted from a redox reaction: $xLiBH_4 + M_yO_z \rightarrow Li_xM_yO_z + xB + 2xH_2$. Particularly, they systematically studied the effect of TiO_2 with different addition amount upon the dehydrogenation of $LiBH_4$ [209]. As the

weight ratio of $LiBH_4$-TiO_2 was 4:1, there were three main hydrogen evolutions observed at 325 °C, 405 °C, and 525 °C with the full hydrogen release capacity of 11.9 wt% (**Fig. 49**). For the $LiBH_4$-TiO_2 sample with a ratio of 1:1, of which the onset temperature decreased to 150 °C as well as three peak temperatures at 245 °C, 390 °C, and 465 °C with the total weight loss up to 9.0 wt% H_2. Only one dehydrogenation peak was observed for the $LiBH_4$-$4TiO_2$ sample at 245 °C as well as a shoulder at ~ 180 °C, as opposed to the other samples. These implied that the doping quantity of TiO_2 also played a significant role in destabilizing $LiBH_4$. Moreover, XRD and in-situ neutron diffraction revealed that the destabilization of $LiBH_4$ by the oxide was caused by the formation of lithium titanate. The oxide-modified borohydride (75% $LiBH_4$ + 25% TiO_2), reported by Au and co-workers [210], could release 9 wt% of H_2 when heated from 100 to 600 °C and absorb ~8 wt% H_2 at 600 °C under 7 MPa H-pressure. The pressure was much lower than that for pristine $LiBH_4$ (350 bar) at the same temperature. With respect to metal halides, several types, including $TiCl_3$, TiF_3, and ZnF_2, etc., could dramatically reduce the hydrogen desorption temperature of $LiBH_4$, whereas a number of other halides, such as MgF_2, $MgCl_2$, $CaCl_2$, $SrCl_2$, or $FeCl_3$, could scarcely influence the dehydriding temperature [211]. The hydrogen desorption of $LiBH_4$-$0.1TiF_3$ composite was ~3.5 wt% H_2 at 150 °C and ~8.5 wt% H_2 at 450 °C, respectively, with a rehydriding capacity up to 6 wt% H_2 at 500 °C and 7 MPa pressure. The initial H_2 release temperature of $LiBH_4$ + $0.5TiCl_3$, $LiBH_4$ + $0.5TiF_3$, and $LiBH_4$ + $0.5ZnCl_2$ was reduced to room temperature, but they suffered from irreversibility owing to the unrecoverable boron loss caused by diborane emission. Yu et al. [212] systematically studied the role of TiF_3 upon the de-/rehydriding behaviors of $LiBH_4$ and they found the $LiBH_4$-TiF_3 mixtures showed remarkably improved thermodynamics and kinetics for hydrogen release. The desorption temperature was decreased as low as ~100 °C and the $3LiBH_4$-TiF_3

composites could release 5 wt% H_2 below 250 °C and 6.4 wt% H_2 at < 500 °C. Meanwhile, the dehydrogenated by-products were partially rehydrogenated under 10 MPa H_2 at 350 °C. The results revealed that the unfavorable dehydrogenation conditions for $LiBH_4$-TiF_3 may be resulted from an exothermic reaction:

$$3LiBH_4 + TiF_3 \rightarrow 3LiF + TiB_2 + B + 6H_2 \qquad \Delta H = -157.1 \text{ kJ/mol} \qquad (12)$$

The above exothermic process appears to be thermodynamically unfeasible for rehydrogenation. Further investigations indicated that the poor reversibility may be attributed to the formation of another new borohydride.

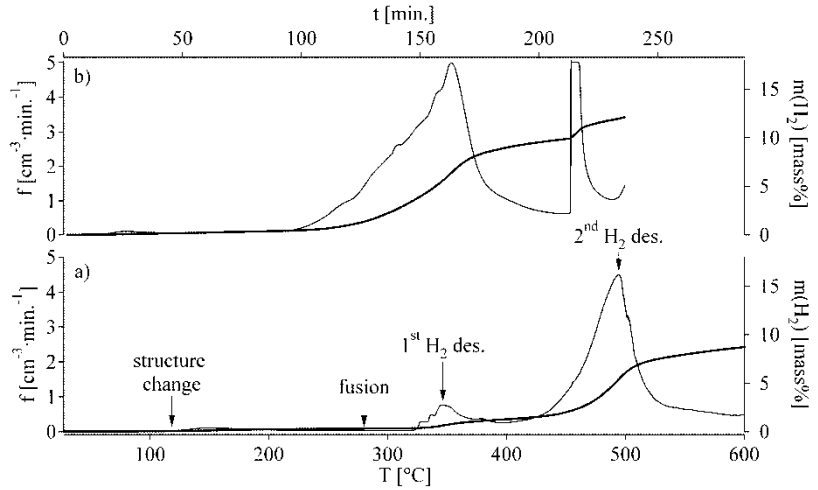

Fig. 46. Thermal desorption spectra of $LiBH_4$. The sample was heated after evacuation at room temperature with a heating rate of 2 K/min. The gas flow was measured as a function of time and the desorbed hydrogen was computed from the integrated gas flow: (a) pure $LiBH_4$ and (b) $LiBH_4$ mixed with SiO_2 as catalyst. Reprinted with permission from ref [178]. Copyright 2003 Elsevier.

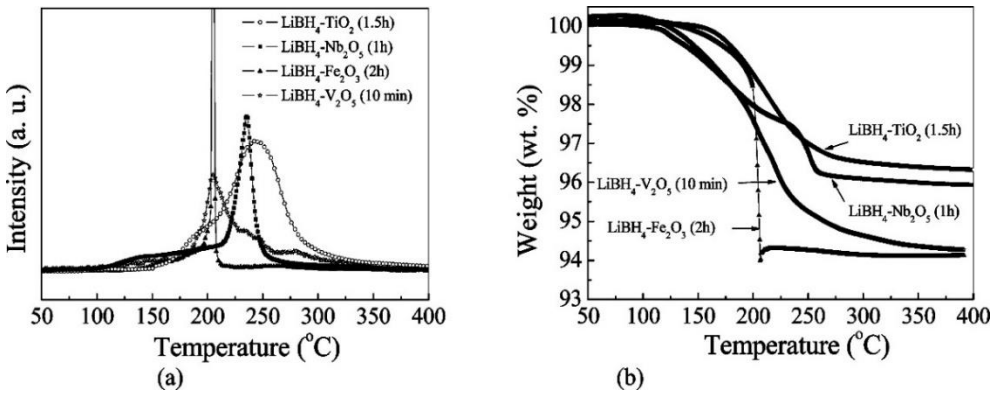

Fig. 47. MS (a) and TGA (b) results for the hydrogen evolution from ball milled $LiBH_4$ and TiO_2 mixtures with a mass ratio of 1:4, $LiBH_4/Nb_2O_5$ (1:4), $LiBH_4/Fe_2O_3$ (1:2), and $LiBH_4/V_2O_5$ (1:2), respectively. Reprinted with permission from ref [208]. Copyright 2009 ACS Publications.

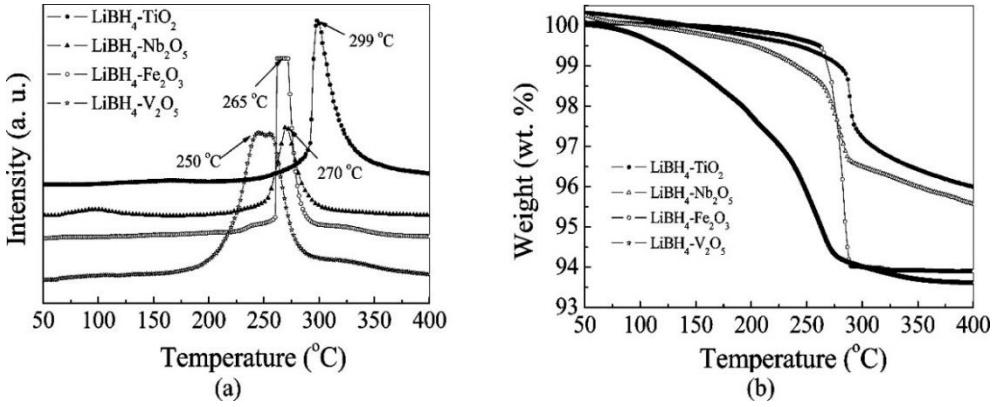

Fig. 48. MS (a) and TGA (b) results for the hydrogen evolution from $LiBH_4$-TiO_2 (mass ratios of 1:4), $LiBH_4$-Nb_2O_5 (1:4), $LiBH_4$-Fe_2O_3 (1:2), and $LiBH_4$-V_2O_5 (1:2) mixtures after 5 min hand milling. Reprinted with permission from ref [208]. Copyright 2009 ACS Publications.

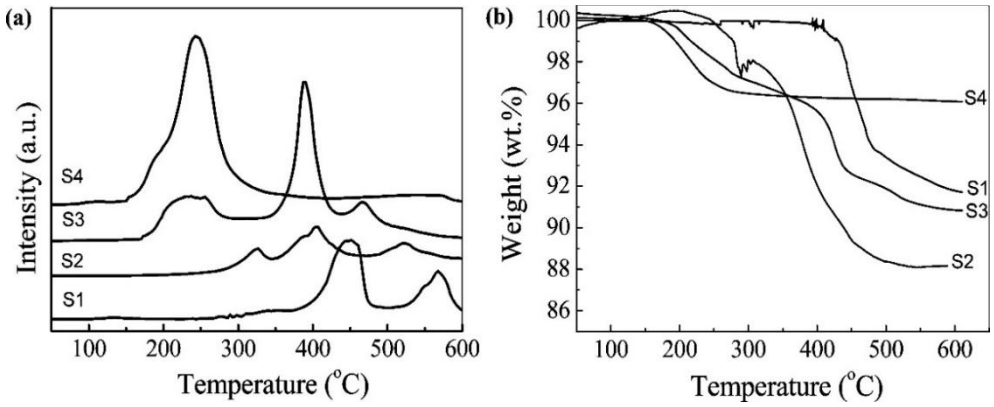

Fig. 49. MS (a) and TGA (b) results for the hydrogen evolution from $LiBH_4$ (S1) and $LiBH_4$-TiO_2 mixtures with mass ratios of 4:1 (S2), 1:1 (S3), and 1:4 (S4) after 1.5 h of ball milling. Heating rate was 10 °C/min. Reprinted with permission from ref [209]. Copyright 2008 ACS Publications.

With respect to carbon-based materials for the dehydrogenation of $LiBH_4$, Wang's group [213] found that almost the carbon additives, including graphite (G), single-walled carbon nanotubes (SWCNT) and activated carbon (AC), could improve the H-exchange kinetics and H-capacity of $LiBH_4$ to some extents. In particular, Yu et al. [214] explored the hydrogen behaviors of $LiBH_4$ doped with diverse ratios of carbon nanotubes (C_{nano}) via the ball milling process. The $LiBH_4$-C_{nano} mixtures exhibited superior dehydrogenation behaviors, wherein the hydrogen desorption started from 250 °C and the majority of H_2 was released as low as 360 °C (**Fig. 50**). Subsequently, Fang et al. found [215] that as-received SWNTs had a striking promoting effect on the de-/rehydrogenation properties of $LiBH_4$, thus rendering it reversibly for hydrogen release/uptake under markedly reduced operating temperature and pressure conditions. For the 1 h-milled $LiBH_4$-30 wt% SWNTs composites, ~11.4 wt% of H_2 was released in 50 min at 450 °C, and over 6.0 wt% H_2 could be recharged at 400 °C under an initial H-pressure of 10 MPa within 10 h. On the other hand, carbon nanotubes also exerted a space-confined effect to some extent.

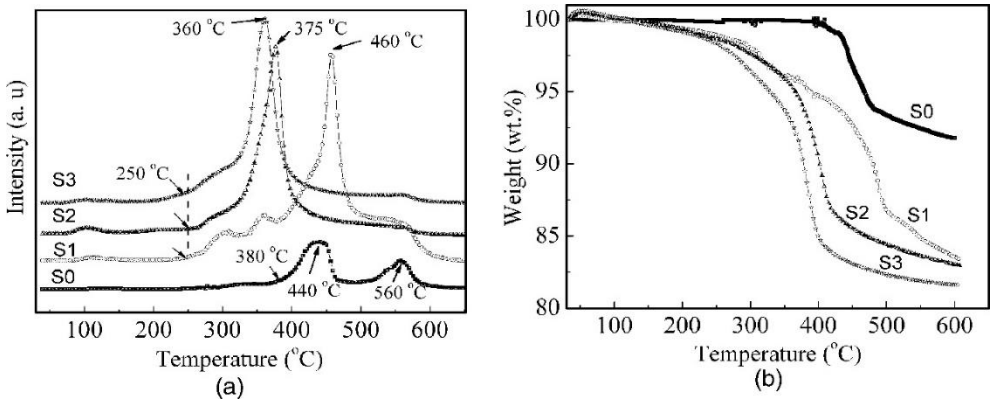

Fig. 50. MS signals for the evolution of hydrogen from $LiBH_4$ and $LiBH_4$-C_{nano} mixtures milled for 1 h. S0, $LiBH_4$;

S1, $LiBH_4$-C_{nano} (mass ratio of 2:1); S2, $LiBH_4$-C_{nano} (1:1); and S3, $LiBH_4$-C_{nano} (1:2). Reprinted with permission from ref [214]. Copyright 2007 American Institute of Physics.

.

(3) Nanostructuring

Nanoengineering has been demonstrated to be an effective method in tailoring both kinetics and thermodynamics of $LiBH_4$ during hydrogen release/uptake, mainly including space-confinement and direct synthesis strategies. **Table 6** summarizes the de-/rehydrogenation properties of $LiBH_4$ loaded upon various scaffolds or directly synthesized without supports. Similar to MgH_2, confined borohydrides may be obtained via incorporating host materials into various carbon-based porous nanostructures, ordered mesoporous silica or other mesoporous templates. Gross et al. [216] firstly proposed to incorporate $LiBH_4$ into nanoporous carbon scaffolds with the diameter pore size of 13 nm. The dehydrogenation rate of the space-confined system was ~50 times faster than that for the bulk counterpart at 300 °C. The dehydrogenation Ea was downshifted to 103 kJ/mol H_2 from 146 kJ/mol for the bulk one. Furthermore, the nanostructured $LiBH_4$ also exhibited a considerable cycling stability over multiple de-/sorption cycles. Fang et al. [217] adopted the same approach to incorporate $LiBH_4$ into AC scaffolds with a pore diameter of 2 nm, wherein both of the hydrogen sorption kinetics and thermodynamics were dramatically improved. The $LiBH_4$/AC composite began to release H_2 from merely 220 °C, ~150 °C lower than that from the bulk counterpart. Moreover, the dehydrogenation rate and dissociation H_2 pressure of $LiBH_4$/AC composite were increased by nearly one order of magnitude than those for pristine $LiBH_4$. Liu et al. [218] systematically investigated the pore-size effects of space-confined $LiBH_4$ upon the phase transition, de-/rehydrogenation properties and emission of diborane. It was indicated that both of the structural phase-transition and melting point of $LiBH_4$ shifted

to lower temperature with the reduction of pore size and finally vanished below a pore size around 4 nm. Accordingly, both of the sorption temperature (**Fig. 51**) and the emission of B_2H_6 showed a monotonic dwindling with decreasing pore size (**Fig. 52**). Excellent reversibility was achieved under 6 MPa H-pressure at 250 °C, and it might be reversible under even more moderate conditions (**Fig. 53**). This demonstrates that the reaction routes and hydrogen storage properties of $LiBH_4$ could be tailored by the pore-size effects of nanoconfinement.

Recently, Sun et al. [219] incorporated $LiBH_4$ into SBA-15 (a kind of ordered mesoporous silica) with a pore size of 9 nm through impregnation (**Fig. 54**). The space-confined system was firstly reported to release the majority of H_2 at ~100 °C without other impurity gases being discharged (**Fig. 55**). The onset desorption temperature of the confined system was lowered to 45 °C with a H-capacity of 8.5 wt% (calculated by $LiBH_4$ itself) within 10 min at 105 °C. Unfortunately, no visible reversible hydrogen storage could be observed for the $LiBH_4$/SBA-15 system even at 450 °C under 7 MPa H-pressure. Li et al. [220] developed an evaporation-induced self-assembly strategy to diversely distribute $LiBH_4$ nanoparticles with a controllable sphere, polygon and hollow geometries in poly-methylmethacrylate (PMMA). The particle size of $LiBH_4$ could be readily controlled by varying the concentrations of $LiBH_4$/THF solution (**Fig. 56**). These $LiBH_4$ nanoparticles with altered sizes exhibited remarkable effects on the dehydriding properties, where the main dehydrogenation peak evolved to 72 °C for a ~10 nm sample from 488 °C for a bulk one, as shown in **Fig. 56d**. However, the dehydrogenation capacity was not delivered by the authors. In the same year, Huang et al. [221] prepared an air-stable $LiBH_4$@PMMA composite with a loading weight of 28 wt% $LiBH_4$ as well as the diameter distribution of nanoparticles ranging from 19~73 nm. The $LiBH_4$@PMMA composite showed dramatically enhanced desorption properties in comparison with the bulk counterpart, which began to release hydrogen at 53 °C with the first main dehydrogenation peak

located at 116 °C and hydrogen desorption reached 5.2 wt% H_2 at 162 °C within 1 h (**Fig. 57**). Recently, Zang et al. [222] confined $LiBH_4$ into a novel two-dimensional layered Ti_3C_2 MXene through the impregnation method, where the onset desorption temperature was reduced to 172.6 °C. The $LiBH_4$@2Ti_3C_2 hybrid could release 9.6 wt % of H_2 at 380 °C in 1 h, whereas bulk $LiBH_4$ merely desorbed 3.2 wt% H_2 under the same conditions. The remarkably lowered desorption temperature and enhanced de-/rehydrogenation kinetics may be the synergetic effect of destabilization and nanoconfinement caused by the unique layered structure of Ti_3C_2.

With regard to low hydrogen storage capacity with a small amount loading ratio of hydrides on a nanoscaffold or matrix, novel support-free synthesis strategy of nanoscaling complex hydrides has been developed. For example, Aguey-Zinsou' group [177] prepared $NaBH_4$ particles with the size of < 30 nm by an antisolvent precipitation method, delivering a reduction of the melting point as well as the onset temperature for hydrogen release at 400 °C. Further encapsulation of these nanoparticles upon the reaction of nickel chloride at their surface enabled the synthesis of a core-shell nanostructure, $NaBH_4$@Ni. The majority of hydrogen was released as low as 418 °C, and a reversible and steady hydrogen capacity of 5 mass % was achieved within 60 min at 350 °C for $NaBH_4$@Ni, corresponding to 80% of the theoretical hydrogen content.

Table 6. Hydrogen de-/rehydrogenation properties of space-confined $LiBH_4$ in different templates.

Hydrides/supports	Loading ratio (wt%)	Infiltration methods	Hydrogen capacity [a] (wt%)		Conditions: temp (°C) (Pressure: Mpa)		Ref.
			1st Dehyd.	1st Rehyd.	Dehyd.	Rehyd.	
$LiBH_4$/SWCNT	33	Ball milling	12	-	200-500	-	[223]
$LiBH_4$/carbon	30	Solvent	13.3	-	200-300	-	[224]
$LiBH_4$/SBA-15	33	Solvent	8.5	-	105	-	[219]
$LiBH_4$/SiO_2	50	Solvent	7	-	200-350	-	[225]
$LiBH_4$/AC	28.4	Solvent	11.2	6.6	220-350	300 (5)	[217]
$LiBH_4$/NPC	10-30	Melt	7.5	~4	< 350	250 (6)	[218]
$LiBH_4$/Cu-MOFs	10	Solvent	9.5	-	60-200	-	[226]

$LiBH_4/TiO_2$	50	Solvent	11	-	220-300	-	[227]
$LiBH_4$/PMMA	28	Solvent	5.2	-	53-162	-	[221]
$LiBH_4$/Ni@C	25	Melt	10	-	200-400	-	[228]
$LiBH_4/Ti_3C_2$	33	Solvent	12.6	6.5	173-380	300 (9.5)	[222]

[a] Hydrogen capacity is given with respect to $LiBH_4$.

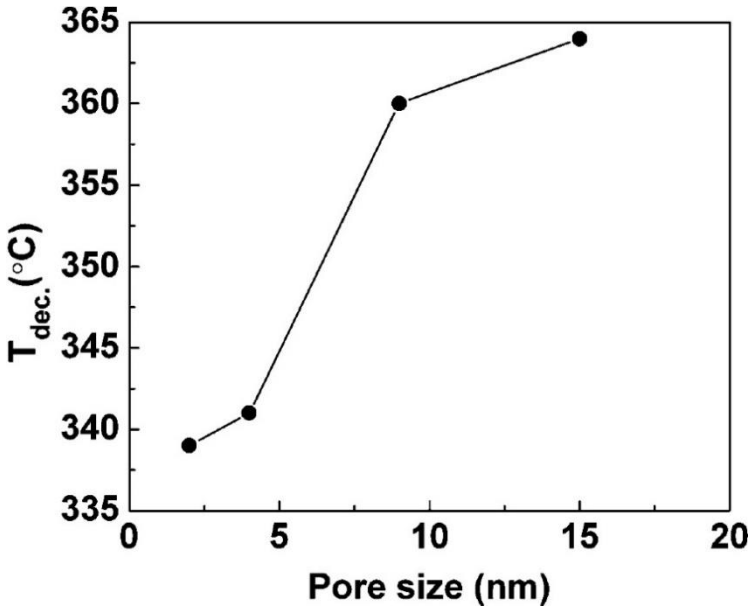

Fig. 51. Pore-size dependence of temperature with maximum dehydrogenation rate for nanoconfined $LiBH_4$ in different carbon templates with a loading of 10 wt%. Reprinted with permission from ref [218]. Copyright 2011 ACS Publications.

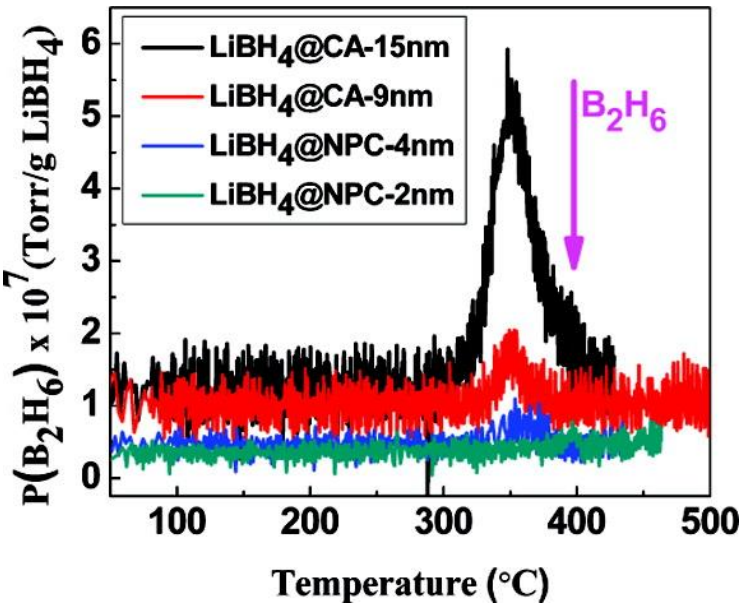

Fig. 52. B_2H_6 evolution for $LiBH_4$@NPC-2 nm, $LiBH_4$@NPC-4 nm, $LiBH_4$@CA-9 nm, and $LiBH_4$@CA-15 nm. The loading of each sample is 10 wt%. (NPC: nanoporous carbon; CA: carbon aerogel). Reprinted with permission

from ref [218]. Copyright 2011 ACS Publications.

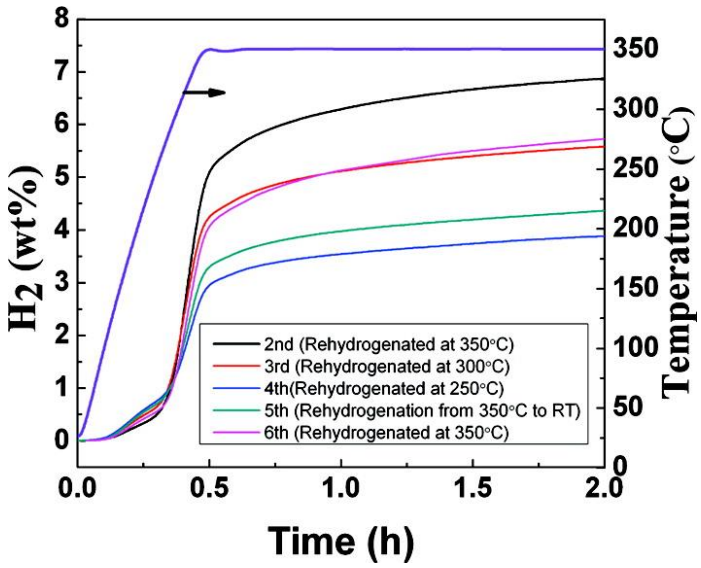

Fig. 53. Hydrogen desorption curves of nanoconfined $LiBH_4$@NPC-4 nm with an initial loading of 20 wt % (Q = 70%). Reprinted with permission from ref [218]. Copyright 2011 ACS Publications.

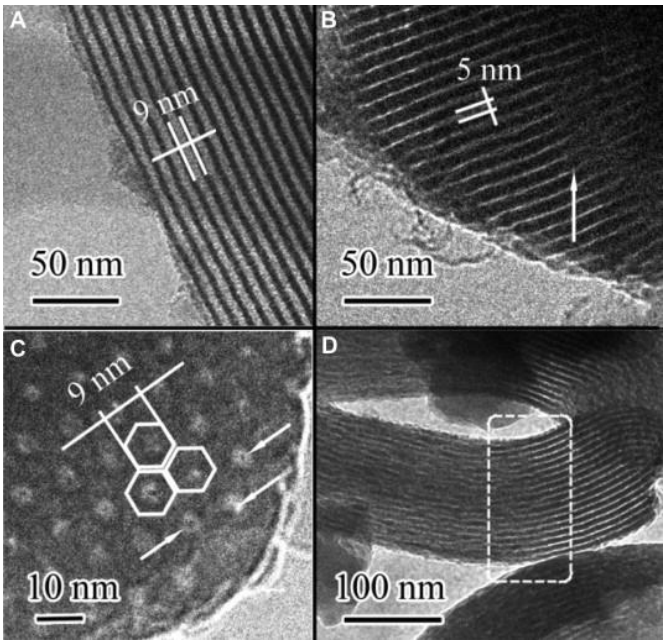

Fig. 54. TEM images of (A) SBA-15 and (B) LBH_4/SBA-15 viewing normal to the pore axis; (C) LBH_4/SBA-15 along the pore axis; (D) dehydrogenated LBH_4/SBA-15. Reprinted with permission from ref [219]. Copyright 2012 Elsevier.

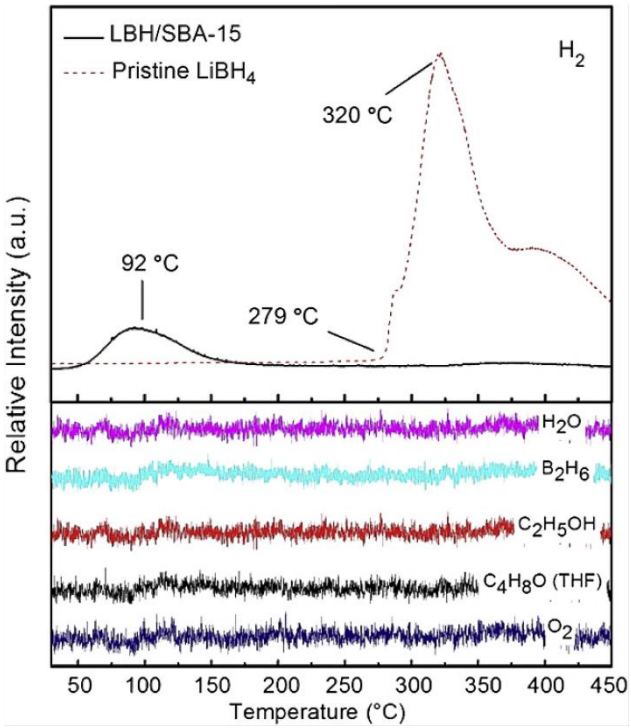

Fig. 55. TPD-MS spectra for LBH_4/SBA-15 and the pristine $LiBH_4$. Reprinted with permission from ref [219]. Copyright 2012 Elsevier.

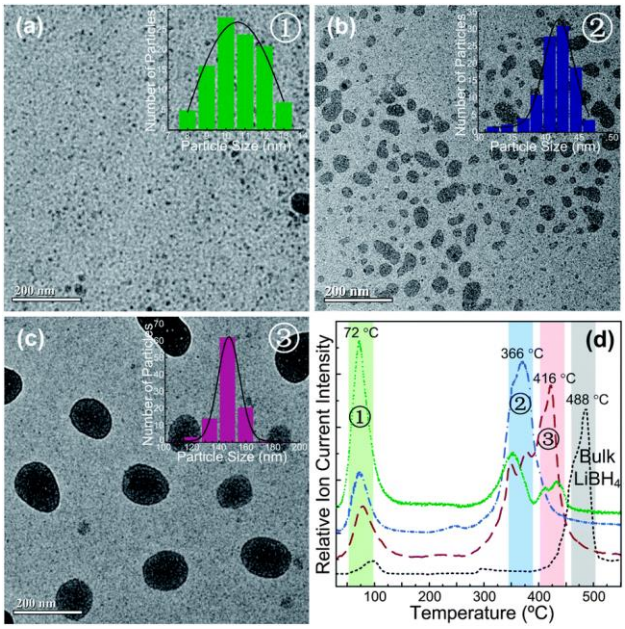

Fig. 56. TEM images for $LiBH_4$ nanoparticles with different sizes formed by changing the $LiBH_4$/THF concentration from (a) 0.10 mol/L, to (b) 0.25 mol/Land to (c) 0.50 mol/L, and (d) the normalized hydrogen desorption curves for the above three samples and bulk $LiBH_4$. Reprinted with permission from ref [220]. Copyright 2014 Royal Society

of Chemistry.

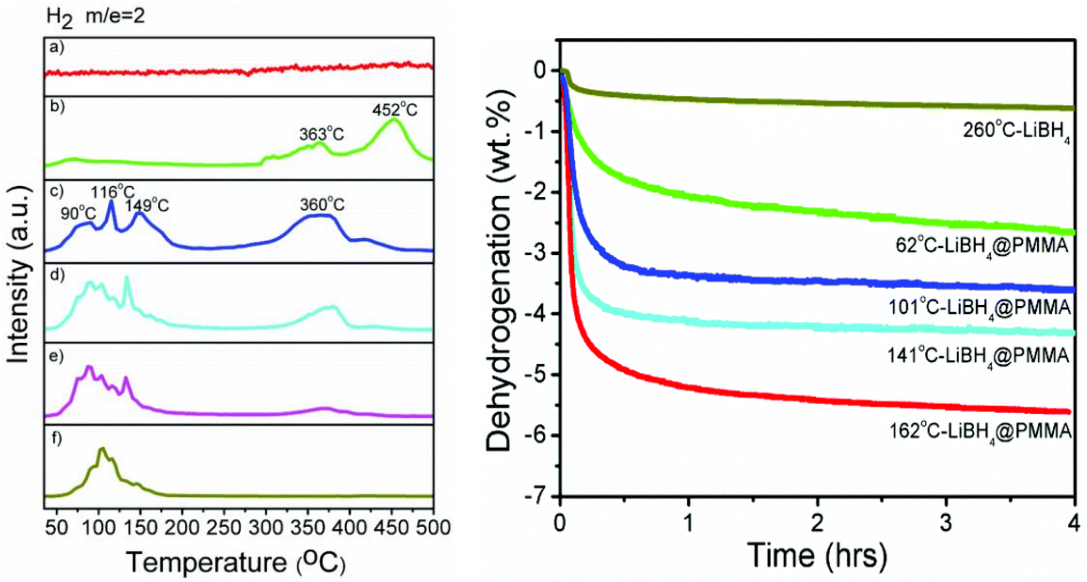

Fig. 57. MS signals of the $LiBH_4$@PMMA composite (c) and after exposure of the $LiBH_4$@PMMA composite to air for 1 h (d), 4 h (e), 8 h (f), compared with the pure PMMA (a) and $LiBH_4$ (b) (left). Isothermal dehydrogenation kinetic curves of the $LiBH_4$@PMMA composite under a vacuum at 62 °C, 101 °C, 141 °C and 162 °C, compared with pure $LiBH_4$ at 260 °C (right). Reprinted with permission from ref [221]. Copyright 2014 Royal Society of Chemistry.

(4) Reaction destabilized systems

The thermodynamics of complex hydrides can be tailored by compositing with metal hydrides to alter the reaction pathway. A representative instance for the destabilization of complex borohydrides is a $2LiBH_4$-MgH_2 system [44, 106, 229]. The de-/hydrogenation reaction of $LiBH_4$-MgH_2 composite could be described as: $MgH_2 + 2LiBH_4 \leftrightarrow 2LiH + MgB_2 + 4H_2$ (11.6 wt% of theoretical H-capacity), where the formation of MgB_2 reduces the enthalpy by 25 kJ/mol H_2 compared with pure $LiBH_4$ [229]. **Fig. 58** shows the structural transformation of the $LiBH_4$-MgH_2 system in the dehydrogenation process [230]. This destabilized composite exhibited a considerable reversible H-capacity of approximately 8 wt%, reaching 70% of the theoretical value. In addition, the

dehydrogenation temperature of the destabilized system was 225 °C under 1 bar of equilibrium H_2 pressure. To clarify the destabilized mechanism in the MgH_2-$LiBH_4$ system, Ichikawa et al. [231] introduced the hydrogen isotope tracer method. They concluded that there was a mutual interaction (H-D exchange, as seen in **Fig. 59**) between MgD_2 and $LiBH_4$, because of the observations of HD gas and the B-D stretching wagging at ~1688 cm^{-1} below the dehydrogenation temperature of $LiBH_4$. The hydrogen behaviors of $LiBH_4$ could also be tailored by ball-milling with Al or its compounds. AlB_2 intermediate was formed during de-/rehydrogenation cycles, which could improve the stability of the products and thus resulting in a lower desorption temperature of $LiBH_4$. The $LiBH_4$-Al system possessed a theoretical capacity of 8.5 wt% H_2 and could be reversibly operated at 400-450 °C, as reported by Kang et al [204]. Recently, Jiang et al. [232] investigated the effect of Al upon the dehydrogenation of $LiBH_4$ by first-principles density-functional theory calculations. The results showed that the doping of Al lowered the structural stability of $LiBH_4$, delivering a reduction in the dehydrogenation energy (E_d) with the order of $Li_8B_8H_{32}$ > $Li_8B_7AlH_{32}$ > $Li_7AlB_8H_{32}$ > $Li_8B_8AlH_{32}$. They believed that the weaker covalent bonding strength of B-H, the metal-like nature and the formation of Al-B bond were all beneficial for the improvement of dehydrogenation capability of $LiBH_4$-Al systems.

Stimulated by the above works, numerous metal or metal hydrides (Ti, Sc, V, Cr, CaH_2, TiH_2, ScH_2, CeH_2, or YH_3) were investigated theoretically and experimentally to obtain reversible composites with $LiBH_4$ [233-238]. The reactions of $LiBH_4$-M composites are expressed as similar to the $LiBH_4$-MgH_2 composite [233]:

$$2LiBH_4 + M \leftrightarrow MB_2 + 2LiH + 3H_2 \text{ [where M = Cr, Ti, Sc, V* (V* forms } V_2H)] \quad (13)$$

For $LiBH_4$-MH_x systems, the dehydrogenation reactions proceed as follows [235-238]:

$6LiBH_4 + CaH_2 \leftrightarrow 6LiH + CaB_6 + 10H_2$ (11.7 wt%) (14)

$2LiBH_4 + ScH_2 \leftrightarrow ScB_2 + 2LiH + 4H_2$ (8.9 wt%) (15)

$4LiBH_4 + YH_3 \leftrightarrow 4LiH + YB_4 + 7.5H_2$ (8:5 wt%) (16)

$6LiBH_4 + CeH_2 \leftrightarrow 6LiH + CeB_6 + 10H_2$ (7.4 wt%) (17)

The maximum theoretical capacity is up to 11.7 wt% and practical dehydrogenation capacity of ca. 9.3 wt% is achieved in the $LiBH_4$-CaH_2 system. Kou et al. [239] proposed that doping 10% NbF_5 into $2LiBH_4$-MgH_2 composite could comprehensively improve thermodynamics/kinetics and cycling performances. The doping composite could stably desorb hydrogen of ~8.31 wt% within 2.5 h under 4 bar H_2 and absorb ~8.79 wt% H_2 in 10 min under 65 bar H_2 at 400 °C even up to 20 cycling (**Fig. 60**). This means that the combination of establishing reaction destabilized system and doping catalyst or other synergies may enhance hydrogen storage behaviors in many aspects. Recently, Pan's group developed a series of reaction destabilized systems by introducing alanates or multi-hydries [240-242]. Especially, there was a significant improvement in hydrogen behaviors as MgH_2 was doped into the $6LiBH_4$-CaH_2 system, wherein ~8.0 wt% of hydrogen could be reversibly stored in the $6LiBH_4$-CaH_2-$3MgH_2$ composite below 400 °C under 100 bar H_2 with a stepwise reaction [241].

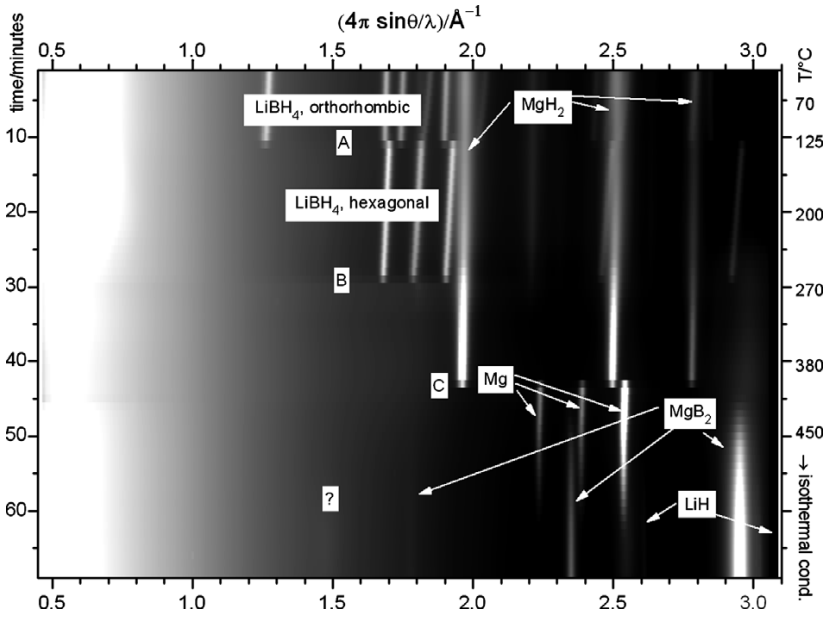

Fig. 58. In situ XRD measurement of the desorption reaction of MgH_2-$2LiBH_4$ composite. Reprinted with permission from ref [230]. Copyright 2007 Elsevier.

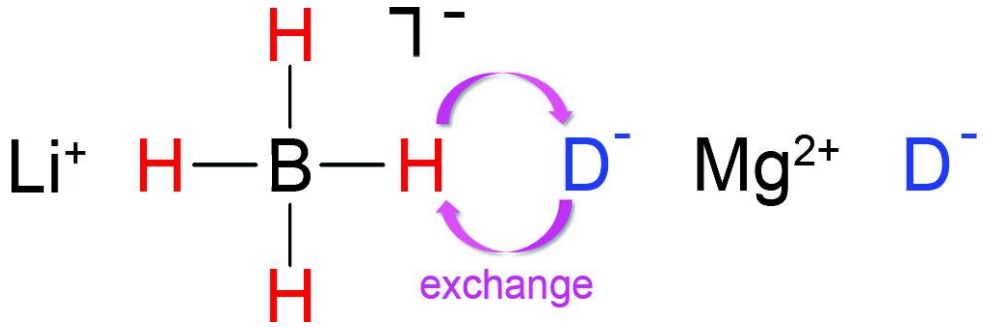

Fig. 59. Schematic illustration of H-D interaction between MgD_2 and $LiBH_4$. Reprinted with permission from ref [231]. Copyright 2010 ACS Publications.

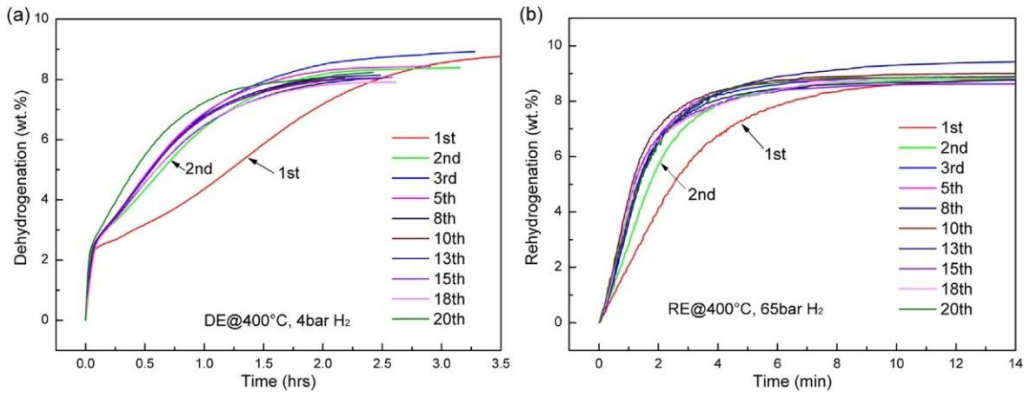

Fig. 60. Cyclic dehydrogenation (a) and rehydrogenation (b) curves of $2LiBH_4$-MgH_2 with NbF_5 in weight ratios of 40:4 for the first 20 cycles. Reprinted with permission from ref [239]. Copyright 2014 Elsevier.

3.2.3. $LiNH_2/NaNH_2/Mg(NH_2)_2$ hydrogen storage systems

In comparison with alanates and borohydrides, the studies upon amides as hydrogen storage materials are relatively less, mainly caused by NH_3 evolution during thermal decomposition [243]. Alkali-metal amides have traditionally been used as reagents in synthetic organic chemistry. In 2002, Chen et al. [126] firstly reported the feasibility of Li_3N as reversible hydrogen material, arising much attention to amides in solid hydrogen applications. Scientists and researchers have developed a great deal of complex hydrogen storage systems by incorporating amides and hydrides. **Table 7** Summary of some typical composites and their theoretical hydrogen content. Detailed information for the de-/rehydrogenation performance of amide-based hydrides systems could refer to a recent review [244].

Table 7. Hydrogen release and uptake properties of some metal N-H systems.

Systems	Reaction mechanism	Theoretical H content (wt%)	Ref.
$LiNH_2$-LiH	$LiNH_2 + 2LiH \leftrightarrow Li_3N + 2H_2$	10.3	[126]
	$LiNH_2 + LiH \leftrightarrow Li_2NH + H_2$	6.5	[126, 245]
$LiNH_2$-MgH_2	$2LiNH_2 + MgH_2 \rightarrow Li_2Mg(NH)_2 + 2H_2$ $\leftrightarrow Mg(NH_2)_2 + 2LiH$	5.6	[246, 247]
	$2LiNH_2 + MgH_2 \rightarrow Mg(NH_2)_2 + 2LiH$ $\leftrightarrow Li_2NH + MgNH + 2H_2$	5.6	[248]
$LiNH_2$-$LiBH_4$	$2LiNH_2 + LiBH_4 \leftrightarrow Li_3BN_2 + 4H_2$	11.9	[249]
$LiNH_2$-$LiAlH_4$	$2LiNH_2 + LiAlH_4 \leftrightarrow Li_3AlN_2 + 4H_2$	9.6	[250]
$Mg(NH_2)_2$-LiH	$Mg(NH_2)_2 + 8/3LiH \leftrightarrow 1/3Mg_3N_2 +$ $4/3Li_2NH + 8/3H_2$	6.9	[251]
	$Mg(NH_2)_2 + 4LiH \leftrightarrow 1/3Mg_3N_2 +$ $4/3Li_3N + 4H_2$	9.1	[252]
$Mg(NH_2)_2$-MgH_2	$Mg(NH_2)_2 + 2MgH_2 \leftrightarrow Mg_3N_2 + 4H_2$	7.4	[253]
	$Mg(NH_2)_2 + MgH_2 \leftrightarrow 2MgNH + 2H_2$	4.9	[254]
$NaNH_2$-$NaBH_4$	$2NaNH_2 + NaBH_4 \leftrightarrow Na_3BN_2 + 4H_2$	6.9	[255]
$NaNH_2$-$NaAlH_4$	$NaNH_2 + LiAlH_4 \leftrightarrow NaH + 0.67Al +$ $LiAl_{0.33}NH + 2H_2$	5.2	[256]

3.2.4. Ammoniates of borohydrides

Inspired by $Mg(BH_4)_2{\cdot}2NH_3$ system [257], where the hydrogen evolution is compelled through the combination of H^+ and H^- with the onset of hydrogen evolution at ~120 °C, various ammine complexes of borohydrides have been developed recently, including $LiBH_4{\cdot}xNH_3$ (x = 1-4), $M(BH_4)_2{\cdot}2NH_3$ (M = Mg, Ca, and Zn), $Mg(BH_4)_2{\cdot}6NH_3$, $Mg(BH_4)_2{\cdot}2NH_3$-$xMgH_2$, $Ca(BH_4)_2{\cdot}xNH_3$ (x = 1, 2, and 4), and $Al(BH_4)_3{\cdot}6NH_3$, etc. [258-266]. Among these ammoniates of borohydrides, $LiBH_4{\cdot}NH_3$ holds the highest H-density of ~18 wt% with the peak temperature of hydrogen release at ~280 °C. But the coordinate bond N: → Li^+ in $LiBH_4{\cdot}NH_3$ is readily broken, thereby liberating ammonia at the lower temperature. To suppress the ammonia release and improve the hydrogen desorption from the ammoniate, Yu et al. [259] applied $MgCl_2$, $ZnCl_2$, and $AlCl_3$ to form stable metal ammonia complexes via coordinating with ammonia. In particular, the $AlCl_3/LiBH_4{\cdot}NH_3$ composite could release a majority of H_2 by 150 °C (~9 wt.%, as shown in **Fig. 61**). $Al(BH_4)_3{\cdot}6NH_3$, another most prospective complex hydride with long-term stability in the air as well as an ideal H-capacity of 17.4 wt.%, is merely inferior to $LiBH_4{\cdot}NH_3$ [266]. It was indicated that $Al(BH_4)_3{\cdot}6NH_3$ enabled a hydrogen release over 10 wt.% H_2 below 140 °C. In addition, they found the dehydrogenation of $Al(BH_4)_2{\cdot}xNH_3/LiBH_4$ composites could be tailored via the combination of altering coordination number and doping mixed cations [267], of which over 12 wt% of pure H_2 was released for $Al(BH_4)_2{\cdot}4NH_3$-$LiBH_4$ at 120 °C (**Fig. 62**). Yu et al. [261] also investigated the dehydrogenation properties of $Al(BH_4)_3{\cdot}6NH_3$ incorporated with various metal borohydrides $M(BH_4)_n$ (M = Na, Li, Ca, Mg) and chlorides MCl_n (M = Sc, Ni, Cu, Zn, Mg, Ca, Li). They found that the addition of metal cations could remarkably enhance the dehydrogenation kinetics, exceeding 10 wt.% high-purity H_2 release in 30 min at < 120 °C for $0.5Mg(BH_4)_2/Li_2Al(BH_4)_5{\cdot}6NH_3$. However,

the difficulty in the regeneration of borohydride ammoniates mainly restrains their wide applications as mobile hydrogen carriers, though they enable high capacity hydrogen release at moderate temperatures.

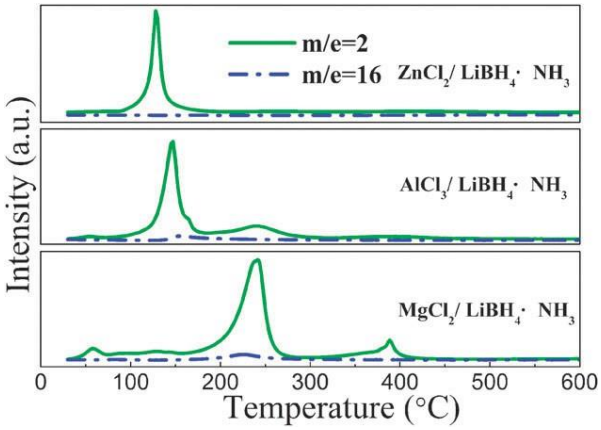

Fig. 61. MS signals for dehydrogenation of $ZnCl_2/LiBH_4{\cdot}NH_3$ (mole ratio: 1:2), $AlCl_3/LiBH_4{\cdot}NH_3$ (1:5) and $MgCl_2/LiBH_4{\cdot}NH_3$ (1:2). The emission of NH_3 is constrained by doping MCl_x. Reprinted with permission from ref [259]. Copyright 2010 Royal Society of Chemistry.

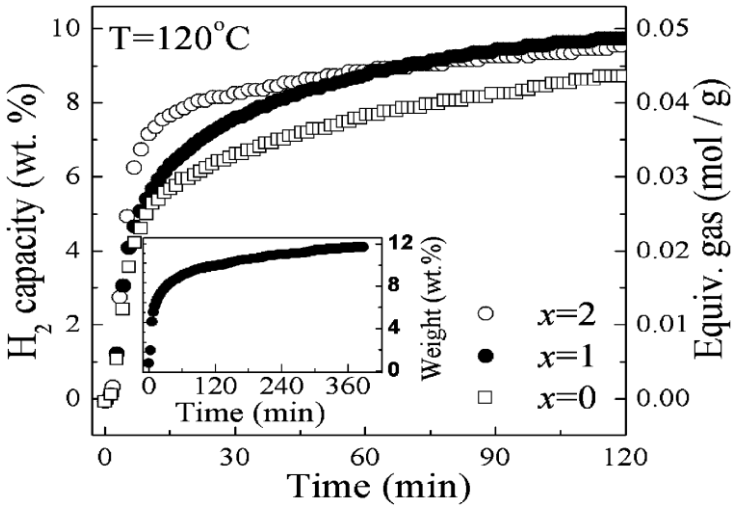

Fig. 62. Dehydrogenation curves for $Al(BH_4)_3{\cdot}4NH_3$-$nLiBH_4$ (n = 2, 1, 0) at 120 °C. Reprinted with permission from ref [267]. Copyright 2012 Royal Society of Chemistry.

4. Summary

The present review provides the recent advances of light-metal based hydrides for potential off- or on-board hydrogen applications, predominantly including Mg-based hydrides and complex hydrides (alanates, borohydrides, and amides). These solid materials can supply hydrogen via thermal decomposition or hydrolysis/alcoholysis. The threshold of commercial viability for potential reversible systems, mainly lies in relatively high decomposition temperature and poor reversibility under moderate conditions resulted from unfavourable de-/hydriding thermodynamics and/or kinetics. To overcome the thermodynamic and kinetic challenges of light-metal hydrogen materials, tremendous efforts and associated progress have been made by applying the sole strategy of catalysis, nanoscaling, alloying or compositing, etc. But the comprehensive improvements upon operating temperature, reaction kinetics and reversibly cycling properties are barely desirable. Therefore, it is expected to tailor both thermodynamics and kinetics by developing novel multi-functional materials with the combination of the above-mentioned tuning approaches, thereby achieving a synergistic effect. For instance, the integration of space-confinement and doping catalysts or reaction destabilized components could not only enhance the kinetics of hydrides with the nanoscaling and catalyzing effects, but also destabilize the thermodynamics due to the surface/interfacial role or altered reaction route in the multi-phase and multi-scale composites. Actually, the majority of the aforementioned hydrogen storage systems are barely reversible under suitable conditions for practical on-site or on-board applications. With respect to the hydrolysis and/or alcoholysis in irreversible systems, they have excellent application potential in on-site hydrogen production or fuel cell field with the advantages of mild operating temperature, environmentally benign by-products, precisely controllable hydrogen release, and high-purity H_2.

Based on the one-pass drawback of alcoholysis/hydrolysis materials, it's necessary to establish low-cost and abundant material systems that enable the high-efficient energy conversion and storage as well as facile and economic regeneration of spent raw materials in the near future.

Acknowledgements

This work was supported by the Foundation for Innovative Research Groups of the National Natural Science Foundation of China (No. NSFC51621001) and National Natural Science Foundation of China Projects (Nos. 51771075 and 51701171). Author Ouyang also thanks Guangdong Province Universities and Colleges Pearl River Scholar Funded Scheme (2014).

Competing interests

The authors declare no competing interests.

References

[1] S.J. Zinkle, G.S. Was, Materials challenges in nuclear energy, Acta Materialia, 61 (2013) 735-758.
[2] E. Romero, V.I. Novoderezhkin, R. van Grondelle, Quantum design of photosynthesis for bio-inspired solar-energy conversion, Nature, 543 (2017) 355-365.
[3] E. Kabir, P. Kumar, S. Kumar, A.A. Adelodun, K.-H. Kim, Solar energy: Potential and future prospects, Renewable and Sustainable Energy Reviews, 82 (2018) 894-900.
[4] L. Schlapbach, A. Zuttel, Hydrogen-storage materials for mobile applications, Nature, 414 (2001) 353-358.
[5] A. Zuttel, E. Callini, S. Kato, Z.O.K. Atakli, Storing Renewable Energy in the Hydrogen Cycle, Chimia, 69 (2015) 741-745.
[6] V. Stamenkovic, B. Simon Mun, M. Arenz, K. Mayrhofer, C. Lucas, G. Wang, P. Ross, N. Marković, Trends in electrocatalysis on extended and nanoscale Pt-bimetallic alloy surfaces, 2007.
[7] L. Ouyang, Z. Cao, H. Wang, R. Hu, M. Zhu, Application of dielectric barrier discharge plasma-assisted milling in energy storage materials – A review, Journal of Alloys and Compounds, 691 (2017) 422-435.
[8] W. Chen, L.Z. Ouyang, J.W. Liu, X.D. Yao, H. Wang, Z.W. Liu, M. Zhu, Hydrolysis and regeneration of sodium borohydride (NaBH4) – A combination of hydrogen production and storage, Journal of Power Sources, 359 (2017) 400-407.
[9] National Hydrogen Association; United States Department of Energy. "The History of Hydrogen".
[10] Daedalus or Science and the Future, A paper read to the Heretics, Cambridge, on February 4th, 1923 – Transcript 1993.

[11] A portfolio of power-trains for Europe: a fact-based analysis.
[12] E. Tzimas, et al., Hydrogen Storage: State-of-art and Future Perspectives, The Netherlands Official Publications of the European Communities, Pettern, 2003.
[13] Available: http://www1. eere. energy. gov/hydrogen and fuel cells/ (accessed 25. 08. 13).
[14] A.W.C. van den Berg, C.O. Areán, Materials for hydrogenstorage: current research trends and perspectives, Chem. Commun., (2008) 668-681.
[15] T. Hua, R. Ahluwalia, L. Eudy, G. Singer, B. Jermer, N. Asselin-Miller, S. Wessel, T. Patterson, J. Marcinkoski, Status of hydrogen fuel cell electric buses worldwide, Journal of Power Sources, 269 (2014) 975-993.
[16] Stetson, N. T. Hydrogen storage program area: plenary presentation (US Department of Energy, 2017).
[17] U. Eberle, M. Felderhoff, F. Schuth, Chemical and physical solutions for hydrogen storage, Angewandte Chemie, 48 (2009) 6608-6630.
[18] M. Felderhoff, C. Weidenthaler, R. von Helmolt, U. Eberle, Hydrogen storage: the remaining scientific and technological challenges, Physical chemistry chemical physics : PCCP, 9 (2007) 2643-2653.
[19] A. Züttel, Materials for hydrogen storage, Mater. Today, 6 (2003) 24-33.
[20] Y. Yürüm, A. Taralp, T.N. Veziroglu, Storage of hydrogen in nanostructured carbon materials, International Journal of Hydrogen Energy, 34 (2009) 3784-3798.
[21] E.J. Rosi N L, Eddaoudi M, et al., Hydrogen Storage in Microporous Metal-Organic Frameworks, Science, 300 (2003) 1127-1129.
[22] J. Sculley, D. Yuan, H.-C. Zhou, The current status of hydrogen storage in metal–organic frameworks—updated, Energy & Environmental Science, 4 (2011) 2721.
[23] D. Pukazhselvan, V. Kumar, S.K. Singh, High capacity hydrogen storage: Basic aspects, new developments and milestones, Nano Energy, 1 (2012) 566-589.
[24] M.P. Suh, H.J. Park, T.K. Prasad, D.-W. Lim, Hydrogen Storage in Metal–Organic Frameworks, Chemical Reviews, 112 (2011) 782-835.
[25] A. Züttel, P. Sudan, P. Mauron, T. Kiyobayashi, C. Emmenegger, L. Schlapbach, Hydrogen storage in carbon nanostructures, International Journal of Hydrogen Energy, 27 (2002) 203-212.
[26] M. Schlichtenmayer, M. Hirscher, Nanosponges for hydrogen storage, Journal of Materials Chemistry, 22 (2012) 10134.
[27] H. Jin, Y.S. Lee, I. Hong, Hydrogen adsorption characteristics of activated carbon, Catalysis Today, 120 (2007) 399-406.
[28] M. Zhu, Y. Lu, L. Ouyang, H. Wang, Thermodynamic Tuning of Mg-Based Hydrogen Storage Alloys: A Review, Materials, 6 (2013) 4654-4674.
[29] R.A. Varin, L. Guo, S. Li, C. Chiu, A. Calka, Nanostructured and Nanocomposite Light Metal-Based Compounds for Hydrogen Storage, in: O.N. Senkov, D.B. Miracle, S.A. Firstov (Eds.) Metallic Materials with High Structural Efficiency, Springer Netherlands, Dordrecht, 2004, pp. 67-78.
[30] Y. Sun, C. Shen, Q. Lai, W. Liu, D.-W. Wang, K.-F. Aguey-Zinsou, Tailoring magnesium based materials for hydrogen storage through synthesis: Current state of the art, Energy Storage Materials, 10 (2018) 168-198.
[31] S.-i. Orimo, Y. Nakamori, J.R. Eliseo, A. Züttel, C.M. Jensen, Complex Hydrides for Hydrogen Storage, Chemical Reviews, 107 (2007) 4111-4132.
[32] N.Z. Abd.Khalim Khafidz, Z. Yaakob, K.L. Lim, S.N. Timmiati, The kinetics of lightweight solid-state hydrogen storage materials: A review, International Journal of Hydrogen Energy, 41 (2016) 13131-13151.
[33] M.B. Ley, L.H. Jepsen, Y.-S. Lee, Y.W. Cho, J.M. Bellosta von Colbe, M. Dornheim, M. Rokni, J.O. Jensen, M. Sloth, Y. Filinchuk, J.E. Jørgensen, F. Besenbacher, T.R. Jensen, Complex hydrides for hydrogen storage – new

perspectives, Materials Today, 17 (2014) 122-128.
[34] J.J. Reilly, R.H. Wiswall, Reaction of hydrogen with alloys of magnesium and nickel and the formation of Mg2NiH4, Inorganic Chemistry, 7 (1968) 2254-2256.
[35] M. Li, Y. Zhu, C. Yang, J. Zhang, W. Chen, L. Li, Enhanced electrochemical hydrogen storage properties of Mg2NiH4 by coating with nano-nickel, International Journal of Hydrogen Energy, 40 (2015) 13949-13956.
[36] K. Bohmhammel, U. Wolf, G. Wolf, E. Königsberger, Thermodynamic optimization of the system magnesium–hydrogen, Thermochimica Acta, 337 (1999) 195-199.
[37] M. Dornheim, S. Doppiu, G. Barkhordarian, U. Boesenberg, T. Klassen, O. Gutfleisch, R. Bormann, Hydrogen storage in magnesium-based hydrides and hydride composites, Scripta Materialia, 56 (2007) 841-846.
[38] H.E. Kissinger, Reaction Kinetics in Differential Thermal Analysis, Analytical Chemistry, 29 (1957) 1702-1706.
[39] J.F. Stampfer, C.E. Holley, J.F. Suttle, The Magnesium-Hydrogen System1-3, Journal of the American Chemical Society, 82 (1960) 3504-3508.
[40] K.J. Jeon, H.R. Moon, A.M. Ruminski, B. Jiang, C. Kisielowski, R. Bardhan, J.J. Urban, Air-stable magnesium nanocomposites provide rapid and high-capacity hydrogen storage without using heavy-metal catalysts, Nat Mater, 10 (2011) 286-290.
[41] J. Cui, H. Wang, J. Liu, L. Ouyang, Q. Zhang, D. Sun, X. Yao, M. Zhu, Remarkable enhancement in dehydrogenation of MgH2 by a nano-coating of multi-valence Ti-based catalysts, Journal of Materials Chemistry A, 1 (2013) 5603.
[42] G. Xia, Y. Tan, X. Chen, D. Sun, Z. Guo, H. Liu, L. Ouyang, M. Zhu, X. Yu, Monodisperse magnesium hydride nanoparticles uniformly self-assembled on graphene, Advanced materials, 27 (2015) 5981-5988.
[43] L.Z. Ouyang, X.S. Yang, M. Zhu, J.W. Liu, H.W. Dong, D.L. Sun, J. Zou, X.D. Yao, Enhanced Hydrogen Storage Kinetics and Stability by Synergistic Effects of in Situ Formed CeH2.73 and Ni in CeH2.73-MgH2-Ni Nanocomposites, The Journal of Physical Chemistry C, 118 (2014) 7808-7820.
[44] J.J. Vajo, F. Mertens, C.C. Ahn, R.C. Bowman, B. Fultz, Altering Hydrogen Storage Properties by Hydride Destabilization through Alloy Formation: LiH and MgH2 Destabilized with Si, The Journal of Physical Chemistry B, 108 (2004) 13977-13983.
[45] H.C. Zhong, H. Wang, J.W. Liu, D.L. Sun, M. Zhu, Altered desorption enthalpy of MgH2 by the reversible formation of Mg(In) solid solution, Scripta Materialia, 65 (2011) 285-287.
[46] L.Z. Ouyang, Z.J. Cao, H. Wang, J.W. Liu, D.L. Sun, Q.A. Zhang, M. Zhu, Dual-tuning effect of In on the thermodynamic and kinetic properties of Mg2Ni dehydrogenation, International Journal of Hydrogen Energy, 38 (2013) 8881-8887.
[47] K.-F. Aguey-Zinsou, J.-R. Ares-Fernández, Hydrogen in magnesium: new perspectives toward functional stores, Energy & Environmental Science, 3 (2010) 526.
[48] A. Zaluska, L. Zaluski, J.O. Ström–Olsen, Nanocrystalline magnesium for hydrogen storage, Journal of Alloys and Compounds, 288 (1999) 217-225.
[49] J. Qu, Y. Wang, L. Xie, J. Zheng, Y. Liu, X. Li, Superior hydrogen absorption and desorption behavior of Mg thin films, Journal of Power Sources, 186 (2009) 515-520.
[50] A. Zaluska, L. Zaluski, J.O. Ström-Olsen, Structure, catalysis and atomic reactions on the nano-scale: a systematic approach to metal hydrides for hydrogen storage, Applied Physics A, 72 (2001) 157-165.
[51] A.F. Gross, C.C. Ahn, S.L. Van Atta, P. Liu, J.J. Vajo, Fabrication and hydrogen sorption behaviour of nanoparticulate MgH2 incorporated in a porous carbon host, Nanotechnology, 20 (2009) 204005.
[52] T.K. Nielsen, K. Manickam, M. Hirscher, F. Besenbacher, T.R. Jensen, Confinement of MgH2 Nanoclusters within Nanoporous Aerogel Scaffold Materials, ACS Nano, 3 (2009) 3521-3528.

[53] Y.S. Au, M.K. Obbink, S. Srinivasan, P.C.M.M. Magusin, K.P. de Jong, P.E. de Jongh, The Size Dependence of Hydrogen Mobility and Sorption Kinetics for Carbon-Supported MgH2Particles, Advanced Functional Materials, 24 (2014) 3604-3611.
[54] G. Liang, J. Huot, S. Boily, A. Van Neste, R. Schulz, Catalytic effect of transition metals on hydrogen sorption in nanocrystalline ball milled MgH2–Tm (Tm=Ti, V, Mn, Fe and Ni) systems, Journal of Alloys and Compounds, 292 (1999) 247-252.
[55] L.E.A. Berlouis, E. Cabrera, E. Hall-Barientos, P.J. Hall, S.B. Dodd, S. Morris, M.A. Imam, Thermal analysis investigation of hydriding properties of nanocrystalline Mg–Ni- and Mg–Fe-based alloys prepared by high-energy ball milling, Journal of Materials Research, 16 (2011) 45-57.
[56] J. Yin, T. Yamada, O. Yoshinari, K. Tanaka, Improvement of hydrogen storage properties of Mg-Ni alloys by rare-earth addition, Materials Transactions, 42 (2001) 712-716.
[57] J. Huot, J. Pelletier, L. Lurio, M. Sutton, R. Schulz, Investigation of dehydrogenation mechanism of MgH2–Nb nanocomposites, Journal of Alloys and Compounds, 348 (2003) 319-324.
[58] J. Huot, J.F. Pelletier, G. Liang, M. Sutton, R. Schulz, Structure of nanocomposite metal hydrides, Journal of Alloys and Compounds, 330-332 (2002) 727-731.
[59] J.F. Pelletier, J. Huot, M. Sutton, R. Schulz, A.R. Sandy, L.B. Lurio, S.G.J. Mochrie, Hydrogen desorption mechanism inMgH2−Nbnanocomposites, Physical Review B, 63 (2001).
[60] Y. Liu, H. Du, X. Zhang, Y. Yang, M. Gao, H. Pan, Superior catalytic activity derived from a two-dimensional Ti 3 C 2 precursor towards the hydrogen storage reaction of magnesium hydride, Chemical Communications, 52 (2016) 705-708.
[61] K. Wang, H. Du, Z. Wang, M. Gao, H. Pan, Y. Liu, Novel MAX-phase Ti3AlC2 catalyst for improving the reversible hydrogen storage properties of MgH2, International journal of hydrogen energy, 42 (2017) 4244-4251.
[62] Y. Pang, T. Yuan, J. Yang, M. Gao, H. Pan, Y. Liu, S. Zheng, In situ formation of Al3Ti, MgF2 and Al and their superior synergetic effects on reversible hydrogen storage of MgH2, Catalysis Today, 318 (2018) 107-112.
[63] Z. Shen, Z. Wang, M. Zhang, M. Gao, J. Hu, F. Du, Y. Liu, H. Pan, A novel solid-solution MXene (Ti0. 5V0. 5) 3C2 with high catalytic activity for hydrogen storage in MgH2, Materialia, 1 (2018) 114-120.
[64] Z. Wang, X. Zhang, Z. Ren, Y. Liu, J. Hu, H. Li, M. Gao, H. Pan, Y. Liu, In situ formed ultrafine NbTi nanocrystals from a NbTiC solid-solution MXene for hydrogen storage in MgH 2, Journal of Materials Chemistry A, 7 (2019) 14244-14252.
[65] N. Hanada, T. Ichikawa, S. Hino, H. Fujii, Remarkable improvement of hydrogen sorption kinetics in magnesium catalyzed with Nb2O5, Journal of Alloys and Compounds, 420 (2006) 46-49.
[66] N. Hanada, T. Ichikawa, H. Fujii, Hydrogen absorption kinetics of the catalyzed MgH2 by niobium oxide, Journal of Alloys and Compounds, 446-447 (2007) 67-71.
[67] T. Klassen, W. Oelerich, R. Bormann, Nanocrystalline Mg-Based Hydrides: Hydrogen Storage for the Zero-Emission Vehicle, Journal of Metastable and Nanocrystalline Materials, 10 (2001) 603-608.
[68] W. Oelerich, T. Klassen, R. Bormann, Metal oxides as catalysts for improved hydrogen sorption in nanocrystalline Mg-based materials, Journal of Alloys and Compounds, 315 (2001) 237-242.
[69] G. Barkhordarian, T. Klassen, R. Bormann, Catalytic Mechanism of Transition-Metal Compounds on Mg Hydrogen Sorption Reaction, The Journal of Physical Chemistry B, 110 (2006) 11020-11024.
[70] G. Barkhordarian, T. Klassen, R. Bormann, Fast hydrogen sorption kinetics of nanocrystalline Mg using Nb2O5 as catalyst, Scripta Materialia, 49 (2003) 213-217.
[71] S.T. Sabitu, A.J. Goudy, Dehydrogenation Kinetics and Modeling Studies of MgH2 Enhanced by Transition Metal Oxide Catalysts Using Constant Pressure Thermodynamic Driving Forces, Metals, 2 (2012) 219-228.
[72] X. Zhang, Z. Leng, M. Gao, J. Hu, F. Du, J. Yao, H. Pan, Y. Liu, Enhanced hydrogen storage properties of

MgH2 catalyzed with carbon-supported nanocrystalline TiO2, Journal of Power Sources, 398 (2018) 183-192.
[73] X. Zhang, Z. Shen, N. Jian, J. Hu, F. Du, J. Yao, M. Gao, Y. Liu, H. Pan, A novel complex oxide TiVO3. 5 as a highly active catalytic precursor for improving the hydrogen storage properties of MgH2, International Journal of Hydrogen Energy, 43 (2018) 23327-23335.
[74] Z. Wang, Z. Ren, N. Jian, M. Gao, J. Hu, F. Du, H. Pan, Y. Liu, Vanadium oxide nanoparticles supported on cubic carbon nanoboxes as highly active catalyst precursors for hydrogen storage in MgH2, Journal of Materials Chemistry A, 6 (2018) 16177-16185.
[75] K. Wang, X. Zhang, Z. Ren, X. Zhang, J. Hu, M. Gao, H. Pan, Y. Liu, Nitrogen-stimulated superior catalytic activity of niobium oxide for fast full hydrogenation of magnesium at ambient temperature, Energy Storage Materials, 23 (2019) 79-87.
[76] I.E. Malka, M. Pisarek, T. Czujko, J. Bystrzycki, A study of the ZrF4, NbF5, TaF5, and TiCl3 influences on the MgH2 sorption properties, International Journal of Hydrogen Energy, 36 (2011) 12909-12917.
[77] I.E. Malka, T. Czujko, J. Bystrzycki, Catalytic effect of halide additives ball milled with magnesium hydride, International Journal of Hydrogen Energy, 35 (2010) 1706-1712.
[78] J. Cui, J. Liu, H. Wang, L. Ouyang, D. Sun, M. Zhu, X. Yao, Mg–TM (TM: Ti, Nb, V, Co, Mo or Ni) core–shell like nanostructures: synthesis, hydrogen storage performance and catalytic mechanism, J. Mater. Chem. A, 2 (2014) 9645-9655.
[79] H.-J. Lin, J.-J. Tang, Q. Yu, H. Wang, L.-Z. Ouyang, Y.-J. Zhao, J.-W. Liu, W.-H. Wang, M. Zhu, Symbiotic CeH 2.73 /CeO 2 catalyst: A novel hydrogen pump, Nano Energy, 9 (2014) 80-87.
[80] A.C. Dillon, K.M. Jones, T.A. Bekkedahl, C.H. Kiang, D.S. Bethune, M.J. Heben, Storage of hydrogen in single-walled carbon nanotubes, Nature, 386 (1997) 377-379.
[81] X. Yao, C. Wu, A. Du, J. Zou, Z. Zhu, P. Wang, H. Cheng, S. Smith, G. Lu, Metallic and Carbon Nanotube-Catalyzed Coupling of Hydrogenation in Magnesium, Journal of the American Chemical Society, 129 (2007) 15650-15654.
[82] C.Z. Wu, P. Wang, X. Yao, C. Liu, D.M. Chen, G.Q. Lu, H.M. Cheng, Effect of carbon/noncarbon addition on hydrogen storage behaviors of magnesium hydride, Journal of Alloys and Compounds, 414 (2006) 259-264.
[83] R. Bogerd, P. Adelhelm, J.H. Meeldijk, K.P. de Jong, P.E. de Jongh, The structural characterization and H(2) sorption properties of carbon-supported Mg(1-x)Nix nanocrystallites, Nanotechnology, 20 (2009) 204019.
[84] P. Jasen, E. Gonzalez, G. Brizuela, O. Nagel, G. Gonzalez, A. Juan, A theoretical study of the electronic structure and bonding of the monoclinic phase of Mg2NiH4Mg2NiH4, International Journal of Hydrogen Energy, 32 (2007) 4943-4948.
[85] X. Zhang, R. Yang, J. Qu, W. Zhao, L. Xie, W. Tian, X. Li, The synthesis and hydrogen storage properties of pure nanostructured Mg2FeH6, Nanotechnology, 21 (2010) 095706.
[86] J. Huot, S. Boily, E. Akiba, R. Schulz, Direct synthesis of Mg2FeH6 by mechanical alloying, Journal of Alloys and Compounds, 280 (1998) 306-309.
[87] P. Selvam, K. Yvon, Synthesis of Mg2FeH6, Mg2CoH5 and Mg2NiH4 by high-pressure sintering of the elements, International Journal of Hydrogen Energy, 16 (1991) 615-617.
[88] M.G. Verón, A.M. Condó, F.C. Gennari, Effective synthesis of Mg2CoH5 by reactive mechanical milling and its hydrogen sorption behavior after cycling, International Journal of Hydrogen Energy, 38 (2013) 973-981.
[89] S. Yajima, H. Kayano, H. Toma, Hydrogen sorption in La 2 Mg 17, Journal of the Less-Common Metals, 55 (1977) 139-141.
[90] R.V. Denys, A.A. Poletaev, J.K. Solberg, B.P. Tarasov, V.A. Yartys, LaMg11 with a giant unit cell synthesized by hydrogen metallurgy: Crystal structure and hydrogenation behavior, Acta Materialia, 58 (2010) 2510-2519.
[91] L.Z. Ouyang, F.X. Qin, M. Zhu, The hydrogen storage behavior of Mg3La and Mg3LaNi0.1, Scripta

Materialia, 55 (2006) 1075-1078.
[92] L. Ouyang, H. Dong, C. Peng, L. Sun, M. Zhu, A new type of Mg-based metal hydride with promising hydrogen storage properties, International Journal of Hydrogen Energy, 32 (2007) 3929-3935.
[93] L.Z. Ouyang, H.W. Dong, M. Zhu, Mg3Mm compound based hydrogen storage materials, Journal of Alloys and Compounds, 446-447 (2007) 124-128.
[94] S.M. Zhu, J.F. Nie, M.A. Gibson, M.A. Easton, On the unexpected formation of rare earth hydrides in magnesium–rare earth casting alloys, Scripta Materialia, 77 (2014) 21-24.
[95] L.Z. Ouyang, X.S. Yang, H.W. Dong, M. Zhu, Structure and hydrogen storage properties of Mg3Pr and Mg3PrNi0.1 alloys, Scripta Materialia, 61 (2009) 339-342.
[96] V. Berube, M.S. Dresselhaus, G. Chen, Entropy stabilization of deformed regions characterized by an excess volume for hydrogen storage applications, International Journal of Hydrogen Energy, 34 (2009) 1862-1872.
[97] L. Ouyang, S. Ye, H. Dong, M. Zhu, Effect of interfacial free energy on hydriding reaction of Mg–Ni thin films, Applied physics letters, 90 (2007) 021917.
[98] R.W.P. Wagemans, J.H. van Lenthe, P.E. de Jongh, A.J. van Dillen, K.P. de Jong, Hydrogen Storage in Magnesium Clusters: Quantum Chemical Study, Journal of the American Chemical Society, 127 (2005) 16675-16680.
[99] M. Paskevicius, D.A. Sheppard, C.E. Buckley, Thermodynamic Changes in Mechanochemically Synthesized Magnesium Hydride Nanoparticles, Journal of the American Chemical Society, 132 (2010) 5077-5083.
[100] W. Li, C. Li, H. Ma, J. Chen, Magnesium Nanowires: Enhanced Kinetics for Hydrogen Absorption and Desorption, Journal of the American Chemical Society, 129 (2007) 6710-6711.
[101] M. Konarova, A. Tanksale, J. Norberto Beltramini, G. Qing Lu, Effects of nano-confinement on the hydrogen desorption properties of MgH2, Nano Energy, 2 (2013) 98-104.
[102] M. Polanski, J. Bystrzycki, The influence of different additives on the solid-state reaction of magnesium hydride (MgH2) with Si, International Journal of Hydrogen Energy, 34 (2009) 7692-7699.
[103] G.S. Walker, M. Abbas, D.M. Grant, C. Udeh, Destabilisation of magnesium hydride by germanium as a new potential multicomponent hydrogen storage system, Chemical communications, 47 (2011) 8001-8003.
[104] H. Wang, H. Zhong, L. Ouyang, J. Liu, D. Sun, Q. Zhang, M. Zhu, Fully Reversible De/hydriding of Mg Base Solid Solutions with Reduced Reaction Enthalpy and Enhanced Kinetics, The Journal of Physical Chemistry C, 118 (2014) 12087-12096.
[105] C. Zhou, Z.Z. Fang, J. Lu, X. Zhang, Thermodynamic and Kinetic Destabilization of Magnesium Hydride Using Mg–In Solid Solution Alloys, Journal of the American Chemical Society, 135 (2013) 10982-10985.
[106] F.E. Pinkerton, M.S. Meyer, G.P. Meisner, M.P. Balogh, J.J. Vajo, Phase Boundaries and Reversibility of LiBH4/MgH2 Hydrogen Storage Material, The Journal of Physical Chemistry C, 111 (2007) 12881-12885.
[107] U. Bösenberg, J.W. Kim, D. Gosslar, N. Eigen, T.R. Jensen, J.M.B. von Colbe, Y. Zhou, M. Dahms, D.H. Kim, R. Günther, Role of additives in LiBH4–MgH2 reactive hydride composites for sorption kinetics, Acta Materialia, 58 (2010) 3381-3389.
[108] U. Bösenberg, D.B. Ravnsbæk, H. Hagemann, V. D'Anna, C.B. Minella, C. Pistidda, W. van Beek, T.R. Jensen, R. Bormann, M. Dornheim, Pressure and Temperature Influence on the Desorption Pathway of the LiBH4−MgH2 Composite System, The Journal of Physical Chemistry C, 114 (2010) 15212-15217.
[109] P. Wang, H.F. Zhang, B.Z. Ding, Z.Q. Hu, Structural and hydriding properties of composite Mg–ZrFe1.4Cr0.6, Acta Materialia, 49 (2001) 921-926.
[110] G. Liang, J. Huot, S. Boily, A. Van Neste, R. Schulz, Hydrogen storage in mechanically milled Mg–LaNi5 and MgH2–LaNi5 composites, Journal of Alloys and Compounds, 297 (2000) 261-265.
[111] P. Mandal, K. Dutta, K. Ramakrishna, K. Sapru, O.N. Srivastava, Synthesis, characterization and

hydrogenation behaviour of Mg-ξwt.%FeTi(Mn) and La2Mg17—ξwt.%LaNi5—new hydrogen storage composite alloys, Journal of Alloys and Compounds, 184 (1992) 1-9.
[112] S.S. Sai Raman, O.N. Srivastava, Hydrogenation behaviour of the new composite storage materials Mg-x wt.% CFMmNi5, Journal of Alloys and Compounds, 241 (1996) 167-174.
[113] Q.A. Zhang, D.D. Liu, Q.Q. Wang, F. Fang, D.L. Sun, L.Z. Ouyang, M. Zhu, Superior hydrogen storage kinetics of Mg12YNi alloy with a long-period stacking ordered phase, Scripta Materialia, 65 (2011) 233-236.
[114] J.W. Liu, C.C. Zou, H. Wang, L.Z. Ouyang, M. Zhu, Facilitating de/hydrogenation by long-period stacking ordered structure in Mg based alloys, International Journal of Hydrogen Energy, 38 (2013) 10438-10445.
[115] L.Z. Ouyang, Z.J. Cao, H. Wang, J.W. Liu, D.L. Sun, Q.A. Zhang, M. Zhu, Enhanced dehydriding thermodynamics and kinetics in Mg(In)–MgF2 composite directly synthesized by plasma milling, Journal of Alloys and Compounds, 586 (2014) 113-117.
[116] Z. Cao, L. Ouyang, Y. Wu, H. Wang, J. Liu, F. Fang, D. Sun, Q. Zhang, M. Zhu, Dual-tuning effects of In, Al, and Ti on the thermodynamics and kinetics of Mg 85 In 5 Al 5 Ti 5 alloy synthesized by plasma milling, Journal of Alloys and Compounds, 623 (2015) 354-358.
[117] F.P. Luo, H. Wang, L.Z. Ouyang, M.Q. Zeng, J.W. Liu, M. Zhu, Enhanced reversible hydrogen storage properties of a Mg–In–Y ternary solid solution, International Journal of Hydrogen Energy, 38 (2013) 10912-10918.
[118] Y.S. Lu, M. Zhu, H. Wang, Z.M. Li, L.Z. Ouyang, J.W. Liu, Reversible de-/hydriding characteristics of a novel Mg18In1Ni3 alloy, International Journal of Hydrogen Energy, 39 (2014) 14033-14038.
[119] M.V. Lototskyy, I. Tolj, L. Pickering, C. Sita, F. Barbir, V. Yartys, The use of metal hydrides in fuel cell applications, Progress in Natural Science: Materials International, 27 (2017) 3-20.
[120] W.H. Stockmayer, D.W. Rice, C.C. Stephenson, Thermodynamic properties of sodium borohydride and aqueous borohydride ion, Journal of the American Chemical Society, 77 (1955) 1980-1983.
[121] M. Wang, L. Ouyang, C. Peng, X. Zhu, W. Zhu, H. Shao, M. Zhu, Synthesis and hydrolysis of NaZn(BH4)3 and its ammoniates, Journal of Materials Chemistry A, 5 (2017) 17012-17020.
[122] M. Ma, L. Ouyang, J. Liu, H. Wang, H. Shao, M. Zhu, Air-stable hydrogen generation materials and enhanced hydrolysis performance of MgH 2 -LiNH 2 composites, Journal of Power Sources, 359 (2017) 427-434.
[123] P. Chen, M. Zhu, Recent progress in hydrogen storage, Materials Today, 11 (2008) 36-43.
[124] S. Orimo, Y. Nakamori, G. Kitahara, K. Miwa, N. Ohba, S. Towata, A. Züttel, Dehydriding and rehydriding reactions of LiBH4, Journal of Alloys and Compounds, 404-406 (2005) 427-430.
[125] B. Bogdanović, M. Schwickardi, Ti-doped alkali metal aluminium hydrides as potential novel reversible hydrogen storage materials1Invited paper presented at the International Symposium on Metal–Hydrogen Systems, Les Diablerets, August 25–30, 1996, Switzerland.1, Journal of Alloys and Compounds, 253-254 (1997) 1-9.
[126] P. Chen, Z. Xiong, J. Luo, J. Lin, K.L. Tan, Interaction of hydrogen with metal nitrides and imides, Nature, 420 (2002) 302.
[127] A. Züttel, S. Rentsch, P. Fischer, P. Wenger, P. Sudan, P. Mauron, C. Emmenegger, Hydrogen storage properties of LiBH4, Journal of Alloys and Compounds, 356 (2003) 515-520.
[128] J.-P. Soulié, G. Renaudin, R. Černý, K. Yvon, Lithium boro-hydride LiBH4: I. Crystal structure, Journal of alloys and compounds, 346 (2002) 200-205.
[129] M. Fichtner, O. Fuhr, O. Kircher, Magnesium alanate—a material for reversible hydrogen storage?, Journal of Alloys and Compounds, 356-357 (2003) 418-422.
[130] J. Block, A. Gray, The thermal decomposition of lithium aluminum hydride, Inorganic Chemistry, 4 (1965) 304-305.
[131] L. Li, F. Qiu, Y. Wang, G. Liu, Y. Xu, C. An, Y. Wang, L. Jiao, H. Yuan, TiN catalyst for the reversible hydrogen storage performance of sodium alanate system, Journal of Materials Chemistry, 22 (2012) 13782.

[132] M.W. Chase Jr, JANAF thermochemical table, J. Phys. Chem. Ref. Data, 14 (1985) Supplement No. 1.
[133] B.C. Hauback, H.W. Brinks, H. Fjellvåg, Accurate structure of LiAlD4 studied by combined powder neutron and X-ray diffraction, Journal of Alloys and Compounds, 346 (2002) 184-189.
[134] B.C. Hauback, H.W. Brinks, C.M. Jensen, K. Murphy, A.J. Maeland, Neutron diffraction structure determination of NaAlD4, Journal of Alloys and Compounds, 358 (2003) 142-145.
[135] A. Fossdal, H.W. Brinks, M. Fichtner, B.C. Hauback, Determination of the crystal structure of Mg(AlH4)2 by combined X-ray and neutron diffraction, Journal of Alloys and Compounds, 387 (2005) 47-51.
[136] E.H. Majzoub, K.J. Gross, Titanium–halide catalyst-precursors in sodium aluminum hydrides, Journal of Alloys and Compounds, 356-357 (2003) 363-367.
[137] D.L. Anton, Hydrogen desorption kinetics in transition metal modified NaAlH4, Journal of Alloys and Compounds, 356-357 (2003) 400-404.
[138] P. Wang, X.D. Kang, H.M. Cheng, Improved hydrogen storage of TiF3-doped NaAlH4, Chemphyschem : a European journal of chemical physics and physical chemistry, 6 (2005) 2488-2491.
[139] L. Li, Y. Wang, F. Qiu, Y. Wang, Y. Xu, C. An, L. Jiao, H. Yuan, Reversible hydrogen storage properties of NaAlH4 enhanced with TiN catalyst, Journal of Alloys and Compounds, 566 (2013) 137-141.
[140] Y. Wang, Q. Ren, Y. Wang, L. Li, D. Song, L. Jiao, H. Yuan, A facile two-step synthesis and dehydrogenation properties of NaAlH4 catalyzed with Co–B, International Journal of Hydrogen Energy, 35 (2010) 11004-11008.
[141] X.-D. Kang, P. Wang, H.-M. Cheng, Electron microscopy study of Ti-doped sodium aluminum hydride prepared by mechanical milling Na H⁄ Al with Ti powder, Journal of applied physics, 100 (2006) 034914.
[142] M. Fichtner, O. Fuhr, O. Kircher, J. Rothe, Small Ti clusters for catalysis of hydrogen exchange in NaAlH4, Nanotechnology, 14 (2003) 778.
[143] X. Zhang, Z. Ren, X. Zhang, M. Gao, H. Pan, Y. Liu, Triggering highly stable catalytic activity of metallic titanium for hydrogen storage in NaAlH 4 by preparing ultrafine nanoparticles, Journal of materials chemistry A, 7 (2019) 4651-4659.
[144] C. Rongeat, I. Llamas Jansa, S. Oswald, L. Schultz, O. Gutfleisch, Mechanochemical synthesis and XPS analysis of sodium alanate with different additives, Acta Materialia, 57 (2009) 5563-5570.
[145] C. Rongeat, N. Scheerbaum, L. Schultz, O. Gutfleisch, Catalysis of H2 sorption in NaAlH4: General description and new insights, Acta Materialia, 59 (2011) 1725-1733.
[146] B. Bogdanović, M. Felderhoff, A. Pommerin, F. Schüth, N. Spielkamp, Advanced Hydrogen-Storage Materials Based on Sc-, Ce-, and Pr-Doped NaAlH4, Advanced materials, 18 (2006) 1198-1201.
[147] J. Hu, S. Ren, R. Witter, M. Fichtner, Catalytic Influence of Various Cerium Precursors on the Hydrogen Sorption Properties of NaAlH4, Advanced Energy Materials, 2 (2012) 560-568.
[148] Y. Liu, X. Zhang, K. Wang, Y. Yang, M. Gao, H. Pan, Achieving ambient temperature hydrogen storage in ultrafine nanocrystalline TiO 2@ C-doped NaAlH 4, Journal of Materials Chemistry A, 4 (2016) 1087-1095.
[149] X. Zhang, R. Wu, Z. Wang, M. Gao, H. Pan, Y. Liu, Preparation and catalytic activity of a novel nanocrystalline ZrO2@ C composite for hydrogen storage in NaAlH4, Chemistry–An Asian Journal, 11 (2016) 3541-3549.
[150] X. Zhang, Z. Ren, Y. Lu, J. Yao, M. Gao, Y. Liu, H. Pan, Facile Synthesis and Superior Catalytic Activity of Nano-TiN@ N–C for Hydrogen Storage in NaAlH4, ACS applied materials & interfaces, 10 (2018) 15767-15777.
[151] X. Zhang, Y. Liu, K. Wang, Y. Li, M. Gao, H. Pan, Ultrafine Nanocrystalline CeO2@ C ‐ Containing NaAlH4 with Fast Kinetics and Good Reversibility for Hydrogen Storage, ChemSusChem, 8 (2015) 4180-4188.
[152] X. Zhang, Y. Liu, K. Wang, M. Gao, H. Pan, Remarkably improved hydrogen storage properties of nanocrystalline TiO 2-modified NaAlH 4 and evolution of Ti-containing species during dehydrogenation/hydrogenation, Nano Research, 8 (2015) 533-545.

[153] d. Rafi ud, L. Zhang, L. Ping, Q. Xuanhui, Catalytic effects of nano-sized TiC additions on the hydrogen storage properties of LiAlH4, Journal of Alloys and Compounds, 508 (2010) 119-128.
[154] R.A. Varin, L. Zbroniec, T. Czujko, Z.S. Wronski, The effects of nanonickel additive on the decomposition of complex metal hydride LiAlH4 (lithium alanate), International Journal of Hydrogen Energy, 36 (2011) 1167-1176.
[155] V.P. Balema, J.W. Wiench, K.W. Dennis, M. Pruski, V.K. Pecharsky, Titanium catalyzed solid-state transformations in LiAlH4 during high-energy ball-milling, Journal of Alloys and Compounds, 329 (2001) 108-114.
[156] J. Chen, N. Kuriyama, Q. Xu, H.T. Takeshita, T. Sakai, Reversible hydrogen storage via titanium-catalyzed LiAlH4 and Li3AlH6, The Journal of Physical Chemistry B, 105 (2001) 11214-11220.
[157] Z. Cao, X. Ma, H. Wang, L. Ouyang, Catalytic effect of ScCl3 on the dehydrogenation properties of LiAlH4, Journal of Alloys and Compounds, 762 (2018) 73-79.
[158] Y. Kim, E.-K. Lee, J.-H. Shim, Y.W. Cho, K.B. Yoon, Mechanochemical synthesis and thermal decomposition of Mg(AlH4)2, Journal of Alloys and Compounds, 422 (2006) 283-287.
[159] A. Fossdal, H.W. Brinks, M. Fichtner, B.C. Hauback, Thermal decomposition of Mg(AlH4)2 studied by in situ synchrotron X-ray diffraction, Journal of Alloys and Compounds, 404-406 (2005) 752-756.
[160] V. Iosub, T. Matsunaga, K. Tange, M. Ishikiriyama, Direct synthesis of Mg(AlH4)2 and CaAlH5 crystalline compounds by ball milling and their potential as hydrogen storage materials, International Journal of Hydrogen Energy, 34 (2009) 906-912.
[161] A. Andreasen, T. Vegge, A.S. Pedersen, Dehydrogenation kinetics of as-received and ball-milled LiAlH4, Journal of Solid State Chemistry, 178 (2005) 3672-3678.
[162] X. Xiao, L. Chen, X. Fan, X. Wang, C. Chen, Y. Lei, Q. Wang, Direct synthesis of nanocrystalline NaAlH 4 complex hydride for hydrogen storage, Applied Physics Letters, 94 (2009) 041907.
[163] C.P. Baldé, B.P. Hereijgers, J.H. Bitter, K.P. de Jong, Facilitated hydrogen storage in NaAlH4 supported on carbon nanofibers, Angewandte Chemie International Edition, 45 (2006) 3501-3503.
[164] S. Zheng, F. Fang, G. Zhou, G. Chen, L. Ouyang, M. Zhu, D. Sun, Hydrogen storage properties of space-confined NaAlH4 nanoparticles in ordered mesoporous silica, Chemistry of Materials, 20 (2008) 3954-3958.
[165] V. Stavila, R.K. Bhakta, T.M. Alam, E.H. Majzoub, M.D. Allendorf, Reversible Hydrogen Storage by NaAlH4 Confined within a Titanium-Functionalized MOF-74(Mg) Nanoreactor, ACS Nano, 6 (2012) 9807-9817.
[166] R.D. Stephens, A.F. Gross, S.L. Van Atta, J.J. Vajo, F.E. Pinkerton, The kinetic enhancement of hydrogen cycling in NaAlH(4) by melt infusion into nanoporous carbon aerogel, Nanotechnology, 20 (2009) 204018.
[167] T.K. Nielsen, M. Polanski, D. Zasada, P. Javadian, F. Besenbacher, J. Bystrzycki, J. Skibsted, T.R. Jensen, Improved Hydrogen Storage Kinetics of Nanoconfined NaAlH4 Catalyzed with TiCl3 Nanoparticles, ACS Nano, 5 (2011) 4056-4064.
[168] Y. Li, G. Zhou, F. Fang, X. Yu, Q. Zhang, L. Ouyang, M. Zhu, D. Sun, De-/re-hydrogenation features of NaAlH4 confined exclusively in nanopores, Acta Materialia, 59 (2011) 1829-1838.
[169] L. Wang, A. Rawal, M.Z. Quadir, K.-F. Aguey-Zinsou, Nanoconfined lithium aluminium hydride (LiAlH4) and hydrogen reversibility, International Journal of Hydrogen Energy, 42 (2017) 14144-14153.
[170] Y. Pang, Y. Liu, M. Gao, L. Ouyang, J. Liu, H. Wang, M. Zhu, H. Pan, A mechanical-force-driven physical vapour deposition approach to fabricating complex hydride nanostructures, Nature Communications, 5 (2014) 3519.
[171] A.W. Vittetoe, M.U. Niemann, S.S. Srinivasan, K. McGrath, A. Kumar, D.Y. Goswami, E.K. Stefanakos, S. Thomas, Destabilization of LiAlH4 by nanocrystalline MgH2, International Journal of Hydrogen Energy, 34 (2009) 2333-2339.

[172] N.S. Mustafa, M. Ismail, Enhanced hydrogen storage properties of 4MgH2 + LiAlH4 composite system by doping with Fe2O3 nanopowder, International Journal of Hydrogen Energy, 39 (2014) 7834-7841.
[173] M. Ismail, Y. Zhao, X.B. Yu, J.F. Mao, S.X. Dou, The hydrogen storage properties and reaction mechanism of the MgH 2 –NaAlH 4 composite system, International Journal of Hydrogen Energy, 36 (2011) 9045-9050.
[174] M. Ismail, Y. Zhao, X.B. Yu, S.X. Dou, Improved hydrogen storage performance of MgH2–NaAlH4 composite by addition of TiF3, International Journal of Hydrogen Energy, 37 (2012) 8395-8401.
[175] H. Cheng, Y. Chen, W. Sun, H. Lou, Y. Liu, Q. Qi, J. Zhang, J. Liu, K. Yan, H. Jin, Y. Zhang, S. Yang, The enhanced de/re-hydrogenation performance of 4MgH 2 -NaAlH 4 composite by doping with TiH 2, Journal of Alloys and Compounds, 698 (2017) 1002-1008.
[176] Y. Wang, L. Li, F. Qiu, C. An, Y. Wang, L. Jiao, H. Yuan, Synergetic effects of NaAlH4-TiF3 co-additive on dehydriding reaction of Mg(AlH4)2, Journal of Energy Chemistry, 23 (2014) 726-731.
[177] M.L. Christian, K.-F. Aguey-Zinsou, Core–shell strategy leading to high reversible hydrogen storage capacity for NaBH4, ACS nano, 6 (2012) 7739-7751.
[178] A. Züttel, P. Wenger, S. Rentsch, P. Sudan, P. Mauron, C. Emmenegger, LiBH4 a new hydrogen storage material, Journal of Power Sources, 118 (2003) 1-7.
[179] H.-W. Li, K. Kikuchi, Y. Nakamori, N. Ohba, K. Miwa, S. Towata, S. Orimo, Dehydriding and rehydriding processes of well-crystallized Mg (BH4) 2 accompanying with formation of intermediate compounds, Acta Materialia, 56 (2008) 1342-1347.
[180] T. Matsunaga, F. Buchter, P. Mauron, M. Bielman, Y. Nakamori, S. Orimo, N. Ohba, K. Miwa, S. Towata, A. Züttel, Hydrogen storage properties of Mg [BH4] 2, Journal of Alloys and Compounds, 459 (2008) 583-588.
[181] M. Aoki, K. Miwa, T. Noritake, N. Ohba, M. Matsumoto, H.-W. Li, Y. Nakamori, S. Towata, S. Orimo, Structural and dehydriding properties of Ca (BH 4) 2, Applied Physics A, 92 (2008) 601-605.
[182] G. Severa, E. Ronnebro, C.M. Jensen, Direct hydrogenation of magnesium boride to magnesium borohydride: demonstration of >11 weight percent reversible hydrogen storage, Chemical communications, 46 (2010) 421-423.
[183] K. Miwa, N. Ohba, S.-i. Towata, Y. Nakamori, A. Züttel, S.-i. Orimo, First-principles study on thermodynamical stability of metal borohydrides: Aluminum borohydride Al(BH4)3, Journal of Alloys and Compounds, 446-447 (2007) 310-314.
[184] A. ALMENNINCEN, C. GUNDERSEN, A. Haaland, A1 (BH4) 3, Acta Chemica Scandinavica, 22 (1968) 328-334.
[185] A. Züttel, A. Borgschulte, S.-I. Orimo, Tetrahydroborates as new hydrogen storage materials, Scripta Materialia, 56 (2007) 823-828.
[186] S.-I. Orimo, Y. Nakamori, N. Ohba, K. Miwa, M. Aoki, S.-i. Towata, A. Züttel, Experimental studies on intermediate compound of Li BH 4, Applied physics letters, 89 (2006) 021920.
[187] P. Martelli, R. Caputo, A. Remhof, P. Mauron, A. Borgschulte, A. Zuttel, Stability and decomposition of NaBH4, The Journal of Physical Chemistry C, 114 (2010) 7173-7177.
[188] Y. Filinchuk, B. Richter, T.R. Jensen, V. Dmitriev, D. Chernyshov, H. Hagemann, Porous and dense magnesium borohydride frameworks: synthesis, stability, and reversible absorption of guest species, Angewandte Chemie, 50 (2011) 11162-11166.
[189] H.W. Li, S. Orimo, Y. Nakamori, K. Miwa, N. Ohba, S. Towata, A. Züttel, Materials designing of metal borohydrides: Viewpoints from thermodynamical stabilities, Journal of Alloys and Compounds, 446-447 (2007) 315-318.
[190] Y. Nakamori, K. Miwa, A. Ninomiya, H. Li, N. Ohba, S.-i. Towata, A. Züttel, S.-i. Orimo, Correlation between thermodynamical stabilities of metal borohydrides and cation electronegativites: First-principles

calculations and experiments, Physical Review B, 74 (2006) 045126.
[191] Y. Nakamori, H.W. Li, M. Matsuo, K. Miwa, S. Towata, S. Orimo, Development of metal borohydrides for hydrogen storage, Journal of Physics and Chemistry of Solids, 69 (2008) 2292-2296.
[192] K. Miwa, N. Ohba, S. Towata, Y. Nakamori, S. Orimo, First-principles study on copper-substituted lithium borohydride, (Li1−xCux)BH4, Journal of Alloys and Compounds, 404-406 (2005) 140-143.
[193] D.B. Ravnsbæk, Y. Filinchuk, R. Cˇerný, T.R. Jensen, Powder diffraction methods for studies of borohydride-based energy storage materials, Zeitschrift für Kristallographie Crystalline Materials, 225 (2010) 557-569.
[194] E.A. Nickels, M.O. Jones, W.I. David, S.R. Johnson, R.L. Lowton, M. Sommariva, P.P. Edwards, Tuning the decomposition temperature in complex hydrides: synthesis of a mixed alkali metal borohydride, Angewandte Chemie, 47 (2008) 2817-2819.
[195] K.C. Kim, D.S. Sholl, Crystal structures and thermodynamic investigations of LiK (BH4) 2, KBH4, and NaBH4 from first-principles calculations, The Journal of Physical Chemistry C, 114 (2009) 678-686.
[196] H. Hagemann, M. Longhini, J.W. Kaminski, T.A. Wesolowski, R. Cerny, N. Penin, M.H. Sørby, B.C. Hauback, G. Severa, C.M. Jensen, LiSc (BH4) 4: a novel salt of Li+ and discrete Sc (BH4) 4− complex anions, The Journal of Physical Chemistry A, 112 (2008) 7551-7555.
[197] D. Ravnsbaek, Y. Filinchuk, Y. Cerenius, H.J. Jakobsen, F. Besenbacher, J. Skibsted, T.R. Jensen, A series of mixed-metal borohydrides, Angewandte Chemie, 48 (2009) 6659-6663.
[198] D.B. Ravnsbæk, C. Frommen, D. Reed, Y. Filinchuk, M. Sørby, B. Hauback, H.J. Jakobsen, D. Book, F. Besenbacher, J. Skibsted, Structural studies of lithium zinc borohydride by neutron powder diffraction, Raman and NMR spectroscopy, Journal of Alloys and Compounds, 509 (2011) S698-S704.
[199] J.Y. Lee, D. Ravnsbæk, Y.-S. Lee, Y. Kim, Y. Cerenius, J.-H. Shim, T.R. Jensen, N.H. Hur, Y.W. Cho, Decomposition reactions and reversibility of the LiBH4− Ca (BH4) 2 composite, The Journal of Physical Chemistry C, 113 (2009) 15080-15086.
[200] Z.-Z. Fang, X.-D. Kang, P. Wang, H.-W. Li, S.-I. Orimo, Unexpected dehydrogenation behavior of LiBH4/Mg (BH4) 2 mixture associated with the in situ formation of dual-cation borohydride, Journal of Alloys and Compounds, 491 (2010) L1-L4.
[201] I. Lindemann, R. Domenech Ferrer, L. Dunsch, Y. Filinchuk, R. Cerny, H. Hagemann, V. D'Anna, L.M. Lawson Daku, L. Schultz, O. Gutfleisch, Al3Li4(BH4)13: a complex double-cation borohydride with a new structure, Chemistry, 16 (2010) 8707-8712.
[202] L. Yin, P. Wang, Z. Fang, H. Cheng, Thermodynamically tuning LiBH4 by fluorine anion doping for hydrogen storage: A density functional study, Chemical Physics Letters, 450 (2008) 318-321.
[203] Z.-Z. Fang, X.-D. Kang, Z.-X. Yang, G.S. Walker, P. Wang, Combined Effects of Functional Cation and Anion on the Reversible Dehydrogenation of LiBH4, The Journal of Physical Chemistry C, 115 (2011) 11839-11845.
[204] X.-D. Kang, P. Wang, L.-P. Ma, H.-M. Cheng, Reversible hydrogen storage in LiBH4 destabilized by milling with Al, Applied Physics A, 89 (2007) 963-966.
[205] G.L. Xia, Y.H. Guo, Z. Wu, X.B. Yu, Enhanced hydrogen storage performance of LiBH4–Ni composite, Journal of Alloys and Compounds, 479 (2009) 545-548.
[206] J.A. Puszkiel, F.C. Gennari, Reversible hydrogen storage in metal-doped Mg–LiBH4 composites, Scripta Materialia, 60 (2009) 667-670.
[207] W. Cai, H. Wang, J. Liu, L. Jiao, Y. Wang, L. Ouyang, T. Sun, D. Sun, H. Wang, X. Yao, M. Zhu, Towards easy reversible dehydrogenation of LiBH 4 by catalyzing hierarchic nanostructured CoB, Nano Energy, 10 (2014) 235-244.

[208] X. Yu, D. Grant, G. Walker, Dehydrogenation of LiBH4 destabilized with various oxides, The Journal of Physical Chemistry C, 113 (2009) 17945-17949.
[209] X.B. Yu, D.M. Grant, G.S. Walker, Low-Temperature Dehydrogenation of LiBH4 through Destabilization with TiO2, The Journal of Physical Chemistry C, 112 (2008) 11059-11062.
[210] M. Au, W. Spencer, A. Jurgensen, C. Zeigler, Hydrogen storage properties of modified lithium borohydrides, Journal of Alloys and Compounds, 462 (2008) 303-309.
[211] M. Au, A.R. Jurgensen, W.A. Spencer, D.L. Anton, F.E. Pinkerton, S.-J. Hwang, C. Kim, R.C. Bowman Jr, Stability and reversibility of lithium borohydrides doped by metal halides and hydrides, The Journal of Physical Chemistry C, 112 (2008) 18661-18671.
[212] Y.H. Guo, X.B. Yu, L. Gao, G.L. Xia, Z.P. Guo, H.K. Liu, Significantly improved dehydrogenation of LiBH4destabilized by TiF3, Energy Environ. Sci., 3 (2010) 465-470.
[213] Z.-Z. Fang, X.-D. Kang, P. Wang, Improved hydrogen storage properties of LiBH4 by mechanical milling with various carbon additives, International Journal of Hydrogen Energy, 35 (2010) 8247-8252.
[214] X. Yu, Z. Wu, Q. Chen, Z. Li, B. Weng, T. Huang, Improved hydrogen storage properties of Li BH 4 destabilized by carbon, Applied physics letters, 90 (2007) 034106.
[215] Z.-Z. Fang, X.-D. Kang, P. Wang, H.-M. Cheng, Improved reversible dehydrogenation of lithium borohydride by milling with as-prepared single-walled carbon nanotubes, The Journal of Physical Chemistry C, 112 (2008) 17023-17029.
[216] A.F. Gross, J.J. Vajo, S.L. Van Atta, G.L. Olson, Enhanced hydrogen storage kinetics of LiBH4 in nanoporous carbon scaffolds, The Journal of Physical Chemistry C, 112 (2008) 5651-5657.
[217] Z.Z. Fang, P. Wang, T.E. Rufford, X.D. Kang, G.Q. Lu, H.M. Cheng, Kinetic- and thermodynamic-based improvements of lithium borohydride incorporated into activated carbon, Acta Materialia, 56 (2008) 6257-6263.
[218] X. Liu, D. Peaslee, C.Z. Jost, T.F. Baumann, E.H. Majzoub, Systematic Pore-Size Effects of Nanoconfinement of LiBH4: Elimination of Diborane Release and Tunable Behavior for Hydrogen Storage Applications, Chemistry of Materials, 23 (2011) 1331-1336.
[219] T. Sun, J. Liu, Y. Jia, H. Wang, D. Sun, M. Zhu, X. Yao, Confined LiBH4: Enabling fast hydrogen release at ~100 °C, International Journal of Hydrogen Energy, 37 (2012) 18920-18926.
[220] Y. Li, Q. Zhang, F. Fang, Y. Song, D. Sun, L. Ouyang, M. Zhu, Facile self-assembly of light metal borohydrides with controllable nanostructures, RSC Adv., 4 (2014) 983-986.
[221] J. Huang, Y. Yan, L. Ouyang, H. Wang, J. Liu, M. Zhu, Increased air stability and decreased dehydrogenation temperature of LiBH4via modification within poly(methylmethacrylate), Dalton Trans., 43 (2014) 410-413.
[222] L. Zang, W. Sun, S. Liu, Y. Huang, H. Yuan, Z. Tao, Y. Wang, Enhanced Hydrogen Storage Properties and Reversibility of LiBH4 Confined in Two-Dimensional Ti3C2, ACS applied materials & interfaces, 10 (2018) 19598-19604.
[223] S. Cahen, J.B. Eymery, R. Janot, J.M. Tarascon, Improvement of the LiBH4 hydrogen desorption by inclusion into mesoporous carbons, Journal of Power Sources, 189 (2009) 902-908.
[224] N. Brun, R. Janot, C. Sanchez, H. Deleuze, C. Gervais, M. Morcrette, R. Backov, Preparation of LiBH4@carbon micro–macrocellular foams: tuning hydrogen release through varying microporosity, Energy & Environmental Science, 3 (2010) 824.
[225] X.Y. Chen, Y.H. Guo, L. Gao, X.B. Yu, Improved dehydrogenation of LiBH4 supported on nanoscale SiO2 via liquid phase method, Journal of Materials Research, 25 (2011) 2415-2421.
[226] W. Sun, S. Li, J. Mao, Z. Guo, H. Liu, S. Dou, X. Yu, Nanoconfinement of lithium borohydride in Cu-MOFs towards low temperature dehydrogenation, Dalton transactions, 40 (2011) 5673-5676.
[227] L. Guo, L. Jiao, L. Li, Q. Wang, G. Liu, H. Du, Q. Wu, J. Du, J. Yang, C. Yan, Y. Wang, H. Yuan, Enhanced

desorption properties of LiBH4 incorporated into mesoporous TiO2, International Journal of Hydrogen Energy, 38 (2013) 162-168.
[228] P. Ngene, M.R. van Zwienen, P.E. de Jongh, Reversibility of the hydrogen desorption from LiBH4: a synergetic effect of nanoconfinement and Ni addition, Chemical communications, 46 (2010) 8201-8203.
[229] J.J. Vajo, S.L. Skeith, F. Mertens, Reversible storage of hydrogen in destabilized LiBH4, The Journal of Physical Chemistry B, 109 (2005) 3719-3722.
[230] U. Bösenberg, S. Doppiu, L. Mosegaard, G. Barkhordarian, N. Eigen, A. Borgschulte, T.R. Jensen, Y. Cerenius, O. Gutfleisch, T. Klassen, M. Dornheim, R. Bormann, Hydrogen sorption properties of MgH2–LiBH4 composites, Acta Materialia, 55 (2007) 3951-3958.
[231] L. Zeng, H. Miyaoka, T. Ichikawa, Y. Kojima, Superior hydrogen exchange effect in the MgH2− LiBH4 system, The Journal of Physical Chemistry C, 114 (2010) 13132-13135.
[232] J. Weiqing, C. Shilong, Effect of Al on the dehydrogenation of LiBH 4 from first-principles calculations, International Journal of Hydrogen Energy, 42 (2017) 6181-6188.
[233] J. Yang, A. Sudik, C. Wolverton, Destabilizing LiBH4 with a metal (M= Mg, Al, Ti, V, Cr, or Sc) or metal hydride (MH2= MgH2, TiH2, or CaH2), The Journal of Physical Chemistry C, 111 (2007) 19134-19140.
[234] V. Ozolins, E. Majzoub, C. Wolverton, First-principles prediction of thermodynamically reversible hydrogen storage reactions in the Li-Mg-Ca-BH system, Journal of the American Chemical Society, 131 (2008) 230-237.
[235] J.-H. Shim, J.-H. Lim, S.-u. Rather, Y.-S. Lee, D. Reed, Y. Kim, D. Book, Y.W. Cho, Effect of hydrogen back pressure on dehydrogenation behavior of LiBH4-based reactive hydride composites, The Journal of Physical Chemistry Letters, 1 (2009) 59-63.
[236] S.-A. Jin, Y.-S. Lee, J.-H. Shim, Y.W. Cho, Reversible Hydrogen Storage in LiBH4−MH2 (M = Ce, Ca) Composites, The Journal of Physical Chemistry C, 112 (2008) 9520-9524.
[237] J. Purewal, S.-J. Hwang, J. Bowman, Robert C, E. Rönnebro, B. Fultz, C. Ahn, Hydrogen Sorption Behavior of the ScH2− LiBH4 System: Experimental Assesment of Chemical Destabilization Effects, The Journal of Physical Chemistry C, 112 (2008) 8481-8485.
[238] P. Mauron, M. Bielmann, A. Remhof, A. Züttel, J.-H. Shim, Y.W. Cho, Stability of the LiBH4/CeH2 composite system determined by dynamic PCT measurements, The Journal of Physical Chemistry C, 114 (2010) 16801-16805.
[239] H. Kou, G. Sang, Z. Huang, W. Luo, L. Chen, X. Xiao, C. Hu, Y. Zhou, Comprehensive hydrogen storage properties and catalytic mechanism studies of 2LiBH4–MgH2 system with NbF5 in various addition amounts, International Journal of Hydrogen Energy, 39 (2014) 7050-7059.
[240] Y. Pang, Y. Liu, X. Zhang, Q. Li, M. Gao, H. Pan, Composition‐Dependent Reaction Pathways and Hydrogen Storage Properties of LiBH4/Mg (AlH4) 2 Composites, Chemistry–An Asian Journal, 10 (2015) 2452-2459.
[241] Y. Zhou, Y. Liu, Y. Zhang, M. Gao, H. Pan, Functions of MgH 2 in hydrogen storage reactions of the 6LiBH 4–CaH 2 reactive hydride composite, Dalton Transactions, 41 (2012) 10980-10987.
[242] Y. Zhou, Y. Liu, W. Wu, Y. Zhang, M. Gao, H. Pan, Improved hydrogen storage properties of LiBH4 destabilized by in situ formation of MgH2 and LaH3, The Journal of Physical Chemistry C, 116 (2012) 1588-1595.
[243] T. Ichikawa, S. Isobe, N. Hanada, H. Fujii, Lithium nitride for reversible hydrogen storage, Journal of Alloys and Compounds, 365 (2004) 271-276.
[244] B. Zhang, Y. Wu, Recent advances in improving performances of the lightweight complex hydrides Li-Mg-N-H system, Progress in Natural Science: Materials International, 27 (2017) 21-33.
[245] Y. Song, Z. Guo, Electronic structure, stability and bonding of the Li-NH hydrogen storage system, Physical Review B, 74 (2006) 195120.

[246] Z. Xiong, G. Wu, J. Hu, P. Chen, Ternary imides for hydrogen storage, Advanced materials, 16 (2004) 1522-1525.
[247] J. Rijssenbeek, Y. Gao, J. Hanson, Q. Huang, C. Jones, B. Toby, Crystal structure determination and reaction pathway of amide–hydride mixtures, Journal of Alloys and Compounds, 454 (2008) 233-244.
[248] R.R. Shahi, T.P. Yadav, M.A. Shaz, O.N. Srivastava, Effects of mechanical milling on desorption kinetics and phase transformation of LiNH2/MgH2 mixture, International Journal of Hydrogen Energy, 33 (2008) 6188-6194.
[249] Y. Nakamori, A. Ninomiya, G. Kitahara, M. Aoki, T. Noritake, K. Miwa, Y. Kojima, S. Orimo, Dehydriding reactions of mixed complex hydrides, Journal of Power Sources, 155 (2006) 447-455.
[250] Z. Xiong, G. Wu, J. Hu, Y. Liu, P. Chen, W. Luo, J. Wang, Reversible hydrogen storage by a Li–Al–N–H complex, Advanced functional materials, 17 (2007) 1137-1142.
[251] H.Y. Leng, T. Ichikawa, S. Hino, N. Hanada, S. Isobe, H. Fujii, New Metal−N−H System Composed of Mg(NH2)2 and LiH for Hydrogen Storage, The Journal of Physical Chemistry B, 108 (2004) 8763-8765.
[252] Y. Nakamori, G. Kitahara, K. Miwa, S. Towata, S. Orimo, Reversible hydrogen-storage functions for mixtures of Li 3 N and Mg 3 N 2, Applied Physics A, 80 (2005) 1-3.
[253] H.Y. Leng, T. Ichikawa, S. Isobe, S. Hino, N. Hanada, H. Fujii, Desorption behaviours from metal–N–H systems synthesized by ball milling, Journal of Alloys and Compounds, 404-406 (2005) 443-447.
[254] Y. Kojima, Y. Kawai, N. Ohba, Hydrogen storage of metal nitrides by a mechanochemical reaction, Journal of Power Sources, 159 (2006) 81-87.
[255] C. Wu, Y. Bai, J.-h. Yang, F. Wu, F. Long, Characterizations of composite NaNH2–NaBH4 hydrogen storage materials synthesized via ball milling, International Journal of Hydrogen Energy, 37 (2012) 889-893.
[256] Z. Xiong, J. Hu, G. Wu, Y. Liu, P. Chen, Large amount of hydrogen desorption and stepwise phase transition in the chemical reaction of NaNH2 and LiAlH4, Catalysis today, 120 (2007) 287-291.
[257] G. Soloveichik, J.-H. Her, P.W. Stephens, Y. Gao, J. Rijssenbeek, M. Andrus, J.C. Zhao, Ammine Magnesium Borohydride Complex as a New Material for Hydrogen Storage: Structure and Properties of Mg(BH4)2·2NH3, Inorganic Chemistry, 47 (2008) 4290-4298.
[258] Y.H. Guo, W.W. Sun, Z.P. Guo, H.K. Liu, D.L. Sun, X.B. Yu, Dehydrogenation Promotion of LiBH4·NH3 Through Heating in Ammonia or Mixing with Metal Hydrides, The Journal of Physical Chemistry C, 114 (2010) 12823-12827.
[259] Y. Guo, G. Xia, Y. Zhu, L. Gao, X. Yu, Hydrogen release from amminelithium borohydride, LiBH4·NH3, Chemical communications, 46 (2010) 2599-2601.
[260] X. Zheng, G. Wu, W. Li, Z. Xiong, T. He, J. Guo, H. Chen, P. Chen, Releasing 17.8 wt% H2 from lithium borohydride ammoniate, Energy & Environmental Science, 4 (2011) 3593.
[261] Z. Tang, Y. Tan, H. Wu, Q. Gu, W. Zhou, C.M. Jensen, X. Yu, Metal cation-promoted hydrogen generation in activated aluminium borohydride ammoniates, Acta Materialia, 61 (2013) 4787-4796.
[262] X. Chen, X. Yu, Electronic Structure and Initial Dehydrogenation Mechanism of M(BH4)2·2NH3 (M = Mg, Ca, and Zn): A First-Principles Investigation, The Journal of Physical Chemistry C, 116 (2012) 11900-11906.
[263] Y. Yang, Y. Liu, Y. Li, M. Gao, H. Pan, Heating Rate-Dependent Dehydrogenation in the Thermal Decomposition Process of Mg(BH4)2·6NH3, The Journal of Physical Chemistry C, 117 (2013) 16326-16335.
[264] Y. Yang, Y. Liu, Y. Zhang, Y. Li, M. Gao, H. Pan, Hydrogen storage properties and mechanisms of Mg(BH4)2·2NH3–xMgH2 combination systems, Journal of Alloys and Compounds, 585 (2014) 674-680.
[265] X. Chen, F. Yuan, Y. Tan, Z. Tang, X. Yu, Improved Dehydrogenation Properties of Ca (BH4) 2· n NH3 (n= 1, 2, and 4) Combined with Mg (BH4) 2, The Journal of Physical Chemistry C, 116 (2012) 21162-21168.
[266] Y. Guo, X. Yu, W. Sun, D. Sun, W. Yang, The hydrogen-enriched Al-B-N system as an advanced solid

hydrogen-storage candidate, Angewandte Chemie, 50 (2011) 1087-1091.
[267] Y. Guo, Y. Jiang, G. Xia, X. Yu, Ammine aluminium borohydrides: an appealing system releasing over 12 wt% pure H2 under moderate temperature, Chemical communications, 48 (2012) 4408-4410.